Beam-beam Interactions in Run IIa

T. Sen, M. Xiao
FNAL
P.O. Box 500
Batavia, IL 60510

January 25, 2002

Contents

Abstract

The Tevatron in Run IIa is operating with three trains of twelve bunches each. The impact of the long-range interactions on beam stability are more significant compared to Run I. We study these beam-beam interactions (head-on and long-range) at design Run IIa parameters with particle tracking. The model includes machine nonlinearities such as the field errors of the Interaction Region quadrupoles and the chromaticity sextupoles. Tune footprints and dynamic apertures are calculated for different bunches in a train. These calculations show that the long-range completely determine the dynamic aperture. Transport mechanisms leading to amplitude growth are identified. Initial studies of the impact of a crossing angle (relevant to Run IIb) are also reported.

1 INTRODUCTION

The Tevatron is now operating again in collider mode from summer 2001. In the first phase, termed Run IIa, 36 $\bar{p}$ bunches in three trains of twelve bunches collide with 36 proton bunches. This is a six-fold increase in the number of bunches from the last collider operation Run Ib. Design proton intensities are higher so the head-on beam-beam tune shifts experienced by the anti-protons are higher than in Run Ib. The greater number of long-range beam-beam interactions increase the total beam-beam induced tune spread of the anti-protons. Furthermore these effects are different for each $\bar{p}$ bunch in a train since the sequence of long-range interactions is different for each of them. All of these effects taken together may reduce the dynamic aperture (DA) and/or lifetime of the anti-protons significantly. In this report we calculate the DA of a few bunches including the nonlinear fields in the IR quadrupoles and the chromaticity sextupoles amongst the nonlinearities. In the second stage of Run II, the plan is to increase the luminosity further with more intense bunches, larger number of bunches to decrease the number of interactions per bunch crossing, and also introduce crossing angles at B0 and D0 to avoid parasitic collisions with small separations [1]. The synchro-betatron resonances generated by these crossing angles may be an issue so it would be advisable to study the effects of these resonances during machine studies with 36×36 bunches. We study the impact on the dynamic aperture due to these crossing angles. Table 1 shows the main beam parameters in Run Ib and Run IIa. Parts of this study have appeared in earlier reports [2], [3], [4], [5].

Table 1: Main beam parameters in Run I and Run II

	Run Ib $p/\bar{p}$	Run IIa $p/\bar{p}$
Luminosity [cm^{-2}sec^{-1}]	1.6×10^{31}	8.6×10^{31}
Bunch Intensities $\times10^{11}$	(2.3/0.55)	(2.7/0.7)
Emittances 95% [mm-mrad]	23/13	20/15
Number of bunches	6	36
Bunch separation [m]	1049.3	118.8
Beam size at IP [μm]	37/28	33/29
Beam-beam parameter/IP $\times10^{-3}$	3.4/7.4	1.5/9.9

Section 2 contains a theoretical discussion of the importance of bunch length effects in the head-on beam-beam interaction. Section 3 discusses the model of the head-on interaction with these effects that will be used in all subsequent simulations. Section 4, the heart of the paper, contains footprints and dynamic aperture calculations for different scenarios involving the middle anti-proton bunch in a train of 12 and also calculations for the bunches at the ends of the train. This section brings out the importance of the long-range interactions, specially those four interactions closest to the experiments at B0 and D0. Section 5 identifies the mechanisms that lead to particle loss both over short and long time intervals. Sections 6, 7 and 8 contain discussions of the effects of crossing angles including dynamic aperture calculations. We conclude in Section 9 with a wrap up of the main insights gained from these studies.

For the harried reader with little time and less patience, we suggest reading the introductory part of Section 4 (to understand the model of the Tevatron used in the simulations), Section 4.6 which summarizes the main conclusions for Run IIa at design parameters and finally Section 9.

2 Bunch length effects

Typically beam-beam effects are analysed by assuming that bunches are infinitesimally short (see e.g. [6]). A first attempt to include the effect of finite bunch lengths on the strengths of beam-beam driven resonances was made by Krishnagopal and Siemann [7]. Several assumptions were made, the most important of which was that the amplitude function (β function) stays constant over the length of the interaction and therefore the phase advances linearly with distance. This rapid change in phase leads to resonance strengths decreasing exponentially with bunch length. These authors had also remarked that this exponential form factor overestimates the impact of the bunch length. In this letter I revisit the study with finite bunch lengths without many of the simplifying assumptions made in the earlier analysis. Contrary to the earlier results I find that beam-beam effects oscillate with bunch length. This suggests that it may be possible to maximize the integrated luminosity in a hadron collider by a proper choice of bunch length.

When the ratio of the bunch length σ_s to the beta function β^* at the interaction point (IP) ~ 1, the change in the transverse beam size along the bunch length is significant (the "hour-glass effect") and reduces the effective luminosity. At the Tevatron where $\sigma_s \simeq 36$cm, $\beta^* = 35$cm, the reduction is about 25%. We expect that in addition to this purely geometrical effect, dynamical effects of the bunch length are also significant at the Tevatron.

The luminosity reduction for round beams is given by [8]

$$\mathcal{R}(u) = \frac{\mathcal{L}}{\mathcal{L}_0} = \sqrt{\pi} u \exp[u^2] \mathrm{erfc}(u) \tag{2.1}$$

where $u = \beta^*/\sigma_s$.

The ratio of the bunch length σ_s to the beta function β^* at the interaction point (IP) characterizes the scale at which bunch length effects become important. When $\sigma_s/\beta^* \sim 1$, the change in the transverse beam size along the length of the bunch becomes significant (the "hour-glass effect") and effectively reduces the luminosity. At the Tevatron where $\sigma_s \simeq 36$cm, $\beta^* = 35$cm, the reduction is about 25%. This purely geometrical effect of the bunch length has a major impact on the luminosity and we expect that dynamical effects of the bunch length are also significant at the Tevatron. By contrast for the LHC where $\sigma_s = 7.7$cm, $\beta^* = 50$cm [9], the luminosity reduction is only about 1% and dynamical effects due to the bunch length may not be very important.

Bunch lengths comparable to β^* may occur as a consequence of unavoidable longitudinal emittance increase in the injector chain, for example during bunch coalescing. It may also come about in the later stages of a collider's life cycle when the spot size at the IP (hence β^*) is decreased in order to increase the luminosity.

We begin our analysis with the Hamiltonian of a charged particle(say an anti-proton in the Tevatron)

$$H = \frac{\nu_x}{R} J_x + \frac{\nu_y}{R} J_y + H_s + V(x, y, s) \ . \tag{2.2}$$

Here (ν_x, J_x), (ν_y, J_y) are the linear tunes and actions in the horizontal and vertical planes respectively, R is the radius of the ring, H_s is the Hamiltonian describing the purely longitudinal motion.

Assume that at time $t = 0$ the centers of the two bunches coincide at the origin of coordinates. At time t later, the strong bunch and the weak bunch have gone in opposite directions and are a distance $2ct$ apart. However the test particle by virtue of its synchrotron oscillation is at a distance $s = ct + c\tau$ from the origin or at a distance $s + ct$ from the center of the opposite bunch. The beam-beam potential can be written as

$$V(x, y, s) = \frac{N_b r_p}{\gamma_p} \rho_L(s + ct) U(x, y) \tag{2.3}$$

where where N_b is the bunch intensity, r_p the classical proton radius, γ_p the relativistic factor, ρ_L is the longitudinal density of the strong bunch. The transverse part U of the beam-beam potential due to a transverse Gaussian density distribution of rms beam sizes $\sigma_{x,op}, \sigma_{y,op}$ is given by

$$U(x, y) = \int_0^\infty \frac{dq}{[(2\sigma_{x,op}^2 + q)(2\sigma_{y,op}^2 + q)]^{1/2}} \left\{ 1 - \exp[-\frac{x^2}{2\sigma_{x,op}^2 + q} - \frac{y^2}{2\sigma_{y,op}^2 + q}] \right\} \tag{2.4}$$

The variables $x, y, c\tau$ describing the motion of the particle can be expressed as

$$\begin{aligned} x &= \sqrt{2\beta_x J_x} \cos[\psi_x + \alpha_x(s) + \psi_{x,0}] \equiv \sqrt{2\beta_x J_x} \cos\phi_x \\ y &= \sqrt{2\beta_y J_y} \cos[\psi_y + \alpha_y(s) + \psi_{y,0}] \equiv \sqrt{2\beta_y J_y} \cos\phi_y \\ c\tau &= a_s \sigma_s \cos[\psi_s + \psi_{s,0}] \end{aligned} \tag{2.5}$$

where J_x, J_y are the transverse linear actions. $\psi_x = \nu_x s/R, \psi_y = \nu_y s/R$ are the periodic parts of the transverse phases while

$$\alpha_x(s) = \int_0^s ds \frac{1}{\beta_x} - \nu_x \frac{s}{R}$$

and similarly for $\alpha_y(s)$. a_s is the dimensionless synchrotron oscillation amplitude measured in units of the bunch length σ_s and ψ_s is the longitudinal phase. $\psi_{x,0}, \psi_{y,0}, \psi_{s,0}$ are the initial phases in the respective degrees of freedom. $s = R\theta$ describes the longitudinal position of the test particle. In general the Fourier transform of U depends on s via the dependence of $\sigma_{x,op}$, $\sigma_{y,op}$ on s for beams of arbitrary aspect ratio.

The beam-beam interaction is usually characterized by a parameter ξ which for round beams is $\xi = N_b r_p/(4\pi\gamma_p\epsilon)$.

2.1 Transverse harmonics of the beam-beam potential

Let

$$w_x = \frac{\beta_x J_x}{2\sigma_{x,op}^2 + q}, \quad w_y = \frac{\beta_y J_y}{2\sigma_{y,op}^2 + q} \tag{2.6}$$

Using the generating function for the modified Bessel functions $I_j(z)$,

$$e^{z\cos\theta} = \sum_{j=-\infty}^{\infty} I_j(z) e^{ij\theta} \tag{2.7}$$

we can write the potential in the form

$$\begin{aligned} U(x,y) &= \int_0^\infty \frac{dq}{[(2\sigma_{x,op}^2+q)(2\sigma_{y,op}^2+q)]^{1/2}} \left\{ 1 - e^{-(w_x+w_y)} \sum_{l_x=-\infty}^{\infty} \sum_{l_y=-\infty}^{\infty} (-1)^{l_x+l_y} I_{l_x}(w_x) I_{l_y}(w_y) \right. \\ & \left. \exp[2i(l_x\phi_x + l_y\phi_y)] \right\} \end{aligned} \tag{2.8}$$

U can be expanded as a Fourier series in the periodic parts of the phase

$$U(x,y) = \sum_{m_x} \sum_{m_y} \exp[i(m_x\psi_x + m_y\psi_y)] \bar{U}_{m_x,m_y} \tag{2.9}$$

where the Fourier harmonics can be found from

$$\bar{U}_{m_x,m_y} = \int \frac{d\psi_x}{2\pi} \int \frac{d\psi_y}{2\pi} e^{-i(m_x\psi_x + m_y\psi_y)} U(x,y) \tag{2.10}$$

Substituting in the expression for U from Equation (2.8) into the above and doing the integrations over ψ_x, ψ_y shows that only the even harmonics of the beam-beam potential are non-zero. Defining the harmonics $U_{2l_x,2l_y}$ as

$$\bar{U}_{2l_x,2l_y} = \exp\{2i[l_x(\alpha_x + \psi_{x,0}) + l_y(\alpha_y + \psi_{y,0})]\} U_{2l_x,2l_y} \tag{2.11}$$

we obtain the expansion

$$U(x,y) = \sum_{l_x} \sum_{l_y} \exp[2i(l_x\phi_x + l_y\phi_y)] U_{2l_x,2l_y} \tag{2.12}$$

in terms of the *total* phases ϕ_x, ϕ_y. The Fourier harmonics for a beam with arbitrary aspect ratio are given by

$$\begin{aligned} U_{0,0}(J_x,J_y) &= \int_0^\infty \frac{dq}{(2\sigma_x^2+q)^{1/2}(2\sigma_y^2+q)^{1/2}} \left(1 - e^{-(w_x+w_y)}\right) I_0(w_x) I_0(w_y) \\ U_{0,2l_y}(J_x,J_y) &= 2\int_0^\infty \frac{dq}{(2\sigma_x^2+q)^{1/2}(2\sigma_y^2+q)^{1/2}} (-1)^{(l_y+1)} e^{-(w_x+w_y)} I_0(w_x) I_{l_y}(w_y) \\ U_{2l_x,0}(J_x,J_y) &= 2\int_0^\infty \frac{dq}{(2\sigma_x^2+q)^{1/2}(2\sigma_y^2+q)^{1/2}} (-1)^{(l_x+1)} e^{-(w_x+w_y)} I_{l_x}(w_x) I_0(w_y) \\ U_{2l_x,2l_y}(J_x,J_y) &= 4(-1)^{(l_x+l_y+1)} \int_0^\infty \frac{dq}{[(2\sigma_x^2+q)(2\sigma_y^2+q)]^{1/2}} e^{-(w_x+w_y)} I_{l_x}(w_x) I_{l_y}(w_y) \end{aligned} \tag{2.13}$$

In general $U_{2l_x,2l_y}$ depend on s via $\sigma_{x,op}(s), \sigma_{y,op}(s), \beta_x(s), \beta_y(s)$.

We now specialize to round beams, a condition which is (to approximately fulfilled at most hadron colliders. Over the length of the collisions we assume

$$\sigma^2_{x,op}(s) = \sigma^2_{y,op}(s) = \beta(s)\epsilon = \sigma^2_{op} \tag{2.14}$$

where ϵ is the un-normalized emittance of both beams. In this case,

$$w_x = \frac{J_x}{2\epsilon[1 + q/\sigma^2_{op}(s)]}, \quad w_y = \frac{J_y}{2\epsilon[1 + q/\sigma^2_{op}(s)]} \tag{2.15}$$

Defining the integration variable, $u = 1/[1 + q/(2\sigma^2_{op})]$, the Fourier harmonics can be written as

$$U_{0,0} = \int_0^1 \frac{du}{u}\left\{1 - \exp[-\frac{(J_x + J_y)u}{2\epsilon}]\right\} I_0[\frac{J_x u}{2\epsilon}] I_0[\frac{J_y u}{2\epsilon}] \tag{2.16}$$

$$U_{2l_x,2l_y} = 4(-1)^{(l_x+l_y+1)} \int_0^1 \frac{du}{u} \exp[-\frac{(J_x + J_y)u}{2\epsilon}] I_{l_x}[\frac{J_x u}{2\epsilon}] I_{l_y}[\frac{J_y u}{2\epsilon}] \tag{2.17}$$

The s dependence factors out. The remarkable fact is that for round beams, these Fourier harmonics are independent of s. Another feature is that these depend only on the emittance and not on the beam size or β^*. Hence the tune shift with amplitude also depends only the emittance.

The beam-beam potential is periodic in the phases $\vec{\psi}$ and θ, hence we can expand in a Fourier series

$$V = \sum_{\vec{m},n} V_{\vec{m},n} \exp[i(\vec{m}\cdot\vec{\psi} - n\theta)] \tag{2.18}$$

where the Fourier harmonics are

$$V_{\vec{m},n} = \frac{N_b r_p}{\gamma_p} \int\int \frac{d\theta}{2\pi}\frac{d\psi_s}{2\pi} \int\int \frac{d\psi_x}{2\pi}\frac{d\psi_y}{2\pi} V(x,y,s) \exp[-i(\vec{m}\cdot\vec{\psi} - n\theta)] \tag{2.19}$$

Doing the ψ_x, ψ_y integrations shows that $V_{\vec{m},n}$ are non-zero only if m_x, m_y are even. Letting $m_x \to 2m_x, m_y \to 2m_y$, and replacing $\alpha_x + \psi_{x,0}$ by $\phi_x - \psi_x$ etc. we obtain

$$V_{2m_x,2m_y,m_s,n} = \frac{N_b r_p}{\gamma_p} \int\int \frac{d\theta}{2\pi}\frac{d\psi_s}{2\pi} \rho_L(s + ct) \exp[-i(2m_x\psi_x + 2m_y\psi_y + m_s\psi_s - n\theta)] \tag{2.20}$$

$$\exp[i(2m_x\phi_x + 2m_y\phi_y)] U_{2m_x,2m_y} \tag{2.21}$$

Since $U_{2m_x,2m_y}$ is independent of s or $\theta = s/R$ for round beams, the Fourier harmonic factorizes into a product of transverse and longitudinal harmonics

$$V_{2m_x,2m_y,m_s,n} = \frac{N_b r_p}{\gamma_p}\frac{1}{R} U_{2m_x,2m_y} L_{2m_x,2m_y,m_s,n}(a_s, \sigma_s) \tag{2.22}$$

Consider the argument of the first phase factor in the expression for $L_{2m_x,2m_y,m_s,n}(a_s,\sigma_s)$: $2m_x\psi_x + 2m_y\psi_y + m_s\psi_s - n\theta = [2m_x\nu_x + 2m_y\nu_y + m_s(\nu_s + \Delta\nu_s(a_s)) - n]\theta$. If the tunes are close to the synchro-betatron resonance

$$2m_x\nu_x + 2m_y\nu_y + m_s\nu_s = n \tag{2.23}$$

then this phase factor will be slowly varying. Define Δ to be the distance in tune space to this resonance,

$$\Delta \equiv 2m_x\nu_x + 2m_y\nu_y + m_s\nu_s - n \ll 1 \tag{2.24}$$

With these definitions, the longitudinal harmonic can be expressed as,

$$L_{2m_x,2m_y,m_s,n} = \int\int \frac{ds d\psi_s}{(2\pi)^2} \rho_L(2s - a_s\sigma_s\cos(\psi_s + \psi_{s,0})) \exp[-i(\Delta + m_s\Delta\nu_s)\theta] \exp[i(2m_x\phi_x + 2m_y\phi_y)] \tag{2.25}$$

where we have replaced ct by $s - a_s\sigma_s\cos(\psi_s + \psi_{s,0})$ in the argument of the longitudinal density.

2.2 Longitudinal harmonics of the beam-beam potential

Over the length of the interaction between the beams, the β functions grow quadratically with distance from the IPs. We will assume round beams at the IP, hence $\beta_x^* = \beta_y^* = \beta^*$.

$$\phi_x(s) = \int_0^s \frac{ds'}{\beta_x(s')} = \int_0^s \frac{ds'}{[\beta^* + s'^2/\beta^*]} = \chi = \phi_y(s), \qquad \chi = \tan^{-1}\frac{s}{\beta^*} \tag{2.26}$$

The phase χ accumulated over the rms length of the bunch varies from about 6° when $\sigma_s = 0.1\beta^*$ to 53° when $\sigma_s = \beta^*$ to 90° when $\sigma_s = 2\beta^*$. This change in phase is large compared to say the change in betatron phase of an off-momentum particle due to a finite chromaticity. For example with $\Delta p/p = 1.\times 10^{-4}$, corrected chromaticity = 5, the phase change is about 0.2°. Synchrotron oscillations of the off-momentum particles cause the betatron phase change to modulate which lead to other dynamical effects such as periodic crossings of resonances.

If we regard each kick as a phasor then it is clear that the net effect of the beam-beam kicks will depend strongly on the phase relationships between the kicks delivered over the length of the bunch and also of course on the phase between kicks over successive turns.

Using the relations

$$\cos(\tan^{-1}x) = \frac{1}{\sqrt{1+x^2}}, \quad \sin(\tan^{-1}x) = \frac{x}{\sqrt{1+x^2}}$$

we obtain

$$\exp[i(2m_x\phi_x + 2m_y\phi_y)] = \left[\frac{1+is/\beta^*}{1-is/\beta^*}\right]^{m_x+m_y} \tag{2.27}$$

Hence

$$L_{2m_x,2m_y,m_s,n} = \int\int \frac{ds d\psi_s}{(2\pi)^2}\rho_L(2s - a_s\sigma_s\cos(\psi_s+\psi_{s,0}))\exp[-i(\Delta + m_s\Delta\nu_s)\theta]\left[\frac{1+is/\beta^*}{1-is/\beta^*}\right]^{m_x+m_y} \tag{2.28}$$

Due to the symmetry of the round beams, the phase advance is the same in both planes and consequently $L_{\vec{m}}$ depends on the transverse harmonic numbers only through the sum m_+.

Calculation of the longitudinal harmonics requires that we consider a specific longitudinal density. Here we choose a Gaussian distribution which is a close approximation to the bunch distribution in most hadron colliders. Let

$$\rho_L(s) = \frac{1}{\sqrt{2\pi}\sigma_{s,op}}\exp[-\frac{s^2}{2\sigma_{s,op}^2}] \tag{2.29}$$

Let $\vec{m} \equiv (2m_x, 2m_y, m_s, n)$, $m_+ = m_x + m_y$. Then

$$\begin{aligned} L_{\vec{m}} &= \frac{1}{\sqrt{2\pi}\sigma_{s,op}}\exp[-\frac{a_s^2}{4}\frac{\sigma_s^2}{\sigma_{s,op}^2}]\int\frac{ds}{(2\pi)}\exp[-\frac{2s^2}{\sigma_{s,op}^2}]\exp[-i(\Delta+m_s\Delta\nu_s)\frac{s}{R}]\left[\frac{1+is/\beta^*}{1-is/\beta^*}\right]^{m_+} \\ &\times\int\frac{d\psi_s}{2\pi}\exp[-\frac{a_s^2}{4}\frac{\sigma_s^2}{\sigma_{s,op}^2}\cos 2\psi]\exp[\frac{2sa_s\sigma_s}{\sigma_{s,op}^2}\cos\psi] \end{aligned} \tag{2.30}$$

where we have written $\psi = \psi_s + \psi_{s,0}$. Using the generating functions for the modified Bessel functions Eq.(2.7), we can write the integral over the longitudinal phase as

$$\int\frac{d\psi_s}{2\pi}.... = \sum_{j=-\infty}^{\infty}\sum_{l=-\infty}^{\infty}(-1)^j I_j(\frac{a_s^2}{4}\frac{\sigma_s^2}{\sigma_{s,op}^2})I_l(\frac{2a_s s\sigma_s}{\sigma_{s,op}^2})e^{i(2j+l)\psi_{s,0}}\int\frac{d\psi_s}{2\pi}e^{i(2j+l)\psi_s} \tag{2.31}$$

The delta function from the ψ_s integration reduces the double sum to a single sum. Using the fact that $I_{-n}(z) = I_n(z)$, we obtain

$$L_{\vec{m}} = \frac{1}{\sqrt{2\pi}\sigma_{s,op}}\exp[-\frac{a_s^2}{4}\frac{\sigma_s^2}{\sigma_{s,op}^2}]\sum_{j=-\infty}^{\infty}(-1)^j I_j(\frac{a_s^2}{4}\frac{\sigma_s^2}{\sigma_{s,op}^2})F_j(a_s,\sigma_s,\sigma_{s,op}/\beta^*;m_+,\zeta) \tag{2.32}$$

where

$$F_j(a_s, \sigma_s, \sigma_{s,op}; m_+, \zeta) = \int_0^C \frac{ds}{(2\pi)} \exp[-\frac{2s^2}{\sigma_{s,op}^2}] \exp[-i\zeta s] \left[\frac{1+is/\beta^*}{1-is/\beta^*}\right]^{m_+} I_{2j}(\frac{2a_s s\sigma_s}{\sigma_{s,op}^2}) \quad (2.33)$$

$$\zeta = (\Delta + m_s \Delta\nu_s)\frac{1}{R}$$

The fact that the Bessel functions are even with respect to order implies that $F_{-j} = F_j$.

2.2.1 Upper bound on F_j

The upper bound to the integral can be found by taking the absolute value of the integral and taking the upper limit of the integral to approach infinity

$$F_j(a_s, \sigma_s, \sigma_{s,op}; m_+, \zeta) \leq \int_0^\infty \frac{ds}{(2\pi)} | \exp[-\frac{2s^2}{\sigma_{s,op}^2}] \exp[-i\zeta s] \left[\frac{1+is/\beta^*}{1-is/\beta^*}\right]^{m_+} I_{2j}(\frac{2a_s s\sigma_s}{\sigma_{s,op}^2})| \equiv F_j^{max} \quad (2.34)$$

where

$$F_j^{max}(a_s, \sigma_s, \sigma_{s,op}; m_+, \zeta) = \int_0^\infty \frac{ds}{(2\pi)} \exp[-\frac{2s^2}{\sigma_{s,op}^2}] I_{2j}(\frac{2a_s s\sigma_s}{\sigma_{s,op}^2})$$

$$= \frac{\sigma_{s,op}}{2\pi\sqrt{2}} \int_0^\infty du \exp[-u^2] I_{2j}(\frac{\sqrt{2}a_s\sigma_s}{\sigma_{s,op}}u) \quad (2.35)$$

From the table of integrals in Gradshteyn and Ryzhik (6.618.4) [10], it follows

$$F_j^{max}(a_s, \sigma_s, \sigma_{s,op}; m_+, \zeta) = \frac{\sigma_{s,op}}{4\sqrt{2\pi}} \exp[\frac{a_s^2}{4}\frac{\sigma_s^2}{\sigma_{s,op}^2}] I_j(\frac{a_s^2}{4}\frac{\sigma_s^2}{\sigma_{s,op}^2}) \quad (2.36)$$

Note that the order of the Bessel function is halved after doing the integration. Putting this back into the harmonic factor $L_{\vec{m}}$, the exponential factors cancel and we obtain

$$L_{\vec{m}}^{(1)} = \frac{1}{\sqrt{2\pi}\sigma_{s,op}} \exp[-\frac{a_s^2}{4}\frac{\sigma_s^2}{\sigma_{s,op}^2}] \sum_{j=-\infty}^{\infty} (-1)^j I_j(\frac{a_s^2}{4}\frac{\sigma_s^2}{\sigma_{s,op}^2}) F_j^{max} \quad (2.37)$$

$$= \frac{1}{8\pi} \sum_{j=-\infty}^{\infty} (-1)^j I_j^2(\frac{a_s^2}{4}\frac{\sigma_s^2}{\sigma_{s,op}^2}) \quad (2.38)$$

Remarkably enough, the infinite sum can be evaluated exactly. Appendix 1 shows that

$$\sum_{j=-\infty}^{\infty} (-1)^j I_j^2(z) = 1 , \qquad \forall z \quad (2.39)$$

Hence

$$L_{\vec{m}}^{(1)} = \frac{1}{8\pi} \quad (2.40)$$

This upper bound on F_j is valid for all bunch lengths $\sigma_{s,op}$ and all synchrotron oscillation amplitudes a_s. This however is not the upper bound on $L_{\vec{m}}$ as it involves the sum over alternatingly positive and negative values.

$$L_{\vec{m}}^{(1)} = \frac{1}{\sqrt{2\pi}\sigma_{s,op}} \exp[-\frac{a_s^2}{4}\frac{\sigma_s^2}{\sigma_{s,op}^2}] [I_0 F_0^{max} - 2I_1 F_1^{max} + 2I_2 F_2^{max} - \ldots] \quad (2.41)$$

It is therefore possible for Ł$_{\vec{m}}$ to be larger with non-vanishing bunch length and synchrotron oscillation amplitude a_s. The fact that $L_{\vec{m}}$ is constant in the short bunch length limit is to be expected - the beam-beam driven resonances are determined entirely by the transverse part of the potential U. In the unphysical limit of infinitely long bunches $\sigma_s/\beta^* \to \infty$, we find that $L_{\vec{m}} = (-1)^{m_+}/(8\pi)$, also independent of the longitudinal variables.

One may ask at what parameter values does the longitudinal harmonic $L_{\vec{m}}$ attain the value $1/8\pi$? Replacing the upper limit of the integral in F_j by infinity and scaling $\sigma_{s,op}$ out of the integral, we can write

$$L_{\vec{m}} = \frac{1}{\sqrt{2\pi}} \exp[-\frac{a_s^2}{4}] \sum_{j=-\infty}^{\infty} (-1)^j I_j(\frac{a_s^2}{4}) \int_0^\infty \frac{du}{(2\pi)} \exp[-2u^2] \exp[-i\zeta\sigma_{s,op}u] \left[\frac{1+i\sigma_{s,op}u/\beta^*}{1-i\sigma_{s,op}u/\beta^*}\right]^{m_+} I_{2j}(2a_s u) \tag{2.42}$$

It is easy to show that both phase factors in the integral attain their maximum value of unity only when $\sigma_{s,op}/\beta^* \to 0$. Hence in the limit of infinitely short bunches, the longitudinal harmonics are constant.

2.2.2 Dependence of $L_{\vec{m}}$ on bunch length and synchrotron amplitude

The real part of the longitudinal harmonic may be written as

$$Re(L_{\vec{m}}) = \frac{1}{(2\pi)^{3/2}} \exp[-\frac{a_s^2}{4}] \sum_j (-1)^j I_j(\frac{a_s^2}{4}) F_j(\sigma_s, a_s; m_+) \tag{2.43}$$

$$F_j = \int_0^\infty du e^{-2u^2} \cos[2m_+\chi - \zeta\sigma_s u] I_{2j}(2a_s u)$$

where $\chi = \arctan[\sigma_s u/\beta^*]$. We remark on several features of this expression.

- The only dependence on the bunch length σ_s arises via the argument of the cosine term, $2m_+\chi - \zeta\sigma_s u$. Hence we can expect the beam-beam harmonics to oscillate as a function of σ_s. If we assume that $\zeta \ll 1$, then $L_{\vec{m}}$ depends on σ_s only via the ratio σ_s/β^*.
- The dependence of the longitudinal harmonic on the betatron resonance order m_x, m_y is also oscillatory via $m_+ = m_x + m_y$.
- In the limit that $a_s \to 0$, only the $j = 0$ term contributes. This gives the value $1/(8\pi)$ (if the phase factor is ignored).

From here on we'll consider $\zeta = (\Delta + m_s\Delta\nu_s)/R = 0$. This is a good approximation for several reasons - close to a resonance $\Delta \ll 1$, while both the synchrotron tune ν_s and the spread in synchrotron tune $\Delta\nu_s < 10^{-3}$ in the Tevatron and hadron colliders generally. Under these conditions the synchrotron sideband number m_s plays no further role in the beam-beam harmonics. Consider the integral representation of I_j,

$$I_j(z) = \frac{1}{\pi} \int_0^\pi e^{z\cos\theta} \cos(j\theta) d\theta \tag{2.44}$$

Substituting this expression and interchanging the order of integration,

$$F_j = \frac{1}{\pi} \int_0^\pi \cos 2j\theta \int_0^\infty du \exp[-2u^2 + 2a_s u\cos\theta] \cos(2m_+\chi) \tag{2.45}$$

The saddle point of the integrand is at $u = u_0 = (1/2)a_s\cos\theta$. Plots of the integrand occuring in the integral over u show that it is non-zero mostly in the region from 0 to a_s and is nearly zero outside. We apply the saddle-point approximation,

$$\int_0^\infty du \exp[-2u^2 + 2a_s u\cos\theta] \cos(2m_+\chi) = \sqrt{\frac{\pi}{2}} \exp[\frac{1}{2}a_s^2\cos^2\theta] \cos[2m_+\chi_0] \tag{2.46}$$

where now $\chi_0 = \arctan([a_s\sigma_s/(2\beta^*)]\cos\theta)$. Hence

$$F_j \simeq= \frac{1}{\sqrt{2\pi}} e^{a_s^2/4} \int_0^\pi d\theta \cos 2j\theta \exp[\frac{1}{4}a_s^2\cos 2\theta] cos[2m_+\chi_0] \tag{2.47}$$

It is useful to define the dimensionless parameter $\lambda = a_s\sigma_s/(2\beta^*)$.

1) Arbitrary m_+ We will use

$$\exp[i2m_+\arctan(\lambda\cos\theta)] = \left[\frac{1+i\lambda\cos\theta}{1-i\lambda\cos\theta}\right]^{m_+}$$

to consider the complex form

$$\mathcal{F} = \frac{1}{2\sqrt{2\pi}}e^{a_s^2/4}\int_0^{2\pi} d\theta \exp[i2j\theta + \frac{1}{4}a_s^2\cos 2\theta]\left[\frac{1+i\lambda\cos\theta}{1-i\lambda\cos\theta}\right]^{m_+} \tag{2.48}$$

It is easy to show that $F_j = Real(\mathcal{F})$. $\mathcal{F}$ may be evaluated by a contour integration over the unit circle in the complex plane. Let $z = e^{i\theta}$. Then

$$\mathcal{F} = \frac{-i}{2\sqrt{2\pi}}\oint dz z^{2j-1}\exp[\frac{a_s^2}{8}(z+\frac{1}{z})^2]\left[\frac{2z+i\lambda(z^2+1)}{2z-i\lambda(z^2+1)}\right]^{m_+} \tag{2.49}$$

The third factor in the integrand has poles of order m_+ at $z_\pm = \pm i(\sqrt{\lambda^2+1}\mp 1)/\lambda$. Of these, only z_+ lies within the unit circle when $m_+ > 0$. The singularities of the integrand within the contour are therefore essential singularities at the origin and poles of order m_+ at $z = z_+ = i(\sqrt{\lambda^2+1}-1)/\lambda$.

The residue at the origin can be found by expanding the integrand in a Laurent series about $z = 0$ valid in the region $|z| < |z_+|$. The other residue requires the evaluation of

$$\begin{aligned}\mathrm{Res}(z=z_-) \;=\; & (-1)^{m_+}\lim_{z\to z_-}\frac{1}{(m_+-1)!}\left\{z^{2j-1}e^{[a_s^2(z+1/z)^2/8]}D^{m_+-1}\left[\frac{(z+z_+)(z+z_-)}{z-z_+}\right]^{m_+} + \right.\\ & \left.\sum_{k=0}^{m_+-1}\sum_{l=0}^{m_+-k}\frac{m_+!}{k!l!(m_+-k-l)!}D^k\left[\frac{(z+z_+)(z+z_-)}{z-z_+}\right]^{m_+}D^l z^{2j-1}D^{m_+-k-l}e^{[a_s^2(z+1/z)^2/8]}\right\}\end{aligned} \tag{2.50}$$

Here $D \equiv d/dz$ and $z_+ = -i(\sqrt{\lambda^2+1}+1)/\lambda$. This can be evaluated for any specific m_+ but the general expression for arbitrary m_+ is cumbersome. The residue and the longitudinal harmonic are easily evaluated at $m_+ = 1$.

$$L_{\vec{m}} = \frac{1}{4\pi}\left\{\frac{2\exp[-\frac{a_s^2}{4}(1+\frac{2}{\lambda^2})]}{\sqrt{\lambda^2+1}}\sum_j(-1)^j z_+^{2j}I_j(\frac{a_s^2}{4}) - \left(1+\sum_{k=1}^{\infty}c_{2k}\sum_{j=-\infty}^{\infty}(-1)^j I_j(\frac{a_s^2}{4})I_{j+k}(\frac{a_s^2}{4})\right)\right\}, \quad m_+ = 1 \tag{2.51}$$

where

$$c_k = 2\frac{(z_-+z_+)(z_-^k - z_+^k)}{(z_- - z_+)}$$

Figure 1 shows this harmonic as a function of the synchrotron oscillation amplitude a_s for three low values of m.

2) Large m_+

In the limit that m_+ is large, true in the vicinity of sum resonances, we can use the stationary phase approximation to evaluate F_j. Consider the form

$$\mathcal{F} = \frac{-i}{\sqrt{2\pi}}e^{a_s^2/4}\lim_{m_+\to\infty}\int_0^{\pi} d\theta\exp[i2m_+\chi_0]\left(\exp[i2j\theta+\frac{1}{4}a_s^2\cos 2\theta]\right) \tag{2.52}$$

The only stationary points of the first phase factor are at the two endpoints, neither of which is a point of inflection. Summing the contributions from these stationary points, we obtain

$$\mathcal{F}_j^{asymp} = \frac{1}{2\sqrt{m_+\lambda}}e^{a_s^2/2}\cos[2m_+\arctan(\lambda)] + O(\frac{1}{m_+}) \tag{2.53}$$

Note that the integral is independent of the index j. Substituting back into the expression for $L_{\vec{m}}$ and using the Bessel function identity $\sum_{j=-\infty}^{\infty}(-1)^j I_j(z) = \exp(-z)$, we find that the exponential factors cancel leaving us with

$$\lim_{m_+\to\infty} \mathrm{Re}(L_{\vec{m}}) = \frac{1}{2(2\pi)^{3/2}}\frac{1}{\sqrt{m_+\lambda}}\cos[2m_+\mathrm{arctan}(\lambda)] + O(\frac{1}{m_+}) \tag{2.54}$$

This simple expression shows that to leading order when m_+ is large, the beam-beam harmonics have a damped ($\propto (m_+\lambda)^{-1/2}$) oscillatory behaviour in the dimensionless parameter λ. This implies, for example, that fixed σ_s, β^*, there is no blow-up in the tails (large a_s). For intermediate values of a_s, there could be amplitude growth.

Note that these harmonics all have the same value (= $1/(4\pi)$) at $a_s = 0$. In the range from 0 to $4\sigma_s$, L_1 has a zero crossing only at $a_s \approx 3.4$, L_2 has a zero crossing at the smaller value of $a_s \approx 1.3$ while L_3 has two zero crossings, one at $a_s \approx 0.8$, the other at $a_s \approx 2.5$. In the vicinity of the zero crossings the beam-beam force will almost vanish implying that particles with these synchrotron amplitudes will be more stable than others near these sum resonances.

2.3 Resonance Analysis of the Head-on Beam-beam interaction

We have assumed that the tunes are close to the resonance $2m_x\nu_x + 2m_y\nu_y + m_s\nu_s = n$. In this case the terms in the beam-beam potential with the slowly varying phase factors are the most dominant terms. Using (2.2), (2.18) and (2.22) and after transforming to the independent coordinate $\theta = s/R$, the slowly varying averaged Hamiltonian is

$$H_{slow} = \nu_x J_x + \nu_y J_y + A[U_{0,0}L_{\vec{0}} + 2U_{m_x,m_y}L_{\vec{m}}\cos(2m_x\psi_x + 2m_y\psi_y + m_s\psi_s - n\theta)] + RH_s \equiv \bar{H} + RH_s \tag{2.55}$$

where

$$A = \frac{N_b r_p}{2\pi\gamma_{\bar{p}}}$$

H_s depends only on the longitudinal dynamics and does not have an impact on the betatron motion. We may therefore consider only the dynamics determined by $\bar{H}$.

Transform to a new frame $(J_1, \phi_1, J_2, \phi_2)$ with the generating function

$$F_2(\phi_x, \phi_y, J_1, J_2) = (\phi_x + \frac{m_y}{m_x}\phi_y - \frac{pN_{IP}}{2m_x}\theta)J_1 + \phi_y J_2 \tag{2.56}$$

The new Hamiltonian is

$$K \equiv H + \frac{\partial F_2}{\partial\theta} = \delta J_1 + \nu_y J_2 + A[U_{0,0}L_{\vec{0}} + 2U_{m_x,m_y}L_{\vec{m}}\cos(2m_x\phi_1)] \tag{2.57}$$

where δ is the distance (in tune space) to the resonance,

$$\delta = \nu_x + \frac{m_y}{m_x}\nu_y + \frac{m_s}{2m_x}\nu_s - \frac{pN_{IP}}{2m_x} \tag{2.58}$$

From the equations of motion it follows that

$$J_2 = J_y - \frac{m_y}{m_x}J_x = \mathrm{const.} \quad \text{or} \quad m_x J_y - m_y J_x = \mathrm{const.} \tag{2.59}$$

The tune shifts with amplitudes can be found from

$$\nu_1 \equiv \frac{\partial}{\partial J_1}\langle K\rangle, \quad \nu_2 \equiv \frac{\partial}{\partial J_2}\langle K\rangle \tag{2.60}$$

where the $\langle\rangle$ denote an average over the betatron phases. These can be shown to lead to

$$\Delta\nu_x = AU_{0,0;J_x} = \beta^* A\int_0^\infty \frac{dq}{(2\sigma_x^2+q)^{3/2}(2\sigma_y^2+q)^{1/2}}\left[I_0(w_x) - I_1(w_x)\right]I_0(w_y)e^{-(w_x+w_y)} \tag{2.61}$$

$$\Delta\nu_y = AU_{0,0;J_y} = \beta^* A\int_0^\infty \frac{dq}{(2\sigma_x^2+q)^{1/2}(2\sigma_y^2+q)^{3/2}}\left[I_0(w_y) - I_1(w_y)\right]I_0(w_x)e^{-(w_x+w_y)} \tag{2.62}$$

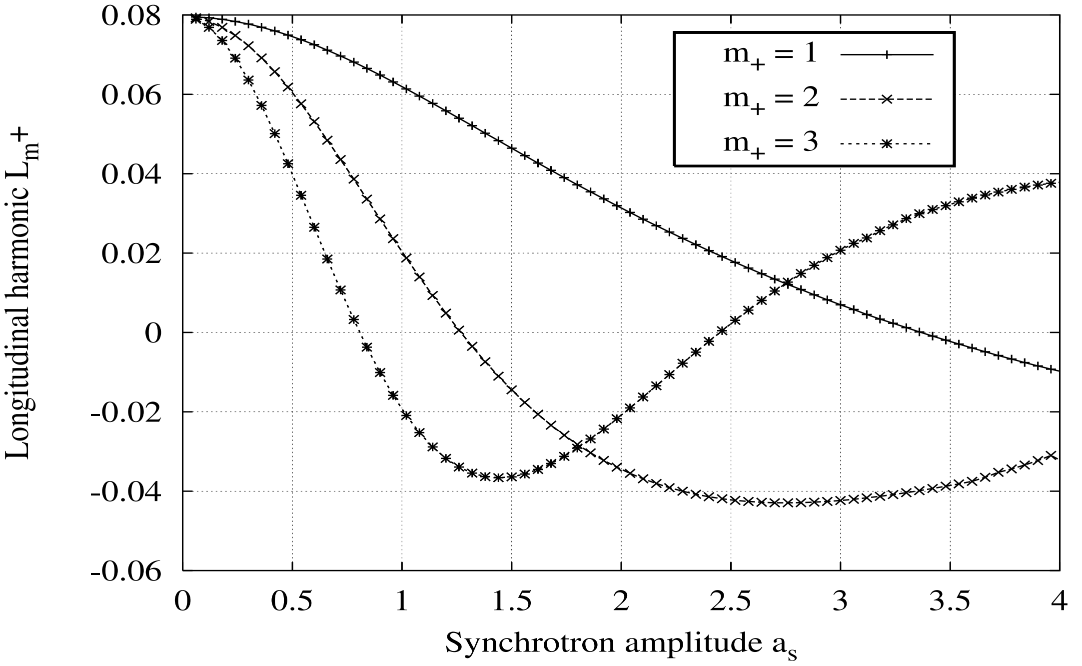

Figure 1: The longitudinal harmonic $L_{\vec{m}}$ as a function of the synchrotron amplitude a_s for three values of m_+. Assumed $\beta^* = \sigma_s, \zeta = 0$.

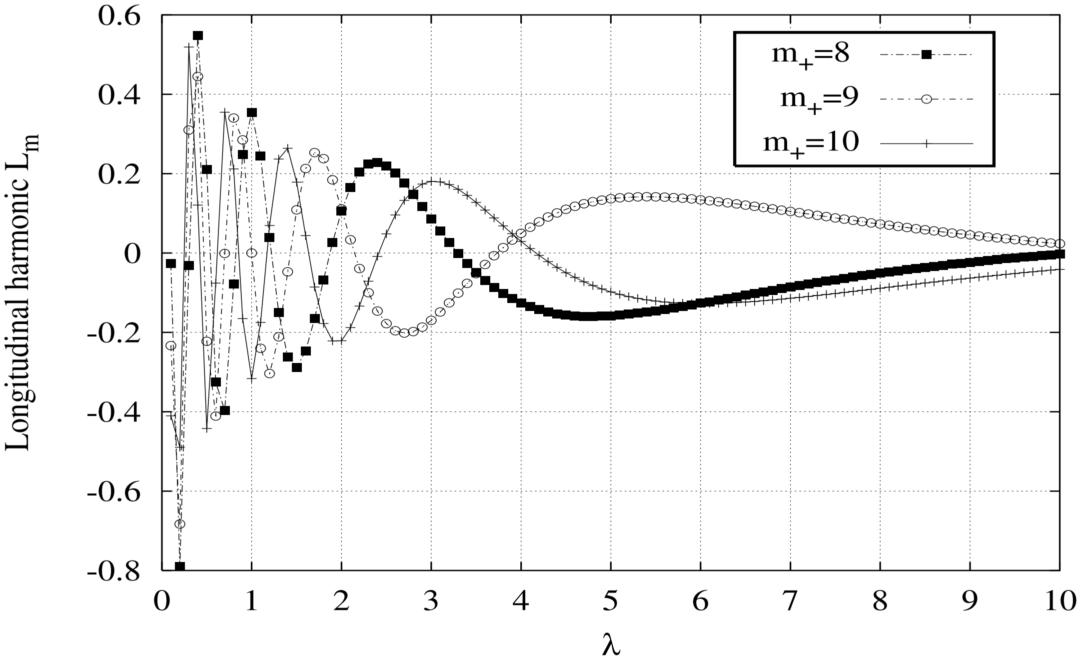

Figure 2: Asymptotic behaviour of $L_{\vec{m}}$ for large m_+ at $m_+ = 8, 9, 10$ as a function of $\lambda = a_s\sigma_s/(2\beta^*)$.

For round beams with $\sigma_x = \sigma_y = \sigma$, these expressions can be simplified to

$$\Delta\nu_x = N_{IP}\xi \int_0^1 dz \left[I_0(\frac{a_x^2 z}{4}) - I_1(\frac{a_x^2 z}{4})\right] I_0(\frac{a_y^2 z}{4}) \exp[-\frac{(a_x^2 + a_y^2)z}{4}] \tag{2.63}$$

$$\Delta\nu_y = N_{IP}\xi \int_0^1 dz\, I_0(\frac{a_x^2 z}{4}) \left[I_0(\frac{a_y^2 z}{4}) - I_1(\frac{a_y^2 z}{4})\right] \exp[-\frac{(a_x^2 + a_y^2)z}{4}] \tag{2.64}$$

Define (a_x, a_y) as

$$J_x = \frac{\sigma_x^2}{2\beta^*}a_x^2, \quad J_y = \frac{\sigma_y^2}{2\beta^*}a_y^2 \tag{2.65}$$

Consider the betatron resonances which are specified by the resonance condition

$$2m_x\nu_x(J_x, J_y) + 2m_y\nu_y(J_x, J_y) = n$$

These are satisfied only at certain amplitudes or actions in phase space. We call these the resonant actions. This resonance condition can be written in terms of the tune shifts from the origin,

$$\mathcal{R}(a_x, a_y) \equiv \delta + \Delta\nu_x + \frac{m_y}{m_x}\Delta\nu_y = 0 \tag{2.66}$$

For round beams with $a_y = ra_x$, the resonant condition is

$$\begin{aligned}\mathcal{R}(a_x, ra_x) = \; & \delta + \frac{A\beta^*}{2\sigma^2}\int_0^\infty \frac{dt}{(1+t)^2}\left\{[I_0(\frac{a_x^2}{4(1+t)}) - I_1(\frac{a_x^2}{4(1+t)})]I_0(r^2\frac{a_x^2}{4(1+t)})\right. \\ & \left. + \frac{m_y}{m_x}[I_0(r^2\frac{a_x^2}{4(1+t)}) - I_1(r^2\frac{a_x^2}{4(1+t)})]I_0(\frac{a_x^2}{4(1+t)})\right\}\exp[-\frac{(1+r^2)a_x^2}{4(1+t)}] = 0\end{aligned} \tag{2.67}$$

This equation defines a 1-parameter (r) family of surfaces which can be solved numerically to find the locations of the resonances.

Since J_2 is constant, we consider the dynamics defined by

$$K_1 = \delta J_1 + A[U_{0,0} + U_{m_x,m_y}\cos(2m_x\phi_1)] \tag{2.68}$$

Standard techniques can be used to calculate the resonance widths. The resonance half widths in action J_x, J_y are

$$\Delta J_{x,w} = m_x\left[2|\frac{U_{2m_x,2m_y}(J_{x,s}, J_{y,s})L_{\vec{m}}}{[m_x^2U_{0,0;J_xJ_x} + 2m_xm_yU_{0,0;J_xJ_y} + m_y^2U_{0,0;J_yJ_y}]L_{\vec{0}}}|\right]^{1/2} \tag{2.69}$$

$$\Delta J_{y,w} = m_y\left[2|\frac{U_{2m_x,2m_y}(J_{x,s}, J_{y,s})L_{\vec{m}}}{[m_x^2U_{0,0;J_xJ_x} + 2m_xm_yU_{0,0;J_xJ_y} + m_y^2U_{0,0;J_yJ_y}]L_{\vec{0}}}|\right]^{1/2} \tag{2.70}$$

Here the transverse harmonics U are evaluated at the locii of stable fixed points $(J_{x,s}, J_{y,s})$ corresponding to the resonance, $U_{0,0;J_xJ_x} \equiv \partial^2 U_{0,0}/\partial J_x^2$ etc.

For round beams $\sigma_x = \sigma_y = \sigma$,

$$U_{m_x,m_y} = 4(-1)^{m_x+m_y+1}\int_0^1 \frac{ds}{s}\exp[-\frac{a_x^2(1+r^2)}{4}s]I_{m_x}(\frac{a_x^2}{4}s)I_{m_y}(\frac{r^2a_x^2}{4}s) \tag{2.71}$$

The integral is defined over a finite range and the integrand is finite everywhere, even at the origin $s = 0$. The expression in the denominator of the resonance widths can be calculated as

$$\begin{aligned}m_x^2U_{0,0;J_xJ_x} + 2m_xm_yU_{0,0;J_xJ_y} + m_y^2U_{0,0;J_yJ_y} = \; & (\frac{\beta^2}{2\sigma^2})^2\int_0^1 ds\; s\exp[-\frac{a_x^2(1+r^2)}{4}s] \\ & \{m_x^2[2I_1(w_x) - I_1'(w_x) - I_0(w_x)]I_0(w_y) \\ & +2m_xm_y[I_0(w_x) - I_1(w_x)][I_1(w_y) - I_0(w_y)] \\ & +m_y^2[2I_1(w_y) - I_1'(w_y) - I_0(w_y)]I_0(w_x)\}\end{aligned} \tag{2.72}$$

$2m_x, 2m_y$	A_{res}(units of σ)	ΔA_{res}(units of σ)		
		$\sigma_s = 0$	$\sigma_s = 36$cm	
			$a_s = 0$	$a_s = 3.0$
2, 10	2.94	0.020	0.41×10^{-4}	0.24×10^{-3}
4, 8	3.25	0.056	0.12×10^{-3}	0.70×10^{-3}
6, 6	3.61	0.11	0.24×10^{-3}	0.14×10^{-2}
8, 4	4.08	0.15	0.31×10^{-3}	0.18×10^{-2}
10, 2	4.72	0.15	0.32×10^{-3}	0.19×10^{-2}
12, 0	5.70	0.14	0.31×10^{-3}	0.18×10^{-2}

Table 2: Twelfth order resonance locations A_{res} and resonance widths ΔA_{res} for a zero length bunch and for a 36cm long bunch at $a_s = 0, 3, r = 1$. At $a_s = 0$ and 3, the resonance widths are about three and two orders of magnitude smaller respectively compared to the widths for a zero length bunch.

where $w_x = a_x^2 s/4$, $w_y = r^2 w_x$.

At the operating tunes in the Tevatron $\nu_x = 0.581, \nu_y = 0.575$, the beam straddles the sum twelfth order resonances with fifth and seventh order resonances just outside the beam distribution. We have calculated the twelfth order resonance widths numerically using Equations (2.3.16), (2.3.17), (2.32) and (2.33) without any of the approximations made in the subsequent analysis. Both $U_{2m_x,2m_y}$ and $L_{\vec{m}}$ decrease with increasing resonance orders m_x, m_y for long bunches. For infinitesimally short bunches $L_{\vec{m}}/L_0$ is replaced by unity. We define the resonant actions as the actions where the resonance condition is exactly satisfied. The locations of these actions depend on the angular orientation in action or amplitude space. Figure 3 shows the resonant amplitudes and widths corresponding to the sum twelfth order resonances as functions of $r = a_y/(a_x+a_y)$. a_x, a_y are the dimensionless transverse amplitudes measured in units of the rms transverse size σ. Thus for example $r = 0.5$ corresponds to the 45° axis in (a_x, a_y) space. A necessary but not sufficient condition for resonances to overlap is that the dotted curves in Figure 3 corresponding to neighbouring resonance islands touch or intersect. Figure 3 shows that there is the possibility that the $10\nu_x + 2\nu_y$ and $8\nu_x + 4\nu_y$ resonances overlap in the region ($\sim 0.15 < r < 0.3$) for infinitesimally short bunches.

Since the resonance widths for finite bunch lengths depend on the synchrotron oscillation amplitude a_s, we will calculate the resonance widths of twelfth order for a few representative values of a_s. For example, when $\sigma_s = 36$cm, $a_s = 1.0$, $L_{\vec{m}}/L_{\vec{0}} = 1.7 \times 10^{-2}$. This ratio depends only on the sum $m_x + m_y$ and therefore is the same for all twelfth order sum resonances. The resonance widths for particles with $a_s = 1.0$ is therefore smaller than for zero length bunches by the ratio $\sqrt{1.7 \times 10^{-2}} = 0.13$. Figure 4 shows that the resonance islands are well isolated and there is no possibility of overlap between any of these resonances. This implies that chaotic motion is unlikely and particle orbits should be stable in this region of phase space when the bunch is long.

Table 2 shows the resonant actions A_{res} for the twelfth order resonances and the resonance widths for particles in a zero length bunch and also for particles at $a_s = 0, 3$ in a 36 cm long bunch. At these values of a_s, the resonance widths are smaller by three and two orders of magnitude respectively. From these calculations it is clear that the resonant widths for the vast majority of particles in a 36 cm long bunch are significantly smaller than in a zero length bunch. These analytical predictions can be checked with simulations.

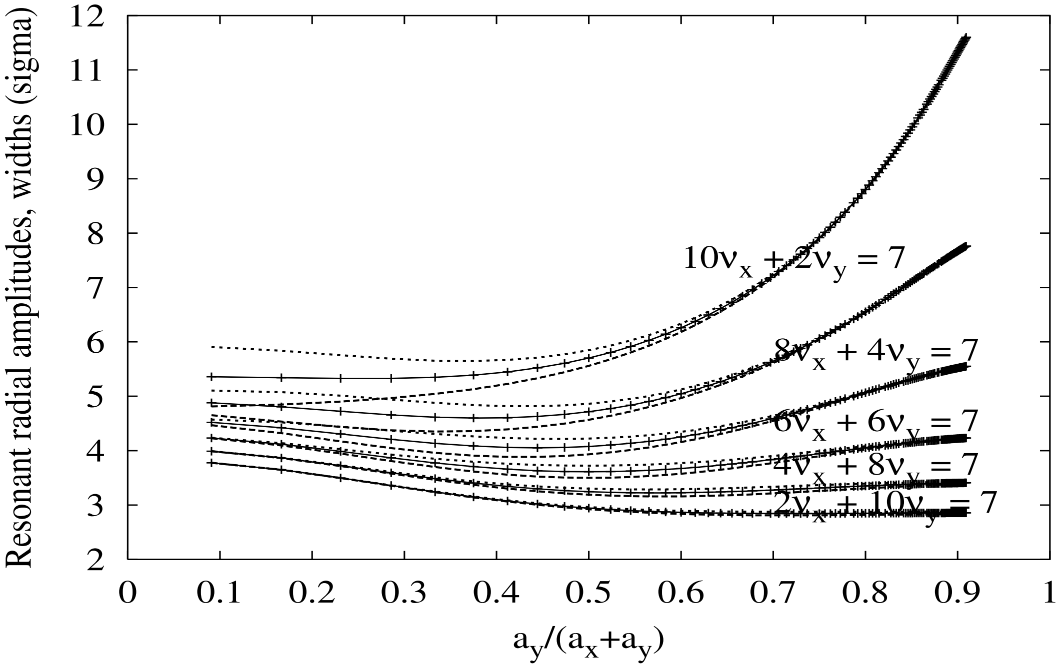

Figure 3: This figure shows the resonant actions and the widths of sum twelfth order resonances calculated for infinitesimally short bunches as a function of $a_y/(a_x+a_y)$. The linear tunes were set to $\nu_x = 0.581, \nu_y = 0.575$. The curves marked with + show the locations of the resonant action while the dotted curves on either side show the width of the resonance. There is a possibility of overlap between the $10\nu_x + 2\nu_y$ and $8\nu_x + 4\nu_y$ resonances.

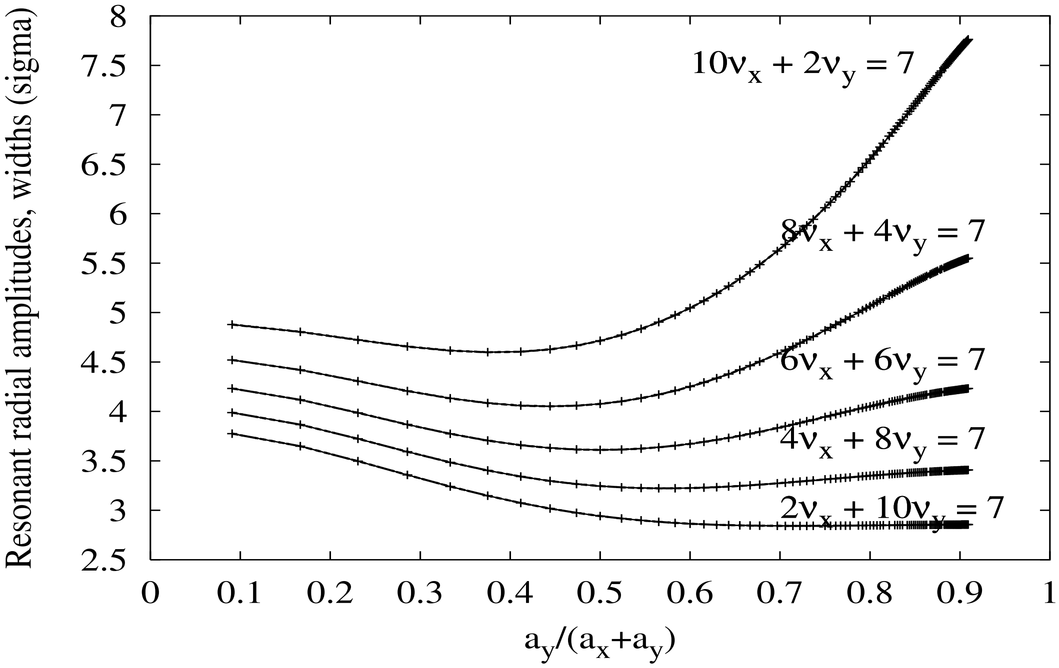

Figure 4: The same twelfth order resonances and widths calculated with a bunch length of 36cm and $a_s = 1.0$. The resonance widths are all reduced by 2 orders of magnitude. Now there is no possibility of overlap between any of these resonances.

3 Simulations with only head-on beam-beam interactions

The predictions of the analytical calculations can be tested with particle tracking using the equations of motion resulting from the Hamiltonian in Equation (2.2). We have calculated the amplitude growth of particles in the "weak" bunch (anti-protons at the Tevatron) due to interactions with the strong bunch (protons) with extensive multi-particle simulations. The strong bunch is sliced into several disks of charge (9 are found to suffice) of equal length. The longitudinal charge density of each disk falls off as a Gaussian from the center of the bunch. Particles in the weak bunch are subject to impulsive kicks from the center of each disk followed by a drift to the center of the next disk. We model the Tevatron by including two interaction points in the ring to simulate the collisions at CDF and D0. The arcs are represented by matrices so the beam-beam interactions are the only nonlinearities in the model. The phase advances in the arcs are adjusted so that the average tunes of a weak bunch calculated with the beam-beam interactions correspond to observed tunes.

Hourglass Effects

The transverse size of each disk is different because of the change in β function (hour-glass effect) and this is taken into account. For example the beta function and rms size in the horizontal plane is

$$\beta_x(i) = \beta_x^* + \frac{l_i^2}{\beta_x^*} = \beta_x^* + \frac{(s_i)^2}{\beta_x^*} \tag{3.1}$$

$$\sigma_x(i) = \sqrt{[1 + (\frac{(s_i)}{\beta_x^*})^2]}\sigma_x^* \; . \tag{3.2}$$

Longitudinal density variation

We assume that the bunch distribution varies as a Gaussian in the longitudinal plane. If $\rho(s_i)$ is the density of the i'th slice, the total charge in the bunch with N_s slices is

$$Q = \sum_i^{N_s} \Delta q_i = e \sum_i^{N_s} \rho(s_i) \Delta s_i \tag{3.3}$$

where Δs_i is the thickness of the i'th slice. If we assume that all slices are of uniform thickness $\Delta s_i = 2\sigma_s/N_s$, the fraction of the total charge in each slice is

$$\frac{\Delta q_i}{Q} = \frac{1}{\sum_{i=1}^{N_S} \exp[-i^2/(2N_S^2)]} \exp[-\frac{i^2}{2N_S^2}] \tag{3.4}$$

We assume that the effective length of the bunch is $2\sigma_s$.

We note that there are other ways of distributing the charge between the slices. As an example, another choice would be to consider all slices with the same charge but with thicknesses which increase from the center towards the ends.

Propagation between slices

We assume that the anti-proton receives a kick from the center of each slice. Between the slices the anti-proton is propagated by a drift map. Since the anti-protons and protons move with equal and opposite velocities, the anti-proton has to propagate by only half the thickness of a slice before it is at the center of the next slice. Hence the drift map from the $i-1$'th slice to the i'th slice, each of thickness Δs, is in the horizontal plane:

$$M_d(s_{i-1} \to s_i) = \begin{pmatrix} 1 & \frac{1}{2}\Delta s \\ 0 & 1 \end{pmatrix} \tag{3.5}$$

and similarly in the vertical plane.

Beam-beam kick

The kick on an anti-proton from the i'th slice of charge in the opposing proton bunch is

$$\Delta x' = 8\pi\xi_i \frac{x - x_i}{[(x-x_i)^2 + (y-y_i)^2]} \left\{ 1 - \exp[-\frac{[(x-x_i)^2]}{\sigma_x(i)^2} + \frac{[(y-y_i)^2]}{2\sigma_y(i)^2}] \right\} \tag{3.6}$$

$$\Delta y' = 8\pi\xi_i \frac{y - y_i}{[(x-x_i)^2 + (y-y_i)^2]} \left\{ 1 - \exp[-\frac{[(x-x_i)^2]}{\sigma_x(i)^2} + \frac{[(y-y_i)^2]}{2\sigma_y(i)^2}] \right\} \tag{3.7}$$

Beam Energy [TeV]	1.0
Bunch Intensity $N_{b,op}$	2.7×10^{11}
Normalized emittance of protons ϵ_N (95%) [mm-mrad]	20
Beta function at IP [m]	0.35
Bunch length σ_s [m]	0.36
σ_E/E	8.90×10^{-5}
Beam-beam parameter/IP ξ	9.9×10^{-3}
Revolution frequency [kHz]	47.713
Bunch spacing [m]	118.78
Beam-beam parameter	0.0099
Beam size @ IP [μm]	33.07
Beam divergence @ IP[μrad]	94.5
Tunes	(0.5811, 0.5751, 7.03×10^{-4})
No. of longitudinal slices	9

Table 3: Parameter values of the Tevatron used in the simulations.

where ξ_i, the beam-beam strength parameter for the slice, is

$$\xi_i = \xi \frac{\Delta q_i}{Q} \tag{3.8}$$

In the expression for the kicks, x is the horizontal distance from the longitudinal axis which goes through the center of the detector and x_i is the corresponding distance of the i'th slice.

Complete beam-beam map

The map across the strong bunch is of the form

$$\mathcal{M} = \mathcal{M}_{BB}(N_S)M_d(N_S-1 \rightarrow N_S)\mathcal{M}_{BB}(N_S-1)M_d(2 \rightarrow 3)\ldots\mathcal{M}_{BB}(2)M_d(1 \rightarrow 2)\mathcal{M}_{BB}(1) \tag{3.9}$$

where we start with a beam-beam kick from the 1st slice, followed by a drift through the slice of thickness $2\sigma_s/N_S$, followed by a kick etc. and ending with a beam-beam kick from the last slice N_S.

Simulation tune, lattice tune, observed tune

The phase advance due to the drift across the bunch of total length $2\sigma_s$ is $2\arctan[\sigma_s/(\beta^*)]$.

If the linear tune is ν_L, the phase advance in the lattice in a model with N_{IP} IPs is set to

$$\Delta\psi_{lattice} = 2\pi\nu_L - N_{IP} \times 2\tan^{-1}[\frac{\sigma_s}{\beta^*}] \tag{3.10}$$

The linear tune however does not correspond to the observed tune specially when the beams collide. The Schottky monitor picks up the coherent motion of the bunch centroid which has a frequency different from that of zero amplitude particles. It is known that if the beam-beam parameter is ξ, then the coherent tune of a Gaussian bunch is shifted by 0.5ξ, [11] i.e. the coherent tune is

$$\nu_{coh} = \nu_L + 0.5N_{IP}\xi + \ldots \tag{3.11}$$

where the ellipsis include contributions from other sources of coherent tune shifts. In the simulations to be reported here, the tune that will be specified is the linear tune ν_L.

In the simulations reported here, the time evolution of 1000 particles in the weak bunch was followed for 100,000 turns (more than 70 synchrotron periods) at each setting of the parameters. The maximum and minimum amplitude reached by each particle during the 100,000 turns is recorded and the ratio of these limits (the swing) is taken as a measure of the resonance strength experienced by the particle (see e.g. [12]). The maximum swing over the distribution of 1000 particles is chosen as a measure of the beam-beam resonance strength experienced by the bunch. In one set of simulations all particles are chosen to have $a_s = 1$ while in the second set we choose

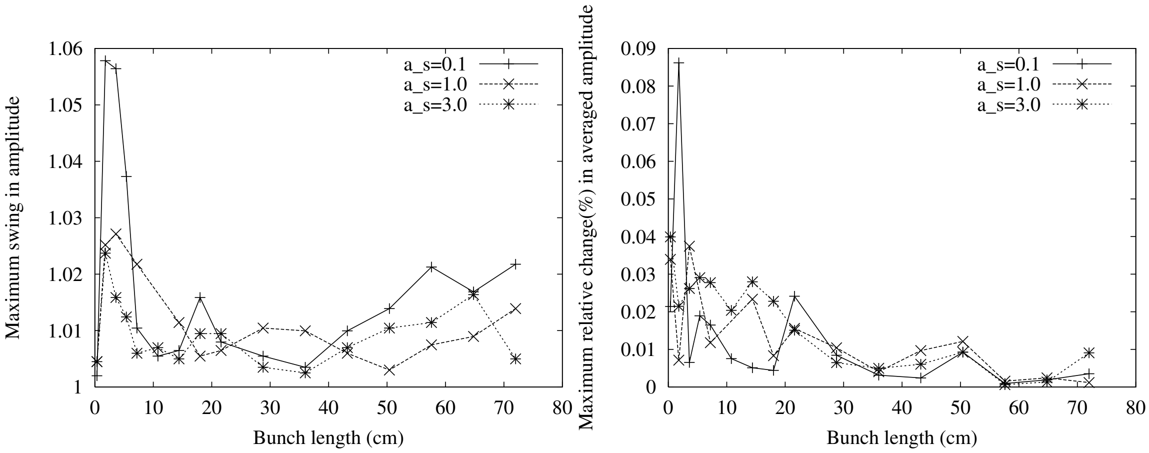

Figure 5: Left: Maximum relative amplitude swing, Right: Maximum % change in average amplitude of 1000 particles tracked for 100,000 turns as a function of bunch length. Tunes are the nominal Tevatron values $\nu_x = 0.581$, $\nu_y = 0.575$. No crossing angle.

a Gaussian distribution in a_s with a cutoff at $a_s = 3$. The calculations are repeated with different values of the bunch length with other parameters staying constant. Table 3 shows the values of the relevant parameters used in the simulations.

Figure 5 shows the maximum relative swing recorded amongst the 1000 particles when the tunes are set to the Tevatron values $\nu_x = 0.581, \nu_y = 0.575$. Several features are noteworthy. The amplitude swing is very low at these well chosen tunes - the swing would be unity in the absence of the beam-beam interactions. However the maximum swings do show clear evidence of oscillation with increasing bunch length. The height of these peaks decrease as the bunch length increases. Both these feature are in qualitative agreement with the results predicted by the asymptotic analysis seen in Figure 2. These simulations have been repeated at tune values closer to fourth and sixth order resonances. The maximum growth in averaged amplitude are larger, and again oscillate as the bunch length increases.

With the bunch length fixed at 36 cm, we have followed the evolution of the transverse amplitudes within the particle distribution. In these calculations the initial distribution was composed of two sets of particles: a uniform distribution of 1000 particles between 0 and 4 σ and another uniform distribution of 1000 particles between 4 and 10 σ. Particles within the core are well represented and this choice of distribution also enables us to determine amplitude growth in the tails with a significant number of particles which would not be the case with a Gaussian distribution. During the tracking the maximum and minimum amplitude reached by each particle is recorded and the ratio of these limits is taken as the maximum wing of the particle. Figure 6 shows the maximum swing for each particle in the distribution. The swings are in an absolute sense quite small but are *relatively* large between 5 and 6 σ - the region crossed by the $12\nu_x$ and $10\nu_x + 2\nu_y$ resonances. These resonances are also the twelfth order resonances with the largest widths. Tracking shows that the amplitude swings are large where the resonance widths are large, as they should be. Overall the amplitude swings of all particles in the distribution are small enough that there is no increase in the size of the distribution. All particles stay well within the physical aperture ($\sim 18\sigma$). Simulations with a 4D phase space distribution, i.e. assuming a zero length bunch, showed that the relative amplitude swings were larger. This agrees with the analytical predictions and the results from the simulations shown in Figure 5.

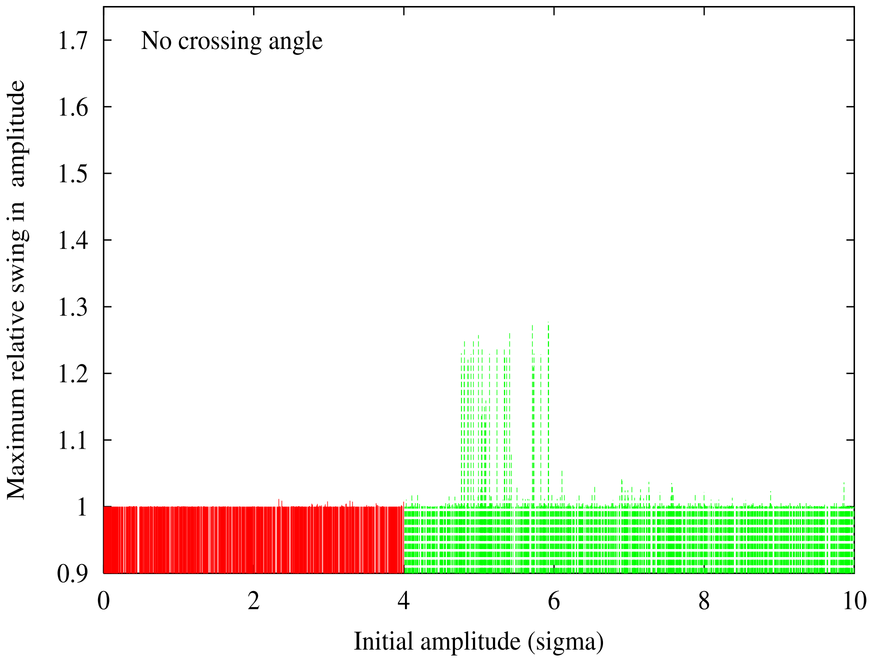

Figure 6: (color) Change in particle amplitudes with only the head-on beam-beam interactions. The bunch length was fixed to the nominal value of 36 cm. The ordinate represents the maximum amplitude relative to the initial amplitude reached by each particle over a million turns. The abscissa represents the initial tranverse amplitude of each particle. Each line represents a particle. The amplitude swings are relatively large between 4.5-6 σ. This is the region crossed by the twelfth order resonances and their synchrotron sidebands. Everywhere else there is almost no change in amplitude.

Conclusions from the study of the head-on beam-beam interactions alone

- The tune shifts with amplitude for round beams depend only on the emittance. This is a generalization of the statement that the beam-beam tune shift parameter (zero amplitude tune shift) depends only on the emittance.
- Close to resonances $2m_x\nu_x + 2m_y\nu_y + m_s\nu_s = n$ where $m_x + m_y$ is large, the theory predicts that the beam-beam resonance strengths have an oscillatory dependence on the bunch length. Simulations confirm that maximum amplitude swings oscillate as a function of bunch length.
- The finite bunch length significantly reduces the resonance widths calculated in the zero bunch length approximation, specially for high order resonances. There is no overlap of the 12th order sum resonances when the bunch length effects are included.
- Shortening the bunches is usually a difficult proposition as it requires either increasing the RF voltage or increasing the transverse focusing in the arcs. Lengthening the bunches is technically more feasible either by a deliberate injection mismatch or with RF noise.

4 Footprints and dynamic aperture calculations

In the earlier sections we studied the effects of the head-on beam-beam interactions with the lattice modelled by a transfer matrix. A realistic simulation requires inclusion of the lattice nonlinearities. Of the several tracking codes available, we chose MAD for the simulations reported here. In earlier simulations [4], [5] we had also used TEVLAT. In most cases where the lattice models were similar, results obtained by the two codes agreed to within 10-15%. In the future we may use other faster codes such as Sixtrack [13].

The calculations in Section 2 showed that bunch length effects which include hour glass effects, longitudinal Gaussian density distribution and phase averaging reduce resonance strengths in the Tevatron by two orders of magnitude compared to strengths calculated with zero length bunches. Within MAD, the beam-beam lens at each head-on interaction is split into 9 equally thick slices with the charge on each slice and the transverse size of each slice varying as described earlier. Drifts between the slices are added to include the change in betatron phase over the beam-beam lens. These effects are not as important for the long-range beam-beam interactions so they are modelled by delta function kicks. All bunches in the strong beam (protons) are assumed to have the same intensity and the same emittance.

The MAD lattice itself was obtained from the Tevatron department in 2001 and included all the recent magnet reshuffles in the B0 and D0 IRs. The magnetic nonlinearities included are the chromaticity sextupoles and the nonlinear multipoles up to the twentieth pole in the IR quadrupoles. The table of multipole errors in these quadrupoles may be found in Appendix B. Aperture restrictions are placed at ± 35 mm within these quadrupoles at locations corresponding to a physical aperture of about 18σ. All the studies reported here are done at a top energy of 980 GeV so the separation helix at this energy is used.

The most important lattice effects not included in this study are the nonlinearities in the arc magnets and magnet misalignments. Bunch to bunch variations in intensity and emittance are not considered nor are external influences such as power supply ripple or ground vibrations. At a later stage when a reliable faster tracking code is available, these effects can be studied.

The dynamic aperture is calculated by launching particles at several angles in $x - y$ space, usually thirteen spaced apart by 7.5°, from 0° to 90°. The radial dynamic aperture at each angle is calculated from the largest stable amplitude below which all amplitudes are stable. From these values at different angles we extract an angle averaged dynamic aperture and a minimum value.

4.1 Single beam

It is important first to consider the impact of the machine nonlinearities on the beam. This serves at least two purposes. Dynamic aperture measurements are always difficult but relatively easier with only a single beam in the machine. These measurements have been performed at various accelerators [14, 15]. A comparison of the measured dynamic aperture with the calculated value is a good test of the model of the lattice. A comparison of the single beam dynamic aperture with the dynamic aperture obtained with the beam-beam forces shows the relative importance of the beam-beam effects.

The tune footprint is sometimes a good measure of the strength of the nonlinearities. Figure 7 shows the tune footprint extending to amplitudes of 6σ in each plane of a single beam with the machine nonlinearities mentioned above. The small amplitude tunes are at the lower right while the tunes at (6σ, 6σ) are at the upper left corner. The tune spread between these extreme amplitudes is about 0.0006. At the nominal working point (0.585, 0.575), the fooptrint straddles only some of the twelfth order sum resonances and does not reach the neighbouring 5th and 7th order resonances (not shown in the figure).

The machine chromaticity, linear and nonlinear, introduces an additional tune spread for off-momentum particles. For these particles, the linear lattice Twiss functions are also different. These effects have an influence on the strengths of the nonlinearities experienced by these particles. Figure 8 shows the change in tune and the maximum β function as a function of the momentum deviation $\Delta p/p$. The linear chromaticity is set to +5 units in the MAD model and the change in tune is primarily due to the linear chromaticity but there is a clear indication of contributions from the nonlinear chromaticity, presumably from the IR quadrupoles. Over the momentum range in the figure, the spread in the tune ~ 0.004 is much larger than the tune spread from the multipoles up to transverse amplitudes of 6σ. The change in the maximum β value is about ± 100 m or about 8% over the momentum range.

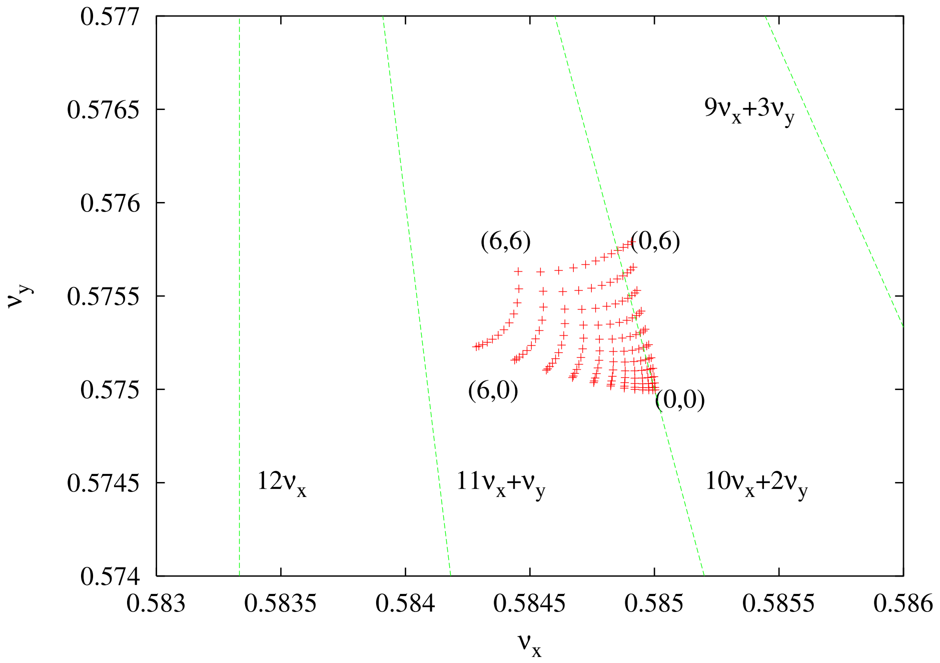

Figure 7: (color) Tune fooprint of a single beam with IR errors and chromaticity sextupoles. The zero amplitude tune is 0.585, 0.575. The footprint extends to 6σ in each plane. Over this amplitude range, the tune spread in each plane is about 6×10^{-4}. Also shown are four of the twelfth order sum resonances which are nearest to the footprint.

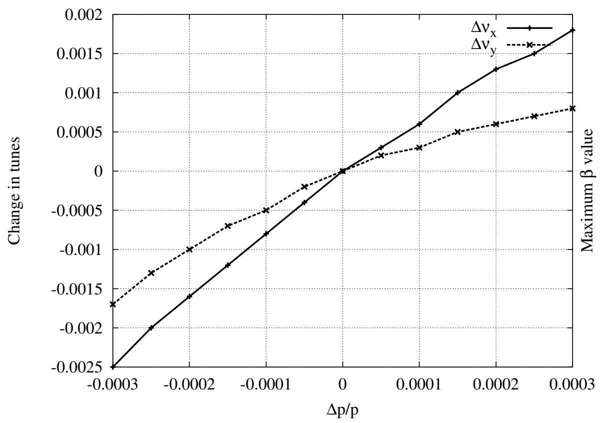

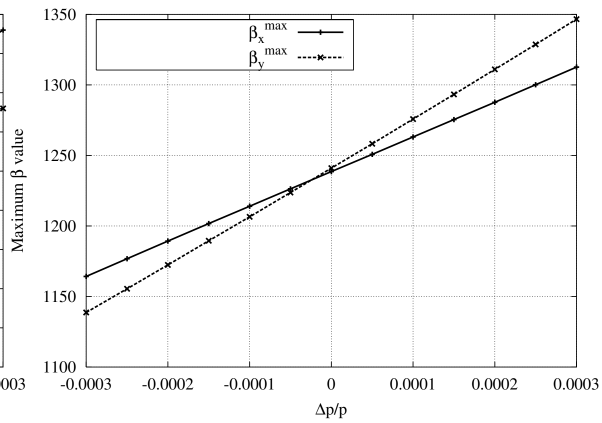

Figure 8: Left: Change in zero amplitude tunes with momentum deviation. Right: Maximum beta values vs the momentum deviation.

	Average DA $\langle DA \rangle$	Minimum DA DA_{min}
dp/p = 0	15.2	13.0
dp/p=1×10^{-4}	14.3	12.0
dp/p=3×10^{-4}	12.9	11.0

Table 4: The average and minimum 6D dynamic aperture of a single beam at three values of the momentum deviation after 10^5 turns.

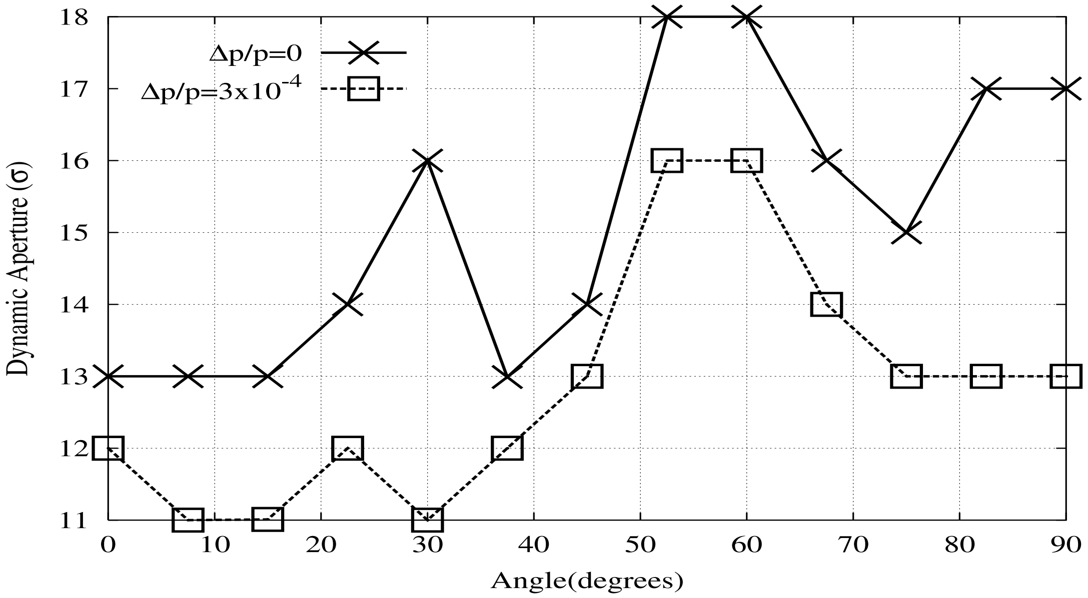

Figure 9: Dynamic aperture of a single beam after 10^5 turns as a function of initial angle in $x - y$ space. $0°$ corresponds to the x axis. Two cases are compared: one without momentum offset, the other with momentum offset and synchrotron oscillations.

Figure 9 shows the dynamic aperture calculated over 10^5 turns as a function of the initial angle in $x - y$ space. On momentum particles and particles with $\Delta p/p = 3 \times 10^{-4} \approx 3\sigma_p/p$ are tracked. The average and minimum dynamic aperture for the two cases are shown in Table 4.

It is typically the case with magnetic nonlinearities, specially in the absence of external time dependent effects such as power supply ripple, that the calculated dynamic aperture stabilizes after a few thousand turns and extending the tracking further does not change the calculated value by much. Indeed we find that after 10^6 turns, the average dynamic aperture with $\Delta p/p = 3 \times 10^{-4}$ is 12.3 σ which is only slightly smaller than the value of 12.9 σ obtained after 10^5 turns. The minimum dynamic aperture is the same at 11 σ in both cases. This model of the single beam tracking shows that the calculated dynamic aperture, at least as large as 11σ, should exceed the physical aperture set by the primary collimators which are typically placed at around 8σ.

4.2 All beam-beam interactions for bunch 6

Design values of the proton bunch intensities are about four times larger than design antiproton intensities. Consequently we will focus only on the beam-beam interactions experienced by the $\bar{p}$ bunches.

At B0 and D0, the beams are round and the kicks experienced by individual antiprotons are given by equations (3.6) and (3.7). while at all the parasitic collisions, the kicks are given by the Bassetti-Erskine expressions for Gaussian beams (assuming $\sigma_x > \sigma_y$),

$$\Delta x' = \frac{N_b r_p}{\gamma_p}\sqrt{\frac{2\pi}{\sigma_x^2 - \sigma_y^2}}\mathrm{Im}\; F(x,y) \tag{4.1}$$

$$\Delta y' = \frac{N_b r_p}{\gamma_p}\sqrt{\frac{2\pi}{\sigma_x^2 - \sigma_y^2}}\mathrm{Re}\; F(x,y) \tag{4.2}$$

and

$$F(x,y) = W\left[\frac{x+iy}{\sqrt{2(\sigma_x^2-\sigma_y^2)}}\right] - \exp[-\frac{x^2}{2\sigma_x^2} - \frac{y^2}{2\sigma_y^2}]W\left[\frac{x\frac{\sigma_y}{\sigma_x} + iy\frac{\sigma_x}{\sigma_y}}{\sqrt{2(\sigma_x^2-\sigma_y^2)}}\right] \tag{4.3}$$

where W is the complex error function. Similar expressions with $x \leftrightarrow y$ result if $\sigma_y > \sigma_x$. In the limit of round beams these reduce to the expressions in Equations (3.6) and (3.7). Here $x = x_\beta + D_x$, $y = y_\beta + D_y$ where x_β, y_β are the betatron amplitudes and D_x, D_y are the beam separations. The effective strengths of all the long-range kicks is determined by the beam separations, the size and intensity of the proton bunches and the phase advance between the kicks. At collision, the electrostatic separators are used to maximize the separations while colliding the beams at B0 and D0. Closed orbit fluctuations or drifts could make the separations change in time. The effective transverse size of the beams are determined by the emittance, the beta functions, the dispersion and the rms momentum spread via $\sigma_{x,eff} = \sqrt{\beta_x\epsilon_x + (D_x\delta_p)^2}$. There are many uncertainties in the beam size due to transverse and longitudinal emittance blow up in the injector chain and optics errors in the Tevatron itself. Finally the phase advance between the kicks can also change due to static and time dependent gradient errors. Here we will assume perfect conditions so all beam and Twiss parameters are assumed to be at their design values. Separator strengths in the MAD lattice we used were set without beam-beam collisions, so when we include the long-range collisions we also reset the separator strengths to center the beams at B0 and D0.

With 36×36 bunches, there are three trains of twelve bunches which fill the ring symmetrically. While the three trains are equivalent, the sequence of parasitic collisions depends on the location of the bunch within the train. For example the leading bunch 1 will experience all long-range interactions downstream of the IP, bunch 6 will experience five interactions upstream and six interactions downstream of the IP while the trailing bunch 12 will experience all long-range interactions upstream of the IP.

Figure 10 shows the beam separation (in units of the rms bunch size) at all the seventy two locations of beam-beam interactions for bunch 6. At most locations the beam separation is of the order of 10σ. The notable exceptions are the parasitic collisions nearest to the IPs where the separation is only about 6σ. As we will see, these four parasitic collisions have the strongest impact on the dynamic aperture of the antiproton beam.

The strength of each beam-beam kick and the phase advance between kicks are important parameters as mentioned earlier. One way to parametrize the strength of a kick with separated beams is by the tune shift experienced by zero amplitude particles. This is similar to the convention of using the beam-beam parameter ξ to parametrize the strength of head-on beam-beam collisions. For beams with arbitrary aspect ratios, the tune shifts of a particle at zero amplitude are given by [16].

$$\begin{aligned}
\Delta\nu_x(0,0) &= \frac{N_b r_p}{4\pi\gamma_p\epsilon_x}\int_0^1 \frac{dv}{\sqrt{(r^2-1)v+1}}(1-d_x^2 v)\exp\{-\frac{v}{2}[d_x^2 + \frac{d_y^2 r^2}{(r^2-1)v+1}]\} \\
\Delta\nu_y(0,0) &= \frac{N_b r_p r}{4\pi\gamma_p\epsilon_y}\int_0^1 \frac{dv}{\sqrt{(1-r^2)v+r^2}}(1-d_y^2 v)\exp\{-\frac{v}{2}[d_y^2 + \frac{d_x^2}{(1-r^2)v+r^2}]\}
\end{aligned} \tag{4.4}$$

Here $d_x = D_x/\sigma_x, d_y = D_y/\sigma_y, r = \sigma_y/\sigma_x$ where D_x, D_y are the separations between the beams in physical units, σ_x, σ_y are the rms beam sizes of the opposing beam. In the limit of round beams ($r = 1$), these simplify

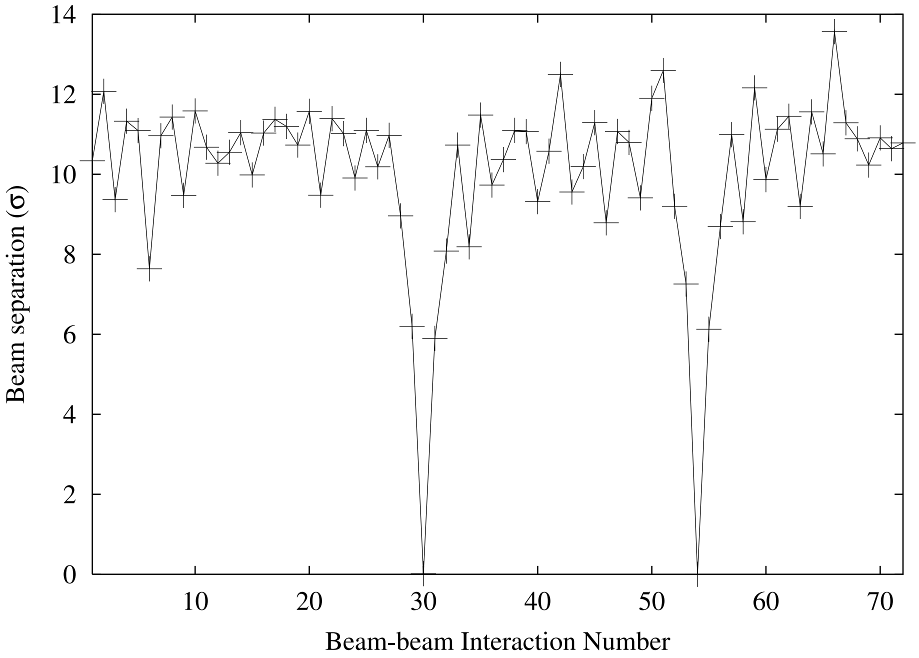

Figure 10: Separation between $\bar{p}$ bunch 6 and the opposing proton bunch at all 72 beam-beam interactions. The head-on collisions are at locations 30 (D0) and 54 (B0).

to

$$\Delta\nu_x(0,0) = \frac{N_b r_p}{4\pi\gamma_p\epsilon_x}\frac{2}{d_x^2+d_y^2}\left\{\frac{d_x^2-d_y^2}{d_x^2+d_y^2} + (d_x^2 + \frac{d_x^2-d_y^2}{d_x^2+d_y^2})\exp[-\frac{d_x^2+d_y^2}{2}]\right\}$$

$$\Delta\nu_y(0,0) = \frac{N_b r_p}{4\pi\gamma_p\epsilon_y}\frac{2}{d_x^2+d_y^2}\left\{\frac{d_y^2-d_x^2}{d_x^2+d_y^2} + (d_y^2 + \frac{d_y^2-d_x^2}{d_x^2+d_y^2})\exp[-\frac{d_x^2+d_y^2}{2}]\right\} \quad (4.5)$$

For round beams we observe that if θ is the angle between the zero amplitude location and the strong beam, the tune shifts $\propto \cos 2\theta$ and at most angles they decay primarily as the inverse square of the distance. The exception to this is on the 45° line $d_x = d_y$ where the tune shifts fall off exponentially with the square of the distance,

$$\Delta\nu_x = \xi\exp[-\frac{1}{2}d^2] = \Delta\nu_y\ , \qquad d = \sqrt{2}d_x = \sqrt{2}d_y, \qquad \text{along } 45^\circ \text{ line} \quad (4.6)$$

Thus *at a given separation, equal separations in both planes minimizes the tune shift when the beams are round*. When the beams are slightly eccentric so that the aspect ratio is $r = 1 + \delta r$, the location of the minimum tune shift is at [16]

$$\lim_{d\to\infty}\theta_{min} = \frac{\pi}{4} - \frac{1}{2}\delta r \quad (4.7)$$

for large beam separations d. The location of the minimum for arbitrary separations and aspect ratios may be found in the report by Erdelyi and Sen [16].

Figure 11 shows the beam-beam kicks from all 72 locations as phasors in the horizontal and vertical plane. In the horizontal plane, the two head-on collisions and the parasitic collisions immediately downstream of the IPs create the strongest kicks at zero amplitude. The two parasitics are close to being out of phase with each other. All other parasitics are smaller by at least an order of magnitude and so are barely visible on this phasor plot. Similarly in the vertical plane, the head-on collisions and the parasitics immediately upstream of the IPs are the strongest.

Due to the differences in long-range collisions, the tune footprint will differ from bunch to bunch. The nominal working point ($\nu_x = 0.585$, $\nu_y = 0.575$) is chosen to lie between fifth and seventh order resonances. At

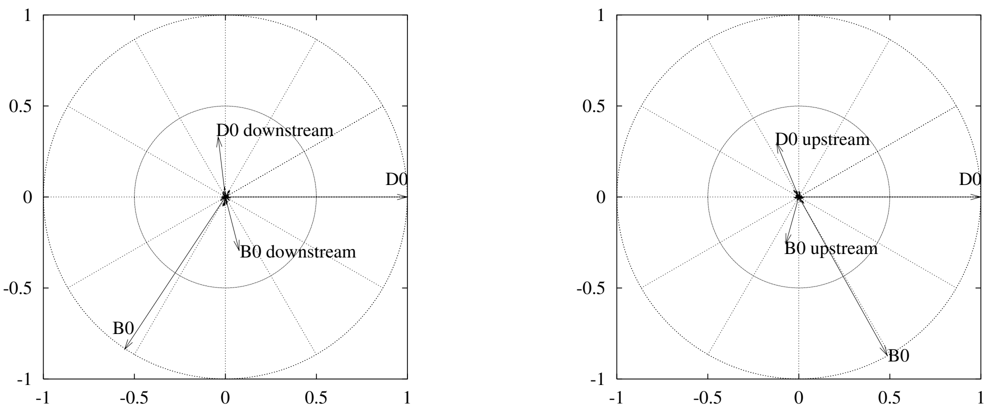

Figure 11: Phasor diagram representing the beam-beam kick on particles at zero amplitude. Left: horizontal kick, Right: vertical kick. The length of each phasor is the tuneshift due to this kick at zero amplitude. The angle of each phasor is the phase advance in the horizontal(left) or vertical (right) plane, modulo 2π, from D0. All 72 kicks are represented but only the head-on kicks at the IPs and the parasitic collisions nearest to the IPs are visible.

this working point the Tevaton beam straddles twelfth order sum resonances. Figure 12 shows the tune footprint for $\bar{p}$ bunch 6 in two cases. The addition of the long-range interactions increases the tune spread significantly and particles at amplitudes up to approximately 3σ now straddle the 5th and 10th order resonances. Inclusion of the IR errors does not change the footprint significantly. Bunches 1 and 12 at the ends of the train will be considered in Section 4.3.

Besides the footprint, another measure of nonlinearity used sometimes is the relative deviation from the linear Courant-Snyder invariant or smear. The region where the smear is less than 10% is then taken as a measure of the short term dynamic aperture. This makes sense with magnetic multipole nonlinearities where the short term and long term dynamic aperture do not differ very significantly. With beam-beam interactions, the smear is not a very useful indicator. Past tracking calculations, e.g. Reference [17], have shown that the dynamic aperture with long-range beam-beam interactions steadily decreases as the number of tracking turns decreases. Differential algebra tracking methods based on Taylor maps which reduce tracking times significantly with multipole nonlinearities are also not useful with beam-beam interactions. The fundamental reason is that a polynomial representation of the beam-beam force converges poorly to the true force. For the present, the beam-beam kick requires an evaluation of the error function although this can be speeded up by an approximate but still accurate error function evaluations.

The dynamic aperture is sensitive to the betatron phases and small changes in amplitude so we use between 100 to 200 particles to cover the phase space region of interest. With MAD, tracking these numbers of particles for 10^6 turns requires nearly a week on XX MHz Linux computers in the Beam Physics computing cluster. Consequently in most cases we follow particles for 10^5 turns and only for a few cases track for 10^6 turns. Faster codes and parallelization will enable us to reduce the tracking times in the near future.

A major question in dynamic aperture calculations is the connection to physical observables such as the lifetime. While a high dynamic aperture does not guarantee a good beam lifetime (too many processes which are important for the lifetime are not included in tracking calculations), it is most likely true that parameter choices which lead to a low dynamic aperture will also ensure poor beam lifetime. It is useful to recall that 10^6 turns corresponds to about 21 seconds in the Tevatron, so in the strict sense our tracking results represent phenomena over this time scale.

Calculation in 4D show that after 10^5 turns the average and minimum values of the dynamic aperture with the head-on interactions are (14.5, 12) σ respectively. With all the beam-beam interactions included, these values drop to (10, 9) σ respectively. These are to be compared with corresponding values of (15, 13)σ for the single beam. Figure 14 shows the dynamic aperture for the three cases as a function of the angle in coordinate space. The head-on interactions have only a slight impact but the addition of the long-range interactions reduces the stable region significantly.

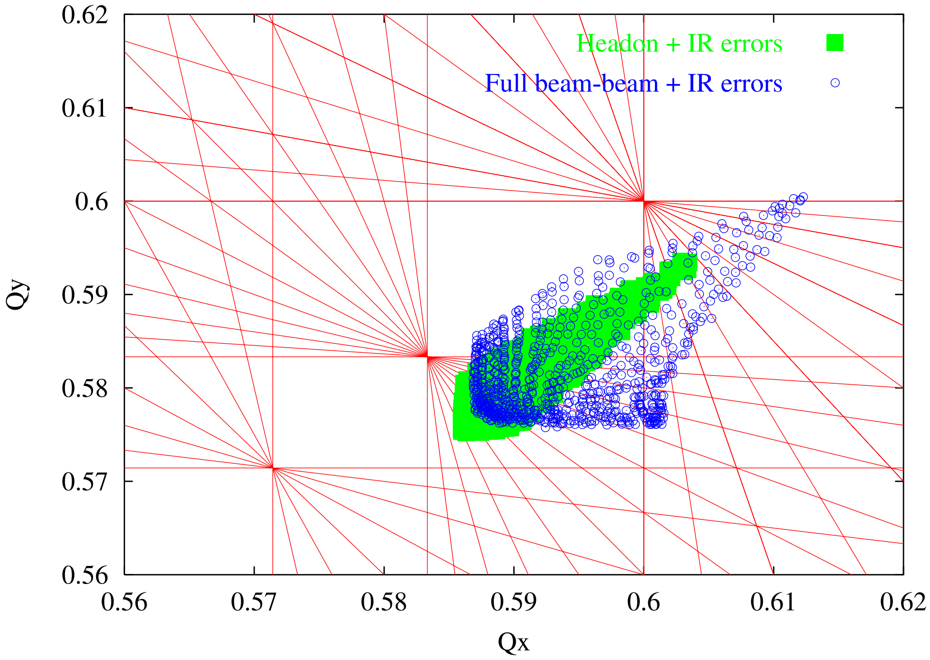

Figure 12: (color) Tune fooprint of $\bar{p}$ bunch 6 with (i)the head-on interactions and (ii) all the beam-beam interactions. IR errors and chromaticity sextupoles are included in each case. The footprint is shown for particles with amplitudes up to 7σ. Nearby fifth, seventh, tenth and twelfth order sum resonances are shown. The linear lattice tune is (0.585,0.575).

We found that if the contribution of dispersion is not included in the beam size of the proton beam, then the smaller and hence brighter proton beams reduce the dynamic aperture by roughly another σ. However for all dynamic aperture calculations reported here, the dispersion was included. Synchrotron oscillations introduce new dynamical issues which we consider next.

The results of Section 2 showed that for long bunches, the head-on beam-beam force is modulated by the longitudinal position of the particle. Strengths of transverse betatron resonances depend on the synchrotron amplitude and in addtion synchrotron sideband resonances are created around each betatron resonance. For example, Figure 1 shows the modulation of the betatron resonance widths by the longitudinal harmonic $L_{\vec{m}}$ as a function of the synchrotron amplitude.

Synchro-betatron resonances are also created when the chromaticity is non-zero. Beam stability requires that the linear chromaticity be corrected to a value near +5 at top energy. The long-range beam-beam force in the Tevatron creates an additional amplitude dependent chromaticity, pointed out by Alexahin [18]. The source of this chromaticity is the horizontal and vertical dispersion at the parasitic collisions which makes the beam separation depend on the momentum deviation $\Delta p/p$. The separations between an anti-proton with non-zero $\Delta p/p$ and the centroid of the proton beam are $(r_x + x_\beta, r_y + y_\beta)$ in the two planes. Here $r_x = \Delta x_{co} + \eta_x \Delta p/p$, $r_y = \Delta y_{co} + \eta_y \Delta p/p$, (η_x, η_y) are the horizontal and vertical dispersions respectively and (x_β, y_β) are the betatron amplitudes. Since the beam-beam force depends on the separations (r_x, r_y), the amplitude dependent betatron tunes now depend on $\Delta p/p$. An analytical study of the amplitude dependent chromaticities due to the long-range interactions may be found in the report by Erdelyi and Sen [16].

As a check of the analytical results, we calculated the amplitude dependent of chromaticity by tracking. At each transverse amplitude particles were launched at an angle of 45° and tunes were calculated as a function of $\Delta p/p$. The chromaticity at this amplitude was extracted from these tunes. Figure 13 shows the amplitude dependent chromaticities for three cases: (1) single beam only, (2) machine errors and the head-on beam-beam interactions and (3) machine errors and all beam-beam interactions. Without the beam-beam interactions, the chromaticities stay nearly constant at the desired value of +5 as expected. The head-on interactions cause the chromaticities to vary from about -5 units in both planes at small amplitudes to zero at large amplitudes. This

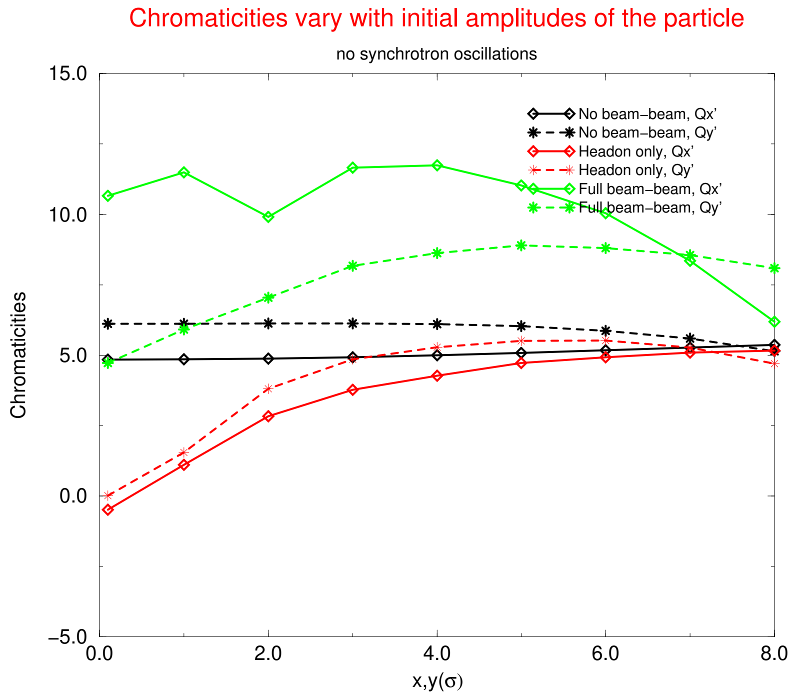

Figure 13: Variation of chromaticities with particle amplitude in pbar bunch 6.

contribution can be understood as a consequence of the dynamic beta effect. The head-on interactions change the maximum beta functions in the IR quadrupoles for example from (1116, 1099) m to (1340, 1347) m. This changes the chromaticity contribution of all the IR quadrupoles by about -10 units. The addition of the long-range interactions first reduces the dynamic beta effect so the beta functions around the ring are almost the same as with the single beam. They also cause, as predicted by the analysis, the horizontal chromaticity to vary from 6 to 12 units and the vertical chromaticity to vary from 5 to 8 units over the range of amplitudes shown. This additional chromaticity will enhance the synchro-betatron resonances driven by the beam-beam interactions.

Figure 14 shows the 4D and 6D dynamic aperture for three different cases. The head-on beam-beam interactions do not appear to be a major source of synchro-betatron resonances compared to those driven by the lattice itself. Both in 4D and 6D, the long-range interactions reduce the dynamic aperture substantially. The average and minimum values of the dynamic aperture are shown in Table 5. Extending the tracking to 10^6 turns shows that the minimum dynamic aperture drops to 4σ, close to the core of the beam. This may have a major impact on the luminosity. This is specially true because all the other effects not included in our tracking studies are likely to make the real dynamic aperture smaller than our calculated values.

We now examine the off-momentum tracking in more detail to identify the particular synchro-betatron resonances that excite the beam. One way to do this is with a synchrotron tune scan by changing the RF voltage. The method we choose here is to track particles first with constant momentum offsets by turning off the RF and then with momentum oscillations with the RF voltage at its usual value of 1MV. The difference will indicate the effects due to the synchrotron oscillations.

Figure 15 shows the dynamic aperture with and without synchrotron oscillations at a momentum deviation $\Delta p/p = 3 \times 10^{-4}$. At a few angles there is no difference but at several angles, the differences are equal to or greater than 2σ. We choose two angles 22.5° and 52.5° and at each angle we choose six particles with initial amplitudes between 9 and 10σ. We follow the evolution of the linear sum action $J_{sum} = J_x + J_y$ of these particles over 2048 turns first with the RF off and then with the RF turned on. We calculate the relative difference in the maximum sum action,

$$\frac{\Delta J_{sum}}{J_{sum}^{max}} = \frac{J_{sum}^{max}(\text{RF on}) - J_{sum}^{max}(\text{RF off})}{J_{sum}^{max}(\text{RF off})} \tag{4.8}$$

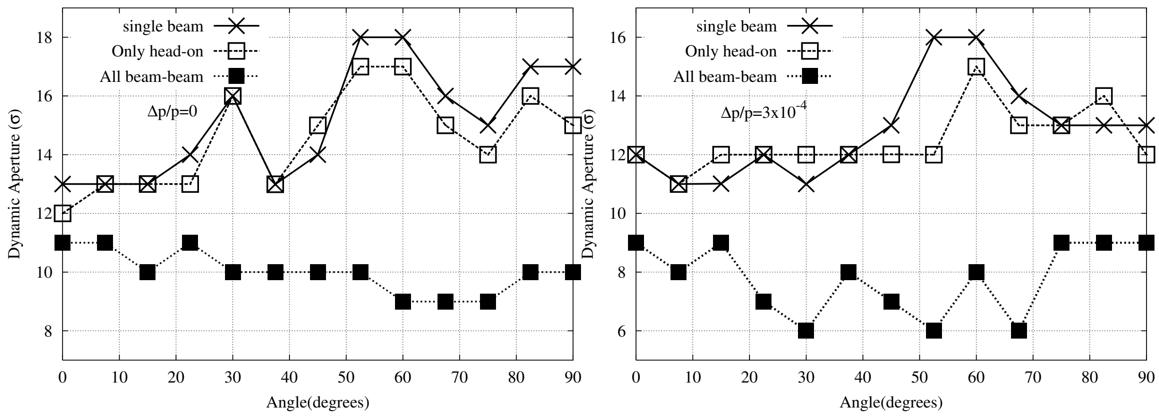

Figure 14: 4D (left figure) and 6D (right figure) dynamic aperture of pbar bunch 6 after 100,000 turns (about 72 synchrotron periods) as a function of angle in transverse coordinate space for three cases: (1) single beam, (2) machine nonlinearities and only the head-on beam-beam interactions and (3) machine nonlinearities and all beam-beam interactions.

	Average DA $\langle DA \rangle$	Minimum DA DA_{min}
dp/p = 0	10.0	9.0
dp/p=1×10^{-4}		
dp/p=3×10^{-4} (No RF)	8.6	8.0
dp/p=3×10^{-4}	7.7	6.0
	10^6 turns	
dp/p=3×10^{-4}	5.4	4.0

Table 5: The average and minimum 6D dynamic aperture after 10^5 and 10^6 turns with all beam-beam interactions and different values of $\Delta p/p$. This table also shows that at $\Delta p/p = 3 \times 10^{-4}$, synchrotron oscillations reduce the average dynamic aperture by about 1σ and the minimum by 2σ.

for each initial amplitude and angle. Here J_{sum}^{max}(RF off) for example is the maximum of the sum action over the 2048 turns with the RF turned off. This relative difference is the largest, around 40%, at an amplitude of 9.25σ and $52.5°$. We attribute this amplitude growth to a web of synchro-betatron resonances in this region of phase space.

To identify the individual synchro-betatron resonances responsible for amplitude growth, we searched for nearby resonances from the calculated tunes of each particle. The criterion to identify a nearby resonance was

$$|m_x\nu_x \pm m_y\nu_y \pm m_s\nu_s - n| \leq \Delta \equiv 0.01 \tag{4.9}$$

The nearness Δ to the resonance was arbitrarily set at 0.01. We restrict our search to betatron resonances up to twelfth order, $|m_x| + |m_y| \leq 12$, and their synchro-betatron sidebands up to third order, $|m_s| \leq 3$. At $\Delta p/p = 3 \times 10^{-4}$, the synchrotron frequency is $\nu_s =$??? (`FILL IN VALUE`) to be compared with $\nu_s = 7.2 \times 10^{-4}$ when $\Delta p/p \to 0$.

The tunes of each particle were also calculated by FFTs. Figure 16 shows the horizontal and vertical spectrum of the particle (at 9.25 σ and 52.5°) with the largest amplitude growth due to synchro-betatron resonances. With the RF off, the peaks are at tunes roughly 0.005 higher than the bare lattice tunes. This increase in tune is largely due to the machine chromaticity and the momentum offset $\Delta p/p = 3 \times 10^{-4}$. With the RF on, the peak of the horizontal spectrum moves to a lower tune and it is broader. This implies that the particle moved to a larger transverse amplitude and perhaps modulated between several amplitudes when the RF was turned on. Synchrotron oscillations also broaden the central peak in the vertical spectrum.

Amplitude (σ)	Angle (degrees)	Resonance Families (m_x, m_y); m_s	$\Delta J_{sum}^{max}/J_{sum}$
9.25	52.5	(1, -1); $m_s = -3, -2, -1$ (7, 5); $m_s = -2, ..., 3$ (8, 4); $m_s = -3$	0.42
10.0	52.5	(1, -1); $m_s = -3, ..., 3$ (3, 9); $m_s = -3, ..., 3$ (4, 8); $m_s = -3, ..., 0$	0.33
9.0	52.5	(1, -1); $m_s = -3, -2$ (8, 4); $m_s = -3, ...3$	0.18
9.25	22.5	(1, -1); $m_s = -3$ (8, 4); $m_s = -2, ...3$	0.14
9.0	22.5	(1, -1); $m_s = -3, -2$ (8, 4); $m_s = -3, ...3$	0.11
9.5	22.5	(1, -1); $m_s = -3$ (8, 4); $m_s = -2, ...2$	0.08
10.0	22.5	(1, -1); $m_s = -3, -2$ (7, 5); $m_s = 1, 2, 3$ (8, 4); $m_s = -3, -2, -1$	0.06
9.75	22.5	(1, -1); $m_s = -3$ (8, 4); $m_s = -3, ...2$	0.04
9.5	52.5	(1, -1); $m_s = -3$ (8, 4); $m_s = -3, ..., 3$	-0.02
9.75	52.5	(1, -1); $m_s = -3, -2, -1$ (7, 5); $m_s = -3, ..., 3$	-0.02

Table 6: Synchro-betatron resonance families associated with particles near the dynamic aperture. The resonance families are arranged in descending order of the relative change in action $\Delta J_{sum}^{max}/J_{sum}$.

Table 6 shows the resonances identified by this criterion. The entries in this table are arranged in descending order of amplitude growth due to the synchro-betatron resonances. Synchrotron sidebands of the coupling resonance $\nu_x - \nu_y = 0$ appear in every case along with sidebands of one or more of the twelfth order sum resonances. Other difference resonances or lower order sum resonances do not appear. At an amplitude of 9.25σ, the important sum resonances (m_x, m_y) are (7,5) and (8,4) together with their sidebands while at 10σ, the important resonances are (3,9) and (4,8) with their sidebands. Resonances where m_x, m_y are odd would not be driven by the head-on beam-beam interactions so their appearance shows again the importance of the long-range interactions and perhaps also the lattice nonlinearities. The particles shown in Table 6 are typically stable for tens of thousands of turns so the resonances shown in this table may be initially responsible for amplitude growth but they are not the ones ultimately responsible for particle loss. In Section 5 we will follow the evolution of tunes over longer times to trace the sources of particle loss.

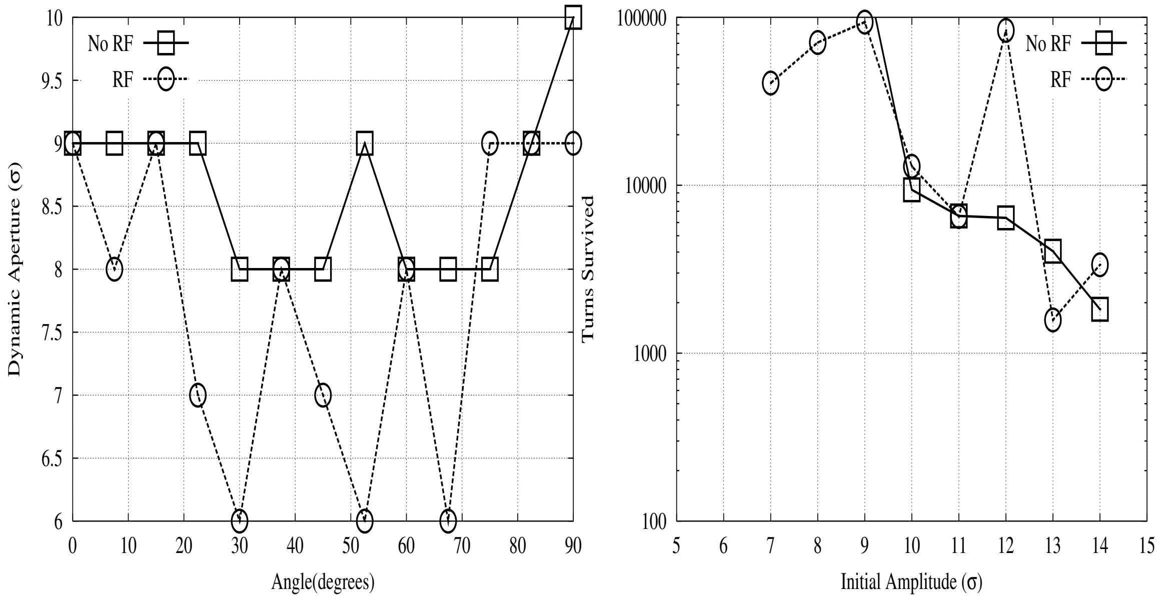

Figure 15: Left: Comparison of the dynamic aperture for particles with momentum deviations of $\Delta p/p = 3 \times 10^{-4}$ but without synchrotron oscillations (No RF) in one case and with synchrotron oscillations in the other case. At some angles, there are differences of 2-3 σ implying that the synchro-betatron resonances do have strong effects. Right: Survival time for particles at an initial angle of 52.5° with and without RF. Without the RF, particles at amplitudes $A_i \le 9\sigma$ survive 10^5 turns while with the RF, only particles at amplitudes $A_i \le 6\sigma$ survive 10^5 turns. At large amplitudes we observe that the differences in survival times are small except in one case where the particle at 12σ survives *longer* with the RF. This plot shows that the effects of the synchro-betatron resonances occur on time scales of the order of tens of thousands of turns or several synchrotron periods.

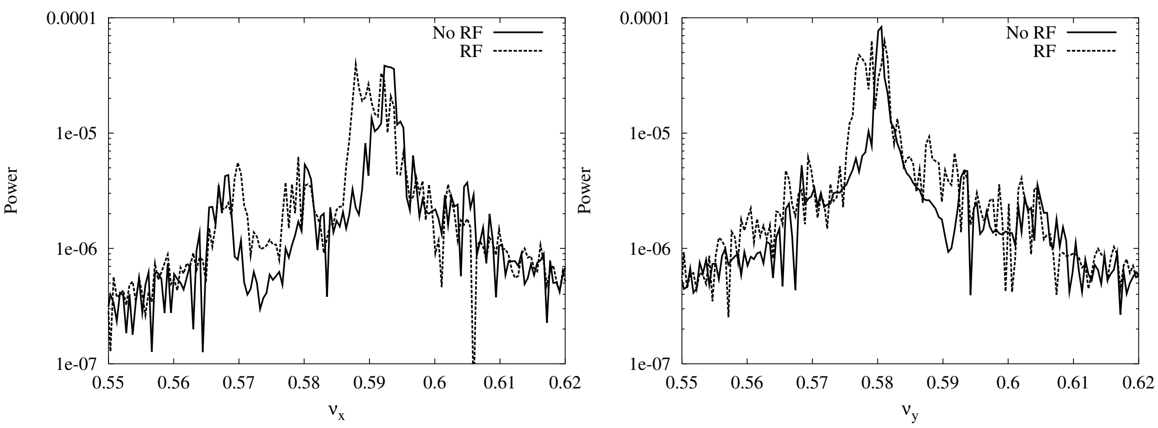

Figure 16: Power spectrum of the horizontal motion (left) and vertical motion (right) for the particle (at 9.25σ, 52.5°) which experiences the largest change in the action due to synchrotron oscillations.

4.3 Bunches 1 and 12

Footprints of all bunches except for bunch 1 and 12 are clustered around that of bunch 6. The major differences in the tuneshifts between bunches 1 and 12 and all other bunches are due to the missing parasitic collision closest to the IP, upstream for bunch 1 and dowstream for bunch 12. The first parasitic collision upstream of the IP has separations that are smaller in the vertical plane than the horizontal plane. These collisions therefore contribute more to the vertical tune shift. Since these collisions are missing for bunch 1, the vertical tune shift will be smaller for this bunch while the horizontal tunes will not be very different from that of bunch 1. Figure 17 shows the footprints due to the beam-beam interactions in Run IIa for bunch 1 and bunch 6 superposed on nearby sum resonances up to twelfth order. The differences are as expected. Small amplitude particles in bunch 1 see fewer fifth and tenth order resonances compared to similar amplitude particles in bunch 6. At large amplitudes the resonances spanned by the beam distribution are not very different for the two bunches.

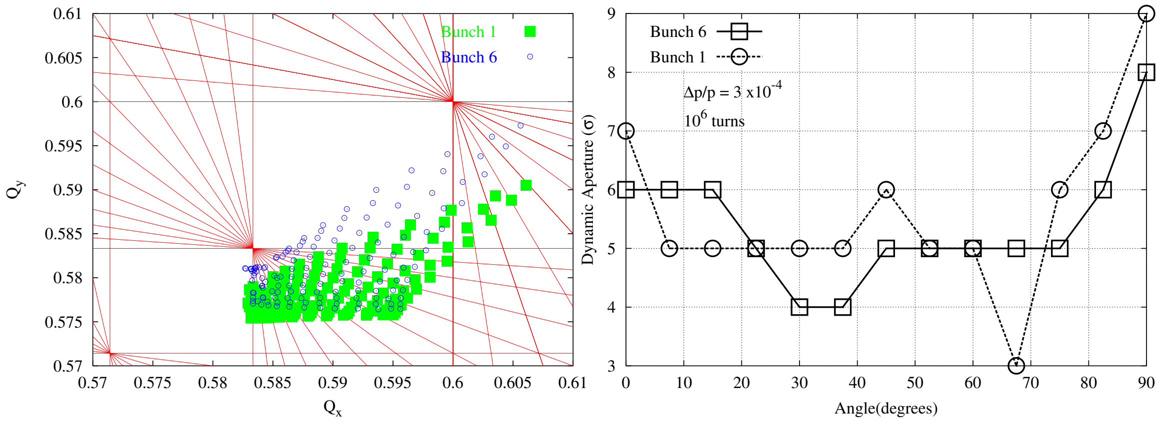

Figure 17: (color) Left: Tune footprint for bunches 1 and 6 in a train. Right: Dynamic aperture of bunch 1 and 6 after 10^6 turns. All particles had $\Delta p/p = 3 \times 10^{-4}$.

Figure 17 also shows the dynamic aperture for bunches 1 and 6 as a function of the initial angle in coordinate space after 10^6 turns. The average dynamic aperture is about the same: 5.6σ for bunch 1, 5.4σ for bunch 6. The minimum dynamic aperture for bunch 1 is 3σ compared to 4σ for bunch 6. In both bunches, motion close to the vertical axis appears to be more stable. Assuming that signifiant differences between the bunches do not manifest themselves at larger numbers of turns, we conclude from this similarity in dynamic aperture that the effects of the additional fifth and tenth order resonances spanned by bunch 6 at small amplitudes do not extend to larger amplitudes close to the dynamic aperture. This may also imply that for an individual bunch, the dynamic aperture is not very sensitive to small changes in the working point in this region of the tune diagram.

`REMARKS on BUNCH 12`

4.4 Tune scan

During a store lasting several hours the tune may drift due to various factors. As a consequence the lifetime may suffer if tunes close to the working point are on strongly driven resonances. Our calculations in the previous sections were done at the fixed tunes ($\nu_x = 0.585$, $\nu_y = 0.575$). In this section we will explore several tunes in the neighbourhood of this tune, both to find a better working point if possible and to determine the tune range beyond which the dynamic aperture falls off sharply.

We assume that coupling in the machine can be corrected to allow a minimum tune split of $|\nu_x - \nu_y|_{min} = 0.005$. Figure 18 shows the tune plane and a band around the diagonal depicting the forbidden region due to coupling. We choose tunes along lines parallel to the diagonal and outside this band. The trim quadrupoles TQFA4 and TQDD1 are used to change the lattice tunes. The tune changes are over a range of ± 0.01 compared to the lattice tunes of 20.585, 20.575. The perturbation to the linear optics, in particular the beta beat, is small. Appendix C shows the changes in the beta functions.

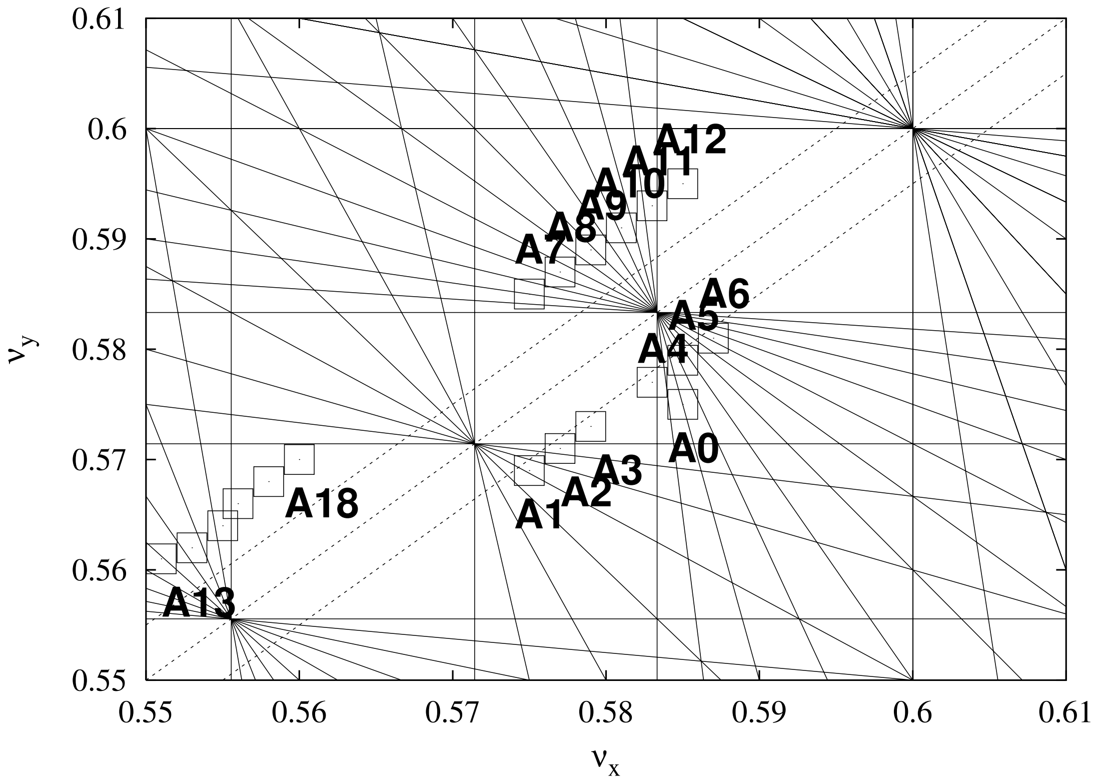

Figure 18: Sum resonances and the linear tunes, numbered A1 to A18, used in the tune scan. The nominal tune is tune A0. We observe that tunes A1, A2 span 7th order resonances, A4 to A11 span 12th order resonances, A12 is close to 5th order resonances while A13 to A16 are on 9th order resonances.

The dynamic aperture after tracking for 10^5 turns, both 4D and 6D ($\Delta p/p = 3 \times 10^{-4}$) were calculated at each of these tunes. The average and minimum values are shown in Table 7. At the tunes labelled A2 to A8, there is remarkably little variation in the dynamic aperture even though tune A2 is very close to the $7\nu_y$ resonance. Tune A1 is close to the $3\nu_x$+$4\nu_y$, $2\nu_x$+$5\nu_y$, ν_x+$6\nu_y$ resonances and here the dynamic aperture drops noticeably, indicating that one or more of these resonances are strongly driven. At tunes A9, A10 the 4D dynamic aperture is not too different from the preceeding tunes but the 6D dynamic aperture is smaller indicating that either the enhanced tune spread due to momentum offset and/or synchro-betatron resonances are important here. At tunes A11 and A12 which are closer to the 5th order resonances, the 6D dynamic aperture falls to very low values. This is most likely due to the increased tune spread. Tunes A13 to A18 are on the other side of the 7th order resonances. Here too the average 4D dynamic aperture is in the range from 10-11σ but the 6D dynamic aperture drops to low values at tunes A16-A18 due to the proximity of the 7th order resonances.

	Bare tunes	4D DA ($(\langle DA\rangle, DA_{min})$)	6D DA ($\delta_p = 3\times 10^{-4}$) ($(\langle DA\rangle, DA_{min})$)
A0	0.585, 0.575	(10.0, 9.0)	(7.8, 6.0)
A1	0.575, 0.569	(9.2, 7.0)	(5.1, 4.0)
A2	0.577, 0.571	(9.3, 8.0)	(7.5, 6.0)
A3	0.579, 0.573	(9.4, 9.0)	(8.1, 7.0)
A4	0.583, 0.577	(9.8, 9.0)	(7.6, 6.0)
A5	0.585, 0.579	(9.6, 8.0)	(7.5, 7.0)
A6	0.587, 0.581	(9.5, 8.0)	(7.5, 6.0)
A7	0.575, 0.585	(11.0, 9.0)	(8.6, 7.0)
A8	0.577, 0.587	(10.7, 9.0)	(8.4, 8.0)
A9	0.579, 0.589	(10.5, 9.0)	(7.6, 5.0)
A10	0.581, 0.591	(10.0, 8.0)	(7.0, 5.0)
A11	0.583, 0.593	(9.5, 6.0)	(4.8, 3.0)
A12	0.585, 0.595	(8.5, 6.0)	(1.9, 1.0)
A13	0.551, 0.561	(10.9, 9.0)	(7.2, 5.0)
A14	0.553, 0.562	(10.7, 9.0)	(6.2, 5.0)
A15	0.555, 0.564	(10.2, 9.0)	(7.2, 6.0)
A16	0.556, 0.566	(9.9, 8.0)	(5.7, 3.0)
A17	0.558, 0.568	(11.0, 9.0)	(5.4, 3.0)
A18	0.560, 0.570	(10.5, 8.0)	(5.4, 3.0)

Table 7: Dynamic aperture, both 4D and 6D, calculated after 10^5 turns at different tunes shown in Figure 18. All beam-beam interactions were included. A0 is the nominal tune, A1, A2, A17 and A18 are close to 7th order resonances while A12 is close to 5th order resonances. We observe that at tunes away from these low order resonances the dynamic aperture does not change significantly.

4.5 Importance of Parasitic Interactions

Of the seventy parasitic interactions, the four nearest to the IPs are at the smallest separations between 6-8 σ. Figure 11 showed that these parasitics create the largest tune shifts at zero amplitudes. When the centroid of the proton beam is at a distance of 6σ, anti-protons which are at amplitudes greater than 3σ can be in the core of the proton beam (depending on the sign of their displacement) and if so will be subject to strong beam-beam kicks. It is possible therefore that the effects of these nearest parasitics dominates the effects from the remaining sixtysix parasitics.

Table 8 shows the zero amplitude tunes with different beam-beam interactions. We notice first that the head-on interactions increase the tunes by slightly less than 2ξ=0.02. We attribute this difference to the beta-beat created by these collisions which also changes the tune. The nearest parasitics increase the tunes further by (0.007, 0.006) which are $> \xi/2$. The other parasitics change the tune by less than 0.001 at zero amplitudes.

	Zero amplitude tunes	Change ($\Delta\nu_x$, $\Delta\nu_y$)
No beam-beam	20.585, 20.575	-
Head on only	20.604, 20.594	(0.019, 0.019)
Head on and nearest parasitics	20.611, 20.600	(0.026, 0.025)
All beam-beam interactions	20.611, 20.600	(0.026, 0.025)
Head on, nearest parasitics at 10σ	20.607, 20.596	(0.022, 0.021)
Only the parasitics	20.590, 20.579	(0.005, 0.004)

Table 8: Zero amplitude tunes and the change from the bare lattice tune with different configurations of nonlinearities.

Table 9 shows some of the major optics parameters with different beam-beam interactions. There are significant differences in the maximum beta functions, for example, as the beam-beam interactions are added. `MORE COMMENTS HERE`.

	β_x^{max}, β_y^{max}	D_x^{max}, D_y^{max}	ν'_x, ν'_y	x_{co}^{max}, y_{co}^{max} [mm]
Head on and nearest parasitics	1220.4, 1230.5	7.63, 1.13		4.509, 4.056
Nearest PCs, 10σ separation	1267, 1281	7.64, 1.14	2.77, 1.59	4.52, 4.065
Only the parasitics	971.4, 953.2	7.6, 1.1	16.4, 10.2	4.55, 4.27

Table 9: Optics functions with different nonlinearities.

Figure 19 shows footprints with different beam-beam interactions. Compared to the head-on footprint, the nearest parasitics increase the tune spread at every amplitude. The difference in tunes increase at larger amplitudes. When all other parasitics are included the differences in small amplitude are negligible. The significant differences are only at large horizontal and small vertical amplitudes or vice versa. It is evident that the tune footprint is largely determined by the head-on collisions and nearest parasitics.

Does a larger footprint correlate with a smaller dynamic aperture? There appears to be some connection between the two with magnetic multipole nonlinearities. The force due to these multipoles increases monotonically with amplitude and can therefore transport particles out of the beam pipe. Beam-beam forces on the other hand first increase with amplitude to a maximum and then decay to zero at large amplitudes. While these forces do create a substantial tune spread, by themsleves thay cannot transport particles to very large amplitudes. Since both types of forces are present, the correlation between a tune footprint and stable region is not a priori obvious.

As with the footprints, we proceed with dynamic aperture calculations by first adding the head-on interactions to the machine nonlinearities. We find that the dynamic aperture changes very little due to these collisions even though the tune footprint increases significantly. For example with synchrotron oscillations and $\Delta p/p = 3 \times 10^{-4}$, the average and minimum dynamic aperture are virtually the same with and without these collisions. The results are summarized in Table 11. Next we add the nearest parasitics. Now there is a significant drop in the dynamic aperture. For example with synchrotron oscillations and $\Delta p/p = 3 \times 10^{-4}$, the average dynamic aperture drops by 3σ and the minimum by 4σ. These values are almost the same as with all the beam-beam interactions included.

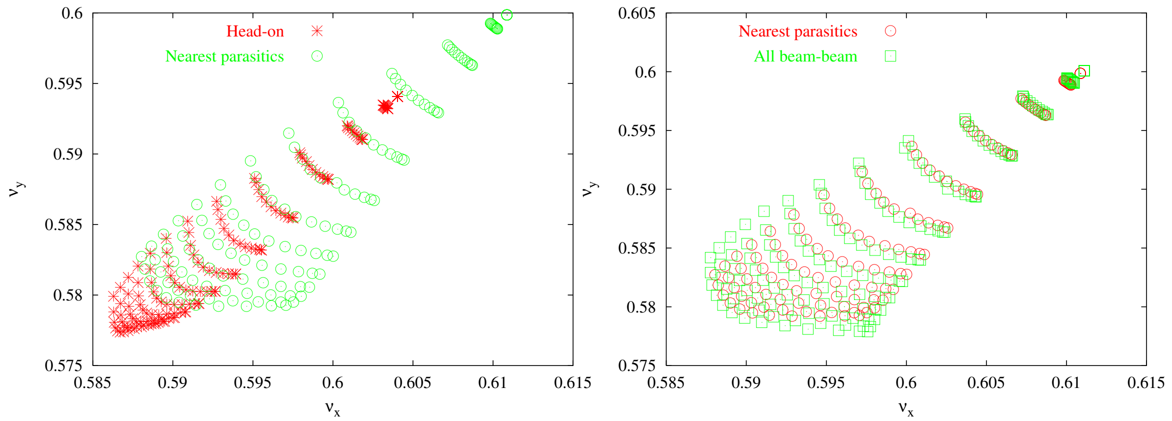

Figure 19: (color) Left: Footprints of anti-proton bunch 6 with only the head-on interactions compared with head-on and nearest parasitic interactions. Right: Footprint of anti-proton bunch 6 with head-on and nearest parasitic interactions compared with all the beam-beam interactions. The tunes are calculated at amplitudes of 0.5σ apart with zero amplitude at the top right corner. The footprint extends to an amplitude of 6σ. The lattice nonlinearities are included in each case.

4.5.1 Nearest Parasitics only

Figure 10 shows that at three of the parasitic interactions nearest to the IPs, the separations are about 6σ while at the fourth the separation is about 8σ. These separations are determined by the available separator voltages and locations and the need to ensure that the beams collide at B0 and D0. It may not be physically possible to change the separations at these locations by much. Nevertheless, since these are the dominant interactions, it is of interest to determine whether the dynamic aperture may be significantly improved by increasing the separations at these locations. This could be specially relevant in Run IIb when a crossing angle is introduced [1]. The separation at the nearest parasitic interactions will be determined by the crossing angle so a knowledge of the smallest acceptable separation may determine the smallest crossing angle necessary.

In our exploration the separation at each of the four parasitics was varied from 3-10 σ with equal separations at all locations. The angle between the beams ($\arctan D_y/D_x$) at each location however was kept the same as in the nominal Run IIa configuration. While there may be a dependence of the dynamic aperture on the angular orientation of the two beams (recall that the footprint is the smallest when the beams are at 45°), we have not explored this possibility in this study.

The left plot in Figure 20 shows the change in zero amplitude tunes compared to the case without any parasitics at different separations. A $1/d^2$ dependence would imply that the tune shifts at 10σ are about an order of magnitude smaller than at 3σ. We observe that the decay is slower than $1/d^2$. The right plot in Figure 20 shows the average and minimum dynamic aperture both in 4D and for particles with $\Delta p/p = 3 \times 10^{-4}$ after 10^5 turns as a function of the separation. In 4D tracking, the average DA jumps by nearly 1σ when the separation increases from 5 to 6σ while the minimum increases by 1σ when the separation increases from 6 to 7σ. In 6D tracking, the change in DA with separation is more gradual. Over the beam separation range from 3-10 σ, the average DA only increases from 9 to 10σ. The minimum DA stays constant at 8σ even as the separation is increased to 10σ. Thus even at relatively large separations the nearest parasitics reduce the minimum DA by 3σ compared to the case without parasitics.

This behaviour in 6D may be due to the amplitude dependent chromaticity generated by the parasitic interactions. Figure 21 shows the chromaticities ν_x', ν_y' as a function of transverse amplitude for different separations. The variation of ν_x' with amplitude depends strongly on the separation at small amplitudes. At a 3σ separation ν_x' decreases monotonically with amplitude while at a 10σ separation ν_x' increases to a maximum at an amplitude close to 4σ and then decreases. At amplitudes between 6-10 σ, ν_x' is almost independent of the separation. Similarly ν_y' at amplitudes between 6-10 σ is nearly independent of the separation although its variation with amplitude is quite different from that of ν_x'. The fact that ν_x', ν_y' at amplitudes greater than 6σ do not change much with beam separation may explain why the 6D DA is also relatively insensitive to the beam separation.

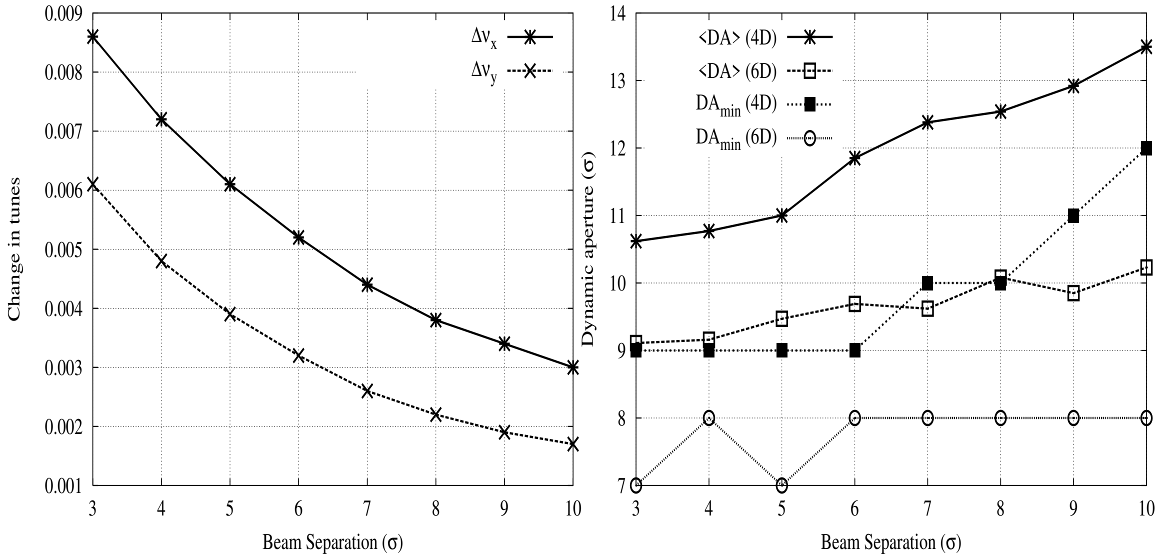

Figure 20: Tunes and dynamic aperture with the head-on interactions and the nearest parasitics. Left: Change in the zero amplitude tune due to the nearest parasitics compared to the case without any parasitics as a function of the separation at the nearest parasitics. Right: Average and minimum dynamic aperture in 4D and 6D ($\Delta p/p = 3\times10^{-4}$, 10^5 turns) as a function of the beam separation. In 4D the minimum DA increases when the separation is larger than 6σ while in 6D the minimum DA stays constant for separations between 6 to 10σ.

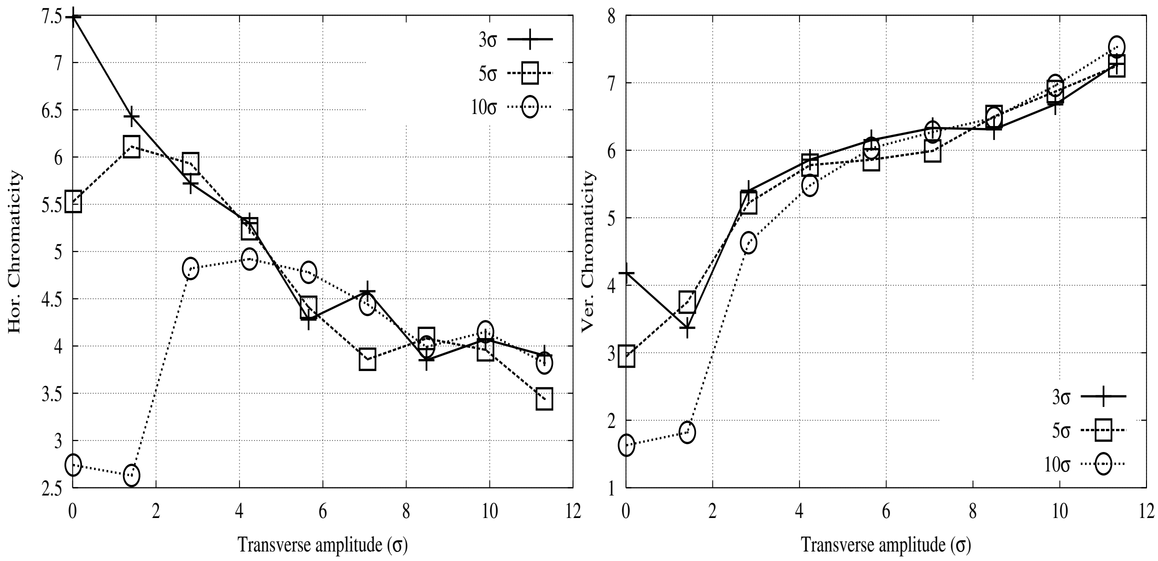

Figure 21: Amplitude dependent chromaticities with the nearest parasitics at different separations. Left: horizontal chromaticity as a function of the transverse amplitude for three different separations. Right: The vertical chromaticity as a function of amplitude.

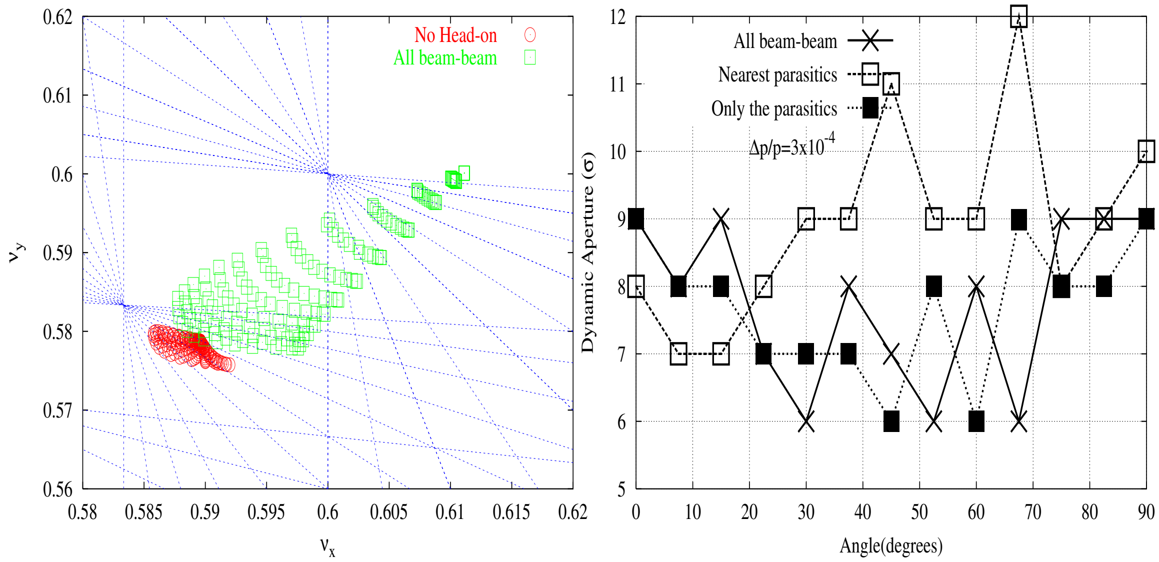

Figure 22: Left: (color) Footprint of anti-proton bunch 6 with (i) all parasitic interactions but no head-on and (ii) all the beam-beam interactions. The footprint extends to an amplitude of 6σ. The lattice nonlinearities are included in each case. Right: 6D dynamic aperture of pbar bunch 6 after 100,000 turns (about 72 synchrotron periods) for three cases: (1) all beam-beam interactions, (2) head-on and nearest parasitics and (3) only the parasitics.

4.5.2 Only the parasitics

In order to isolate the effect of the parasitic interactions, we consider a special but unphysical case where all the parasitic interactions are included but the head-on collisions are not. Without the dynamic beta-beat induced by the head-on collisions, the linear Twiss functions are different throughout the ring. For example, the maximum beta functions in the IR quadrupoles with all the beam-beam interactions are (1155, 1156)m while with only the parasitics, the maximum values are much smaller at (971, 953)m. This will in fact reduce the effect of the quadrupole nonlinearities in the latter case. However to keep the strength of the parasitic interactions unchanged we will use proton beam sizes at all locations the same as before.

The left plot in Figure 22 shows the footprint for this case compared with the footprint when all interactions are included. The sum resonances are also shown. With only the parasitics, the footprint is considerably smaller and does not cross any resonance of order lower than the twelfth. The dependence of the tune shift on amplitude is also different. For example, $\Delta\nu_x$ increases with vertical amplitude y at constant x but decreases with x at constant y. Thus the smallest horizontal tuneshift $\Delta\nu_x = 0.0008$ and largest vertical tuneshift $\Delta\nu_y = 0.005$ is at (6,0)σ while the largest $\Delta\nu_x = 0.007$ and smallest $\Delta\nu_y = 0.0007$ is at (0,6)σ.

Contrary to expectations, tracking reveals that, even with smaller beta functions in the IR quadrupoles and missing head-on collisions, the dynamic aperture is nearly the same as with all the beam-beam interactions. For example with 4D tracking, the average and minimum dynamic aperture are (10.2, 9.0)σ to be compared with (10.0, 9.0)σ with all the beam-beam interactions. The right plot in Figure 22 shows the 6D dynamic aperture vs angle for three cases. It is evident that the stable region is determined by the parasitic interactions - they completely dominate the effects due to the head-on collisions. The same plot in Figure 22 also shows that with the nearest parasitics regions close to the x-axis are least stable while regions close to the y-axis are most stable. When all the parasitics are included, the minimum dynamic aperture is now closer to the diagonal in coordinate space. This is most likely due to the change in resonance widths with angle when all other parasitics are included.

The sensitivity of this result to the working point was checked with a tune scan. The tunes in this scan are the same as those in the first scan reported in Section 4.4. The results of this scan are shown in Table 10. In almost all cases the dynamic aperture with only the parasitics is virtually the same as with all the beam-beam interactions.

How does one interpret this result? At most of the tunes in the scan, twelfth order resonances are nearby

	Bare tunes	4D DA - 10^5 turns	
		Only parasitics	All beam-beam
		$(\langle DA\rangle, DA_{min})$	$(\langle DA\rangle, DA_{min})$
A0	0.585, 0.575	(10.2, 9.0)	(10.0, 9.0)
A1	0.575, 0.569	(8.7, 7.0)	(9.2, 7.0)
A2	0.577, 0.571	(9.2, 8.0)	(9.3, 8.0)
A3	0.579, 0.573	(9.5, 9.0)	(9.4, 9.0)
A4	0.583, 0.577	(9.7, 9.0)	(9.8, 9.0)
A5	0.585, 0.579	(9.8, 9.0)	(9.6, 8.0)
A6	0.587, 0.581	(9.7, 9.0)	(9.5, 8.0)
A7	0.575, 0.585	(11.2, 10.0)	(11.0, 9.0)
A8	0.577, 0.587	(10.9, 10.0)	(10.7, 9.0)
A9	0.579, 0.589	(10.1, 9.0)	(10.5, 9.0)
A10	0.581, 0.591	(10.4, 9.0)	(10.0, 8.0)
A11	0.583, 0.593	(9.8, 8.0)	(9.5, 6.0)
A12	0.585, 0.595	(10.1, 8.0)	(8.5, 6.0)

Table 10: 4D Dynamic aperture with only the parasitics at different tunes compared with the dynamic aperture with all beam-beam interactions. There is very little difference between the two cases at most tunes. The tunes in this scan can be seen in Figure 18.

if not directly within the beam distribution. It is feasible that the widths of these resonances are determined completely by the parasitics. These resonances may be strong enough to drive particles to larger amplitudes where lower order resonances can transport them out of the chamber. This speculation that the resonance widths are determined by the parasitics will be checked analytically. Our tune scan is not exhaustive; it is possible that there are tunes in this tune space which are far enough from twelfth and lower order resonances that the smaller tune spread with only the parasitics does help to increase the stable region.

4.6 Summary of different cases

We summarize here our calculations of the dynamic aperture. Table 11 shows the dynamic aperture first for bunch 6 with different scenarios of beam-beam interactions and then the dynamic aperture for different bunches and more turns. With only a single beam, the calculated dynamic aperture (average and minimum) exceeds the physical aperture of 8σ set by the collimators. There is virtually no change in the dynamic aperture of a single beam as the number of turns is increased from 10^5 to 10^6. The head-on beam-beam interactions have only a small influence on the dynamic aperture even though they are the dominant contributors to the footprint. The parasitic interactions on the other hand increase the tune spread only slightly but completely determine the dynamic aperture. Thus we find that the dynamic aperture with only the parasitics and without the head-on interactions is virtually the same as that with both kinds of interactions. Amongst the parasitics, the ones nearest to B0 and D0 are at the smallest separations and are largely responsible for the drop in dynamic aperture. We find that increasing the separations at the nearest parasitics to 10σ increases the 4D dynamic aperture by 3σ but the 6D dynamic aperture increases by only 1 σ.

A tune scan in the vicinity of the nominal working point reveals that the dynamic aperture is relatively insensitive to the choice of tune until the tune approaches either the 5th, 7th or 10th order resonances.

When the tracking is extended from 10^5 to 10^6 turns we observe that unlike the single beam case, the dynamic aperture with beam-beam interactions drops further by 2σ. Both for bunch 1 and bunch 6, the dynamic aperture after 10^6 turns is close to the core of the beam. Bunch 1 has a minimum dynamic aperture about 1σ smaller than that of bunch 6. Under the conditions assumed in the model, this predicts that at design parameters both the lifetime and the luminosity could be adversely affected.

Figure 23 shows the survival plot for three cases: single beam, bunch 1 and bunch 6. In each case, the stable amplitude along the most unstable angle in coordinate space is shown. This survival plot is another representation of the fact that after 10^5 turns the stable region for the single beam does not change much while with beam-beam interactions, the stable region diminishes with time.

Bunch 6: $\nu_x = 0.585$, $\nu_y = 0.575$ DA after 10^5 turns		
	$(\langle DA \rangle, DA_{min})$ [4D] $\Delta p/p = 0$	$(\langle DA \rangle, DA_{min})$ [6D] $\Delta p/p = 3 \times 10^{-4}$
IR errors	(15.2, 13.0)	(12.9, 11.0)
Head-on and IR errors	(14.5, 12.0)	(12.5, 11.0)
Head-on, nearest PCs, IR errors	(10.5, 9.0)	(8.9, 7.0)
Head-on, nearest PCs at 10σ, IR errors	(13.5, 12.0)	(10.2, 8.0)
Only the parasitics, IR errors	(10.2, 9.0)	(7.7, 6.0)
All beam-beam, IR errors	(10.0, 9.0)	(7.7, 6.0)
$(\langle DA \rangle, DA_{min})$ for bunches 6, 1 and 12 [6D, $\Delta p/p = 3 \times 10^{-4}$]		
	10^5 turns	10^6 turns
Single beam	(12.9, 11.0)	(12.3, 11.0)
Bunch 6: all beam-beam	(7.7, 6.0)	(5.4, 4.0)
Bunch 1: all beam-beam	(7.8, 6.0)	(5.6, 3.0)
Bunch 12: all beam-beam	()	

Table 11: The average and minimum 6D dynamic aperture with various configurations of beam-beam interactions. Note that the dynamic aperture with only the parasitics is nearly the same as that with all the beam-beam interations. The head-on interactions therefore are dominated by the parasitics. Also shown are the average and minimum 6D dynamic aperture for bunches 1 and 12 at the edges of the bunch train compared with bunch 6 in the middle of the train.

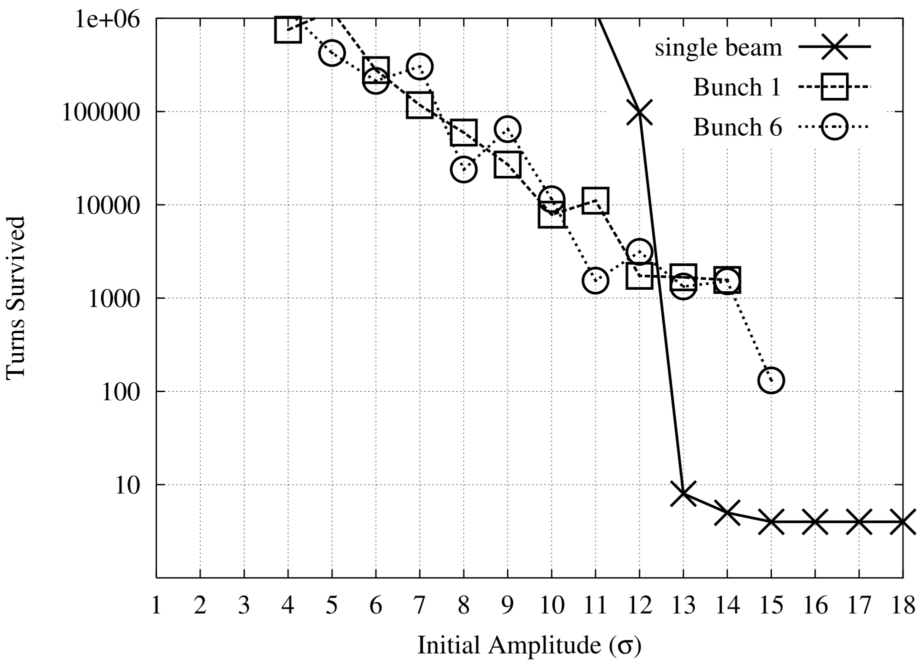

Figure 23: Survival plots for three cases along the most unstable angle in each case. In each case, particles were given a momentum deviation of $\Delta p/p = 3 \times 10^{-4}$. For the single beam, the stable region stabilizes after about 10^5 turns. With the beam-beam interactions, the stable area appears to progressively diminish with time.

5 Transport mechanisms of amplitude growth

Tracking calculations in the previous section have established the dynamic aperture both on and off momentum. Here we will study the mechanisms responsible for transporting particles out of the stable region. First we will identify the important betatron resonances and then characterize the motion in a thin band around the stable boundary.

5.1 Important Resonances

We chose to identify the betatron resonances at amplitudes of 6 and 7σ. Particles at these amplitudes are stable for at least 10^5 turns and their tunes can be calculated with FFTs. We fix the vertical tune and scan in the horizontal tune. At each tune the maximum amplitude reached by the particle over 1024 turns is recorded.

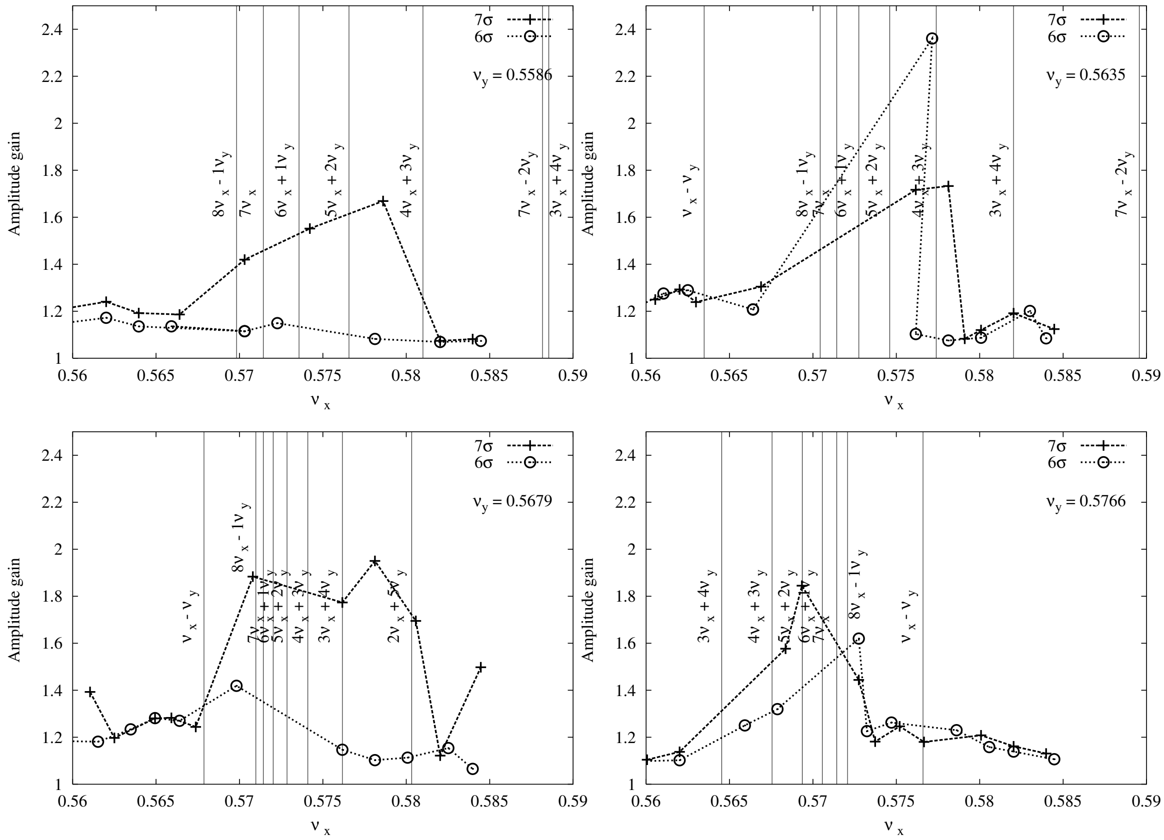

Figure 24: Tune scans around resonances and the amplitude growth in the vicinity of these resonances. See the text for comments.

Figure 24 shows the results of several resonance scans. The tunes shown are the tunes of individual particles at 6σ and 7σ and not the zero amplitude tunes. The ratio of the maximum to initial amplitude (or the relative amplitude gain) is shown in each case as well as the nearby sum and difference betatron resonances up to tenth order.

At these amplitudes, the seventh order sum resonances, the linear coupling resonance $\nu_x - \nu_y$ and two ninth order difference resonances: $8\nu_x - \nu_y$ and $7\nu_x - 2\nu_y$ are identified. These can be driven by the long-range interactions but not the head-on interactions. With one exception the relative amplitude gain at the different choices of vertical tunes ν_y is larger at 7σ than at 6σ. The exception is at $\nu_y = 0.5635$ where the amplitude of the particle initially at 6σ increases 2.4 times close to the $4\nu_x + 3\nu_y$ resonance. Relative amplitude gains of more than a factor of two will drive these particles out of physical aperture so these resonances can be responsible for beam loss. In most cases the largest growth is near the $5\nu_x+2\nu_y$ and $4\nu_x+3\nu_y$ resonances. The $7\nu_x$ and $8\nu_x-\nu_y$ resonances are close together and this pair is also associated with significant growth. The difference resonance $\nu_x - \nu_y$ is isolated from the other resonances seen here and does not seem to be associated with significant growth. These results suggest that a correction scheme which compensates the seventh order sum resonances may be useful.

We should also point out that the resonances identified above were purely transverse. Synchro-betatron resonances, some of which are identified in Section 4.2, can also lead to particle loss and may determine the stable region on longer time scales.

5.2 Diffusion near the stable boundary?

In a report on the long-range interactions in the SSC [19] Irwin had proposed the concept of a *diffusive dynamic aperture* (DDA). The boundary of this aperture was defined as an amplitude where the variance in amplitudes grows by an amount equal to the initial beam emittance over a store. If the motion at this boundary is purely diffusive, the variance would grow linearly in time,

$$\sigma_A^2(N) = \sigma_A^2(0) + \alpha N \tag{5.1}$$

where $\sigma_A^2(0)$ is the initial variance, N is the number of turns and α characterizes the strength of the diffusion. At the DDA. $\alpha N_S = \epsilon_0$ where N_S is the duration of the store in turns and ϵ_0 is the initial emittance.

The model of interactions in the SSC was similar to the one in the proposed LHC where all the long-range interactions occur within the interaction region (IR). The beam separation created entirely by the crossing angle is the same, 7.5σ, at all parasitics and they are all nearly in phase. Tracking calculations in this model showed that at an amplitude of 7σ, the variance grew linearly in time while at smaller amplitudes there was no growth in the variance. When tune modulation was added, this diffusive boundary dropped by another 2.5σ. These results led to the following parametrization:

$$\text{DDA} = D - \Delta(N_b, N_{PC}) \tag{5.2}$$

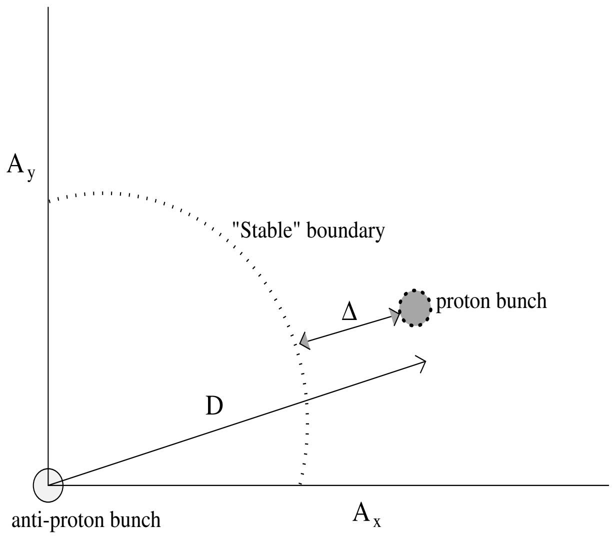

Figure 25: Assuming that the parasitics can be represented by interactions at some “average” separation D, the stable boundary $< D$ by an amount Δ which depends on the bunch intensities and the number of parasitics.

This is illustrated in Figure 25. The DDA is smaller than the average separation D by an amount Δ which depends on the bunch intensity N_b and the number of parasitics N_{PC}. Δ was found to be independent of D in the tracking. Tracking calculations for the LHC reported in [20] using a model similar to Irwin's also found a boundary at which there was a diffusive growth in the amplitude.

In the Tevatron the parasitic interactions are neither all in phase nor are the separations constant. Nevertheless as our calculations in the previous section have shown, the dynamic aperture is mostly determined by the parasitics nearest to the IPs where the separations are as small as 6σ. To determine whether there exists a diffusive boundary in our case, we followed the the square root of the variance (called the spread ΔJ) in time at several different amplitudes. The machine tune was fixed at the nominal values of (0.585, 0.575). We took 100 particles at each amplitude distributed uniformly in angle, atan(y/x), in order to remove the dependence on initial conditions. The spread is averaged over $N_t = 1024$ turns in order to remove the effects of resonance islands which can make the action vary from turn to turn. Thus,

$$\Delta J \equiv \langle \sigma(J_{sum}) \rangle = \frac{1}{N_t} \sum_{k=1}^{N_t} \sigma_k(J_{sum}) \tag{5.3}$$

where $\sigma_k(J_{sum})$ is the standard deviation at turn k of the sum action J_{sum} amongst $N_P = 100$ particles.

First we calculated the spread in action ΔJ as a function of the initial amplitude. Figure 26 shows the spread for two cases: (i) with all the beam-beam interactios and (ii) with only the parasitic interactions. In both cases the spread ΔJ increases faster than quadratically with amplitude. However the nonlinearity due to the head-on collisions clearly contribute to a larger spread at all amplitudes.

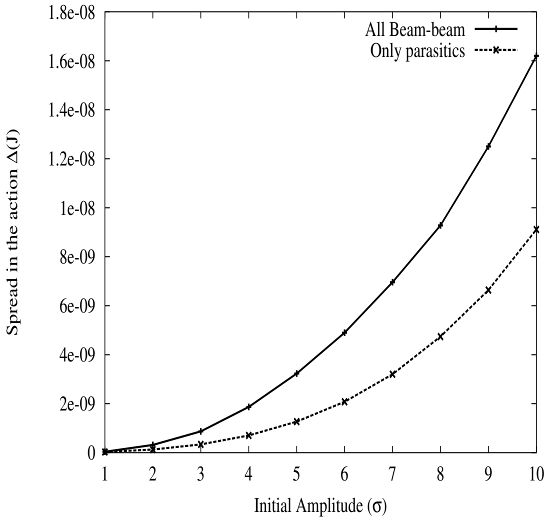

Figure 26: The spread ΔJ of the sum action amongst 100 particles at the same initial amplitude A_i as a function of A_i. ΔJ increases faster than quadratically with A_i in both cases.

Next we chose three initial amplitudes 7, 8 and 9 σ which are below the 4D dynamic aperture calculated to be 10σ after 10^5 turns. After each 10^4 turns, the average sum action and the ΔJ was calculated. In this tracking, coordinate space was covered more densely than in our dynamic aperture calculations. As a consequence we found that three particles at 9σ were lost during the course of the 10^5 turns. None were lost at smaller amplitudes. The left plot in Figure 27 shows the evolution of the spread ΔJ with time for these three amplitudes with all beam-beam interactions included. Also shown are the turns where particles are lost. If the growth in action were diffusive, the spread $\Delta J \propto \sqrt{N_t}$ where N_t is the number of turns. After an initial increase, ΔJ at 7 and 8 σ stays nearly constant. Even at 9σ ΔJ increases before a particle is lost but after it is lost, ΔJ returns to earlier values. Therefore *there is no evidence of diffusive growth at any amplitude*. The right plot in Figure 27 shows the results with only the parasitics. Again three particles initially at 9σ are lost. There is no evidence of diffusive motion in this case either.

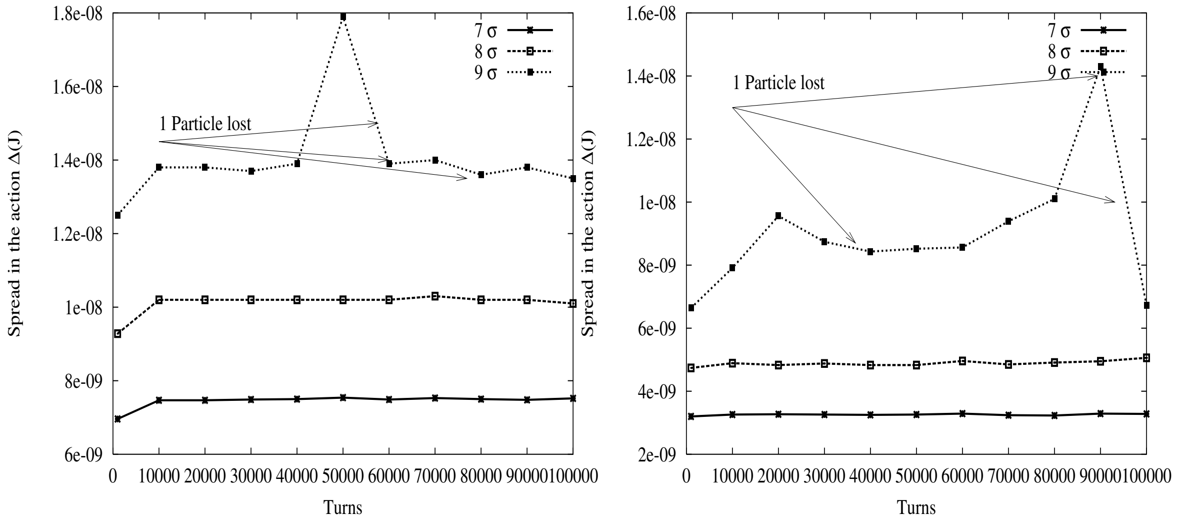

Figure 27: Left: The spread ΔJ as a function of time for different initial amplitudes A_i. All beam-beam interactions are included in this case. Arrows indicate times when particles were lost, here they were lost only for $A_i = 9\sigma$. There is no evidence of diffusive behaviour at any amplitude. Right: Same as in the left figure but with only the parasitics.

Tune changes of these particles were also followed. After every 10^4 turns the tune of each particle was calculated. The sum of the absolute differences after $k \times 10^4$ turns,

$$\Delta\nu(k) = |\nu_x(k) - \nu_x(k-1)| + |\nu_y(k) - \nu_y(k-1)| \,, \qquad k = 1, 2, ...10 \tag{5.4}$$

was calculated at each k. At 7 and 8σ where no particles are lost, the tune changes were of the order of 10^{-5} or less, smaller than the resolution of the FFT. Particles that were lost at 9σ had significantly larger changes in tune even at several 10^4 turns prior to being lost. For each lost particle we also tracked the tune change of a neighbouring particle separated by 3.6° but at the same amplitude. These neighbouring particles had much smaller changes in tune.

The left plot in Figure 28 shows the evolution of the tunes of the lost particles at intervals of 10^4 turns. The tune of particle L1 for example changes by more than 0.002 over the last 10^4 turns before being lost while L2 on the other hand suffers a tune change of more than 0.001 over the first 10^4 turns but is not lost until after 7×10^4 turns. In this plot the tunes of all three particles lost are still close to only the 12th order resonances and have not yet migrated to lower order resonances. As seen in the previous subsection, once particles are close to lower order resonances such as the 7th they would be lost within 10^3 turns. The right plot in Figure 28 shows $\Delta\nu(k)$ for the three lost particles and for their neighbours which survive all the 10^5 turns. We observe that in this model tune changes greater than 0.001 seem to be a precursor to eventual loss. Figure 29 shows the same plots but with only the parasitics. The results are similar - tune changes greater than 0.001 predict eventual loss.

The motion near the stable boundary while not diffusive may be chaotic. The classic signature of chaos is a sensitive dependence on initial conditions. A rigorous demonstration of chaotic motion requires the calculation of the Lyapunov exponent λ defined via

$$d(t) = d(0)e^{\lambda t} \tag{5.5}$$

where $d(t)$ is the distance between two initially neighbouring particles. Positive Lyapunov exponents (one for each degree of freedom) imply chaos. Some tracking programs, such as Sixtrack, follow pairs of initially close particles and look for exponentially fast separation to identify the onset of chaos. In the studies reported here we have used MAD so to test the hypothesis of chaos we examine the survival time in bands at two different amplitudes. One band was chosen between 14-15 σ with 72 particles spaced uniformly apart in amplitude by 0.014 σ ($\sim$ 0.5 μm) within the band. The other band had similarly spaced particles between 10-11 σ. These particles were tracked for 10^5 turns and their survival times recorded. Figure 30 shows the survival time plot with a coarse sampling of particles - one particle at each amplitude from 9 - 18 σ. The survival time increases from 100 turns at 18σ to 10^5 turns at 10 σ. Figure 31 shows the results with the finer grained sampling at 10σ and 14σ mentioned above. In the band between 10-11σ, the survival time fluctuates wildly from particle to particle - e.g. one particle survives for only 10^4 turns while a neighbouring particle only 0.014σ away survives for at least 10^5 turns. Thus in the band close to the DA, the motion depends sensitively on the initial coordinates and is likely to be chaotic. By contrast, at larger amplitudes between 14 and 15 σ, the majority of particles are lost within 10^4 turns and the dependence on initial coordinates is much weaker. At the larger amplitudes therefore, the motion is likely not chaotic but instead there is a fast streaming outwards to the beam pipe.

Together the absence of widescale diffusion near the dynamic aperture and the results in these figures lend support to the picture of thin chaotic layers close to the dynamic aperture which makes the motion of individual particles chaotic. These thin layers provide channels which can transport particles out to large amplitudes. Over longer time scales than those followed in our tracking studies, say minutes or hours, other particles close to the stability boundary may also be guided into these channels and transported out of the beam pipe.

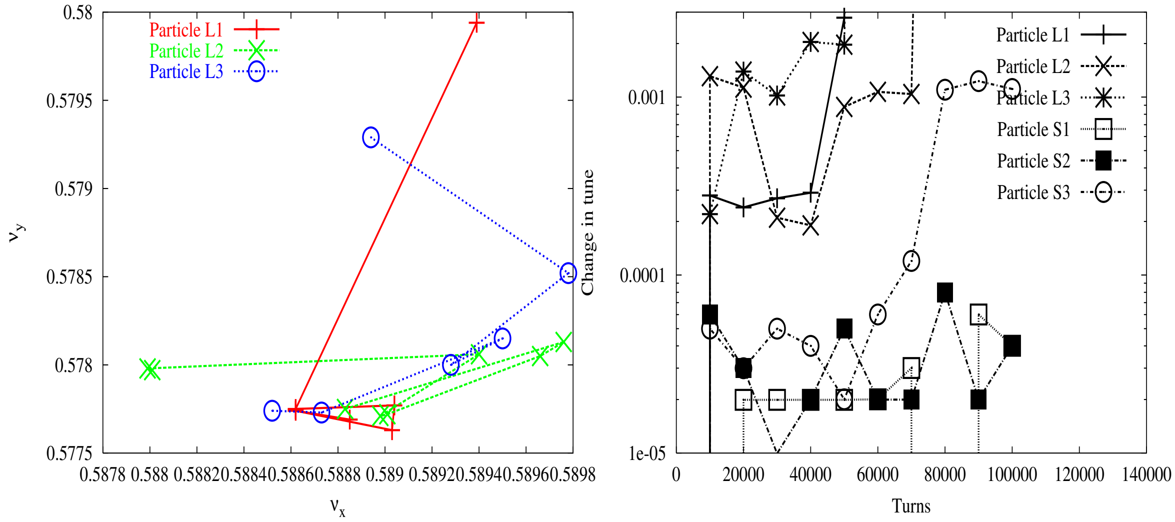

Figure 28: (color) Tune changes of selected particles at 9σ with all beam-beam interactions. Left: Particles L1, L2, L3 all at 9σ were lost during the course of tracking over 10^5 turns. The tunes of these particles, calculated every 10^4 turns, are shown prior to being lost. These tunes change abruptly from their original values but have not yet migrated to resonances lower than the 12th order. Right: Particles S1, S2 and S3 also at 9σ are separated from 1, 3 and 5 respectively by 3.6° but these particles are not lost. Change in the absolute value of the tune of these six particles is shown as a function of turns. Particles with tune changes greater than 0.001 are eventually lost.

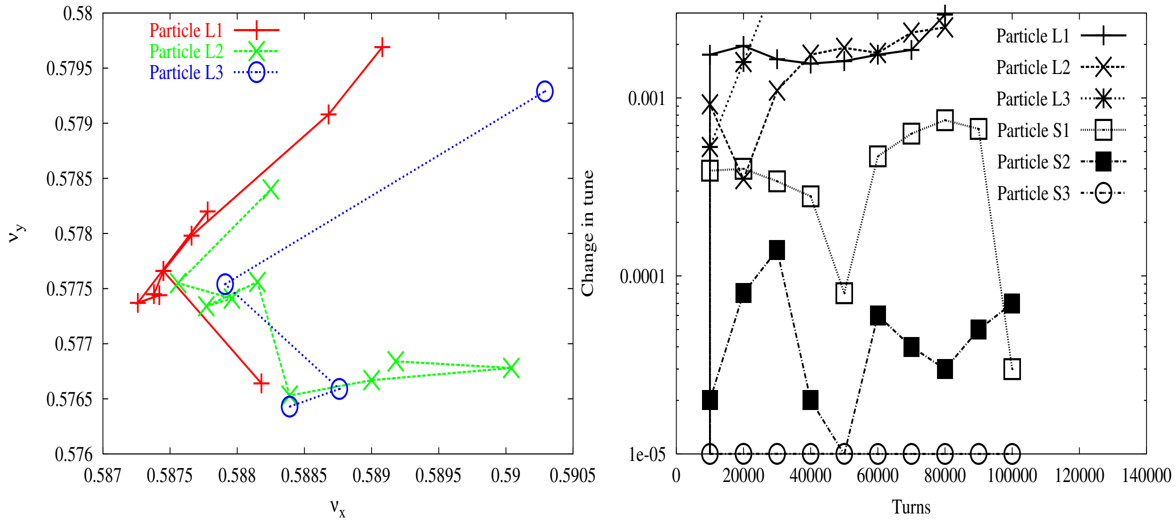

Figure 29: Same as Figure 28 but with only the parasitics.

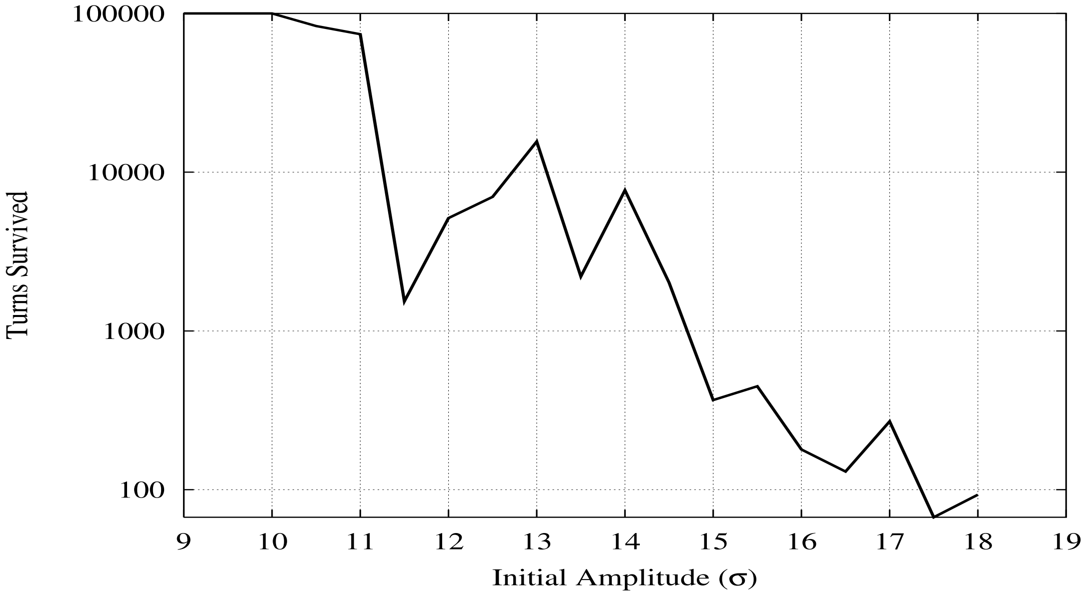

Figure 30: Survival plot for particles tracked for 10^5 turns with initial amplitudes between 9 and 18 σ. The ordinate is plotted on a logarithmic scale. A closer look at the number of turns survived is shown below for particles with amplitudes between 10 and 11 σ and between 14 and 15 σ respectively.

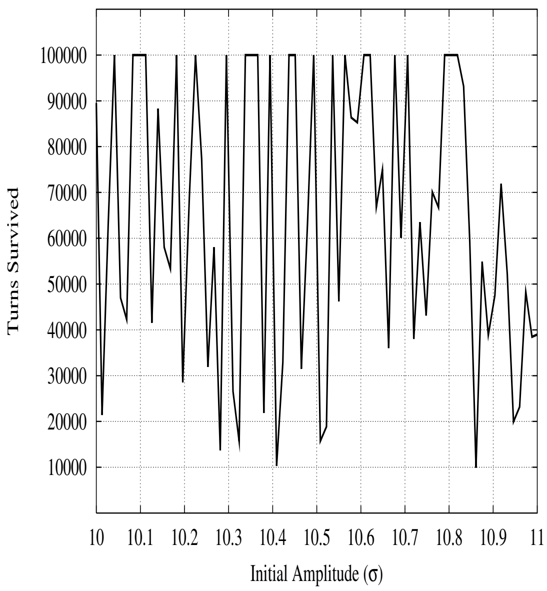

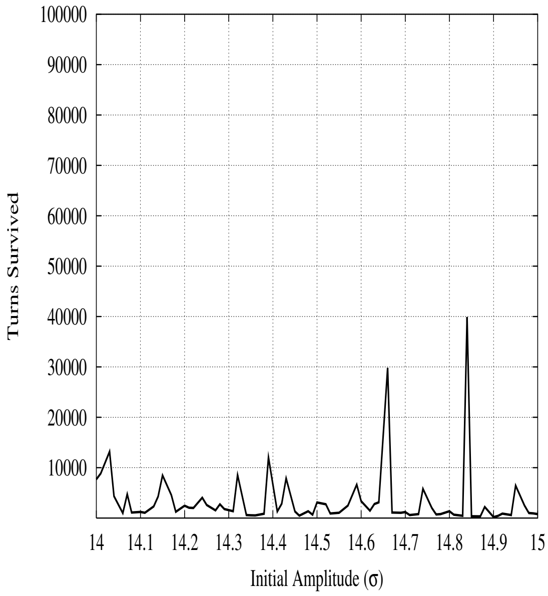

Figure 31: Left: Survival plot for particles with initial amplitudes between 10 and 11 σ. Right:The survival plot for particles between 14 and 15 σ. The spacing between adjacent particles is about 0.014 σ. In both cases particles were tracked for 10^5 turns. The large fluctuations in the band between 10-11 σ suggest that motion in this band is chaotic.

6 Impact of a Crossing Angle

Increasing the luminosity beyond that obtained in Run IIa will require that the bunch spacing decrease to 132 nsecs from the present 396 nsecs and the number of bunches increase from the present 36 per beam to more than a hundred in each beam [1]. This is necessary in order to limit the number of pp inelastic events per bunch crossing to less than three. The shorter bunch spacing introduces a number of beam dynamics issues that have to be considered. One of these is that the parasitic collisions nearest to the IPs now occur before the electrostatic separators since the parasitic interactions will occur at distances about 20m apart. A crossing angle at the IP is needed to separate the beams at these locations. A half crossing angle of about 200 μradians in the 45° plane separates the beams by about 4σ at these nearest parasitic collisions. The crossing angle in turn has several other consequences, chief among them is the loss of luminosity at the main IPs. Assuming that the half crossing angle is ϕ, the loss in luminosity due to the crossing angle is determined from

$$\mathcal{L}(\phi) = \mathcal{L}(0)[1 + (\frac{\phi \sigma_s}{\sigma_\perp})^2]^{-1/2} \tag{6.1}$$

where σ_s is the rms bunch length and $\sigma_\perp$ is the transverse beam size at the IP. The loss in geometrical overlap between the beams also reduces the beam-beam parameter. Assuming that the beam-beam parameter is defined by the effective beam sizes and the crossing plane is at 45° so that the crossing angles in the horizontal and vertical planes are equal $\phi_x = \phi_y = \phi/\sqrt{2}$,

$$\begin{aligned}\xi_{eff} &= \frac{N_b r_p}{2\pi\gamma_p}\frac{\beta_x^*}{\sigma_{x,eff}^*(\sigma_{x,eff}^* + \sigma_{y,eff}^*)} \\ &= \frac{\xi}{1+\chi_x^2}, \qquad\qquad \chi_x = \frac{\phi_x \sigma_s}{\sigma_x}\end{aligned} \tag{6.2}$$

The left plot in Figure 32 shows the loss of luminosity and the reduced beam-beam parameter as a function of

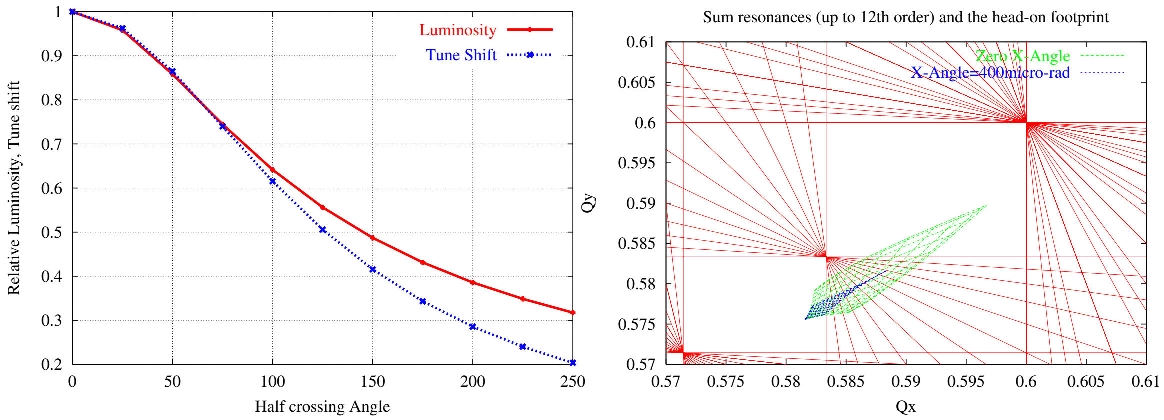

Figure 32: Left: (color) The impact of a crossing angle (in the 45° plane) on the luminosity and the beam-beam parameter. All values are normalized to the value at zero crossing angle. At a half crossing angle of 200μ radians, the luminosity is reduced to 40% of its value without a crossing angle. Right: (color) The beam-beam tune footprint for amplitudes to 6σ shown with only the main collisions at B0 and D0 for two cases: without a crossing angle and with a total crossing angle of 400μradians. The footprints are superposed on the sum resonances up to twelfth order.

the crossing angle. The right plot in Figure 32 shows the beam-beam tune footprints due to the main collisions at B0 and D0 for two cases: (1) without a crossing angle and (2) with a half crossing angle of 200μradians. With this crossing angle, there is a sharp reduction in the footprint and the number of resonances spanned by the beam distribution is also reduced. However as is well known, the crossing angle couples the longitudinal dynamics to the transverse and excites synchro-betatron resonances. In addition, particle orbits with crossing angles go through the IR quadrupoles at larger amplitudes and therefore experience more nonlinear fields. These fields can also reduce the dynamic aperture even without coupling from longitudinal fields.

Using a stand alone code we will first consider only the impact of synchro-betatron resonances generated by the crossing angles in a perfectly linear machine and without long-range interactions. Next we will address the question whether the increased nonlinearities in the presence of the crossing angles have an impact on the dynamic aperture using MAD. As in the earlier sections, this model will include all the long-range interactions and the IR quadrupole nonlinearities. We will consider 36 bunches in each beam so this scenario is only likely during a period of machine studies in Run IIa.

7 Crossing angles and 6D beam-beam interactions at B0 and D0 only

The strength of the synchro-betatron resonances excited by a crossing angle is often characterized by the so-called Piwinski parameter $\chi = \phi\sigma_s/\sigma_\perp$. Typically it is required that $\chi < 1$ to limit the strength of these resonances. A naive interpretation of this parameter would require that at fixed crossing angle, the ratio of the bunch length to transverse size should be made as small as possible to reduce the effects of these resonances. However we have seen in Section 2 that at longer bunch lengths, the beneficial aspects of phase averaging over a bunch are important. Hence the Piwinski parameter needs to be used with care when the effects of synchro-betatron resonances are estimated.

Observations at several electron-positron colliders where bunch lengths are short have shown that the maximum crossing angle is limited by these resonances [21, 22]. The impact of beam-beam driven synchro-betatron resonances in hadron colliders is not as well established. An experiment performed at the SPS [23] showed no observable effect on the lifetime or background losses for χ as large as XX. The reduced impact of these resonances may be due to the longer bunch lengths and smaller synchrotron tunes in hadron colliders.

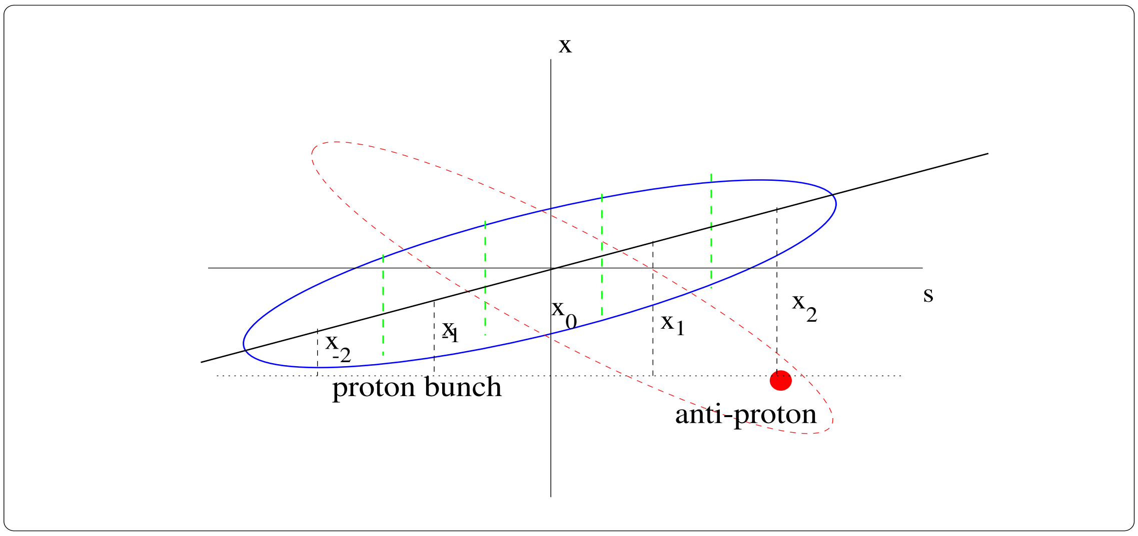

Figure 33: Crossing angle geometry at the IP. The strong proton bunch is divided into a number of slices.

In this section we will consider the importance of bunch length effects in the synchro-betatron resonances. The model of the beam-beam interactions at the main IPs is similar to the one described in Section 3 with one difference. The difference is in the transverse size of each slice which now depends on the crossing angle. Thus the hour-glass effect is modified as follows.

Hourglass Effects

The crossing angle at the IPs is accounted for by slicing the strong bunch into a number of disks and the distance of the particle to the center of each disk is used in computing the beam-beam force. The transverse size of each disk is different because of the change in β function (hour-glass effect) and this is taken into account. The beams will collide in a plane which makes an angle θ_{plane} with the longitudinal axis l centered in the detectors. On this collisional plane, the beams cross at an angle of 2ϕ. Hence a particle which is at a distance s from the center of the bunch (assumed to be at the IP) measured along the bunch axis, is at a projected longitudinal distance $l = s\cos\phi\cos\theta_{plane}$ from the IP. Since the beta function depends on the longitudinal distance l, the beta function and beam size of the i'th slice are given by

$$\beta_x(i) = \beta_x^* + \frac{l_i^2}{\beta_x^*} = \beta_x^* + \frac{(s_i \cos\phi \cos\theta_{plane})^2}{\beta_x^*} \tag{7.1}$$

$$\sigma_x(i) = \sqrt{[1 + (\frac{(s_i \cos\phi \cos\theta_{plane})}{\beta_x^*})^2]\sigma_x^*} \tag{7.2}$$

and similar expressions for the vertical beam size.

The expressions for the kicks from each slice are given by Equations (3.6) and (3.7). Now $x = x_\beta + s\phi_x$ where x_β is the betatron amplitude of the particle, s is the longitudinal distance of the particle from its bunch center and ϕ_x is half the crossing angle in the x plane. Similarly $x_i = s_i\phi_x$ where $-\sigma_s \leq s_i \leq \sigma_s$ with $s_i > 0$ to the right of the IP. In addition to the transverse kicks, we also include the energy kick due to the crossing angle,

$$\delta(\frac{\Delta E}{E}) = (F_x\phi_x + F_y\phi_y) \tag{7.3}$$

where $\delta(\Delta E/E)$ is the change in the relative energy, F_x, F_y are the transverse kicks due to the beam-beam force and ϕ_x, ϕ_y are the half-crossing angles in the transverse planes. We assume a 45° crossing plane so that $\phi_x = \phi_y = \phi/\sqrt{2}$. In principle we should also include the energy kick that is always present due to the slopes of the particle trajectory, $\delta(\Delta E/E) = (F_x x' + F_y y')$. We chose not to include this contribution so as to isolate the synchro-betatron resonances driven by the crossing angle.

Six dimensional Gaussian distributions of 1000 particles with amplitudes ranging from 0-4 σ in the transverse plane and 0-3σ in the longitudinal plane were tracked for a million turns for different crossing angles. This was done for three different initial distributions. The left plot in Figure 34 shows the maximum transverse amplitude reached by any particle in the distribution over the million turns as a function of the crossing angle for the two different models. With only the hour glass effects, particles in the distributions reach amplitudes of 6σ or more at 200-300μrad and to smaller values at increasing angles. This model would predict that the synchro-betatron resonances would be most harmful at crossing angles in the neighbourhood of 300μrad. When all the bunch length effects are included, we would arrive at somewhat different conclusions. The amplitude growth is significantly smaller at all crossing angles and does not appear to reach a maximum in this range of angles. The right plot in Figure 34 shows the maximum change in the averaged transverse amplitude of the distribution as a function of the crossing angle. With only the hourglass effects, there is a large change in the average amplitude as the crossing angle is increased from 100 to 200μrad and smaller changes at increasing crossing angles. With all bunch length effects, the averaged amplitude growth is much smaller and less than 0.2% over the entire range of crossing angles. Taken together these results show that when all bunch length effects are included, amplitude growth due to synchro-betatron resonances are significantly smaller. As mentioned earlier, with larger bunches the betatron phase advance over the length of the bunch increases and this mitigates the increase in synchro-betatron resonance strength predicted by the increase in the Piwinski parameter χ.

Using this code we also did a tune scan to check the sensitivity of the synchro-betatron resonances to the choice of tune. The nominal tunes in this study were (0.581, 0.575), slightly different from the values used in Section 4. The tunes in this scan are shown in the table accompanying the plot in Figure 35. At each tune the crossing angle was varied in the range from 0-500 μrad. The plot in Figure 35 shows the maximum change in the averaged amplitude of the distribution at each tune and crossing angle. At the nominal value, tune 4, the amplitude growth does not change significantly with crossing angles in the range from 100-500 μrad. However at tunes 1 and 2 the amplitude growth increases monotonically with crossing angle and reaches very large values. We observe that at these tunes, particles even at small amplitudes within the core ($< 3\sigma$) are excited to large amplitudes. At tunes 6 and 7 the amplitude growth increases as the crossing angle is increased to 300μrad and then decreases with increasing crossing angle. Overall these simulations show that (a) amplitude growth is much more sensitive to the tune when a crossing angle is introduced and (b) the optimum crossing angle where amplitude growth is the least depends on the choice of tune.

8 Dynamic Aperture with Crossing Angles and 36× 36 bunches

In this section we calculate the dynamic aperture with crossing angles using MAD. All long-range interactions and IR quadrupole nonlinearities are included. The beam-beam interactions at B0 and D0 with crossing angles

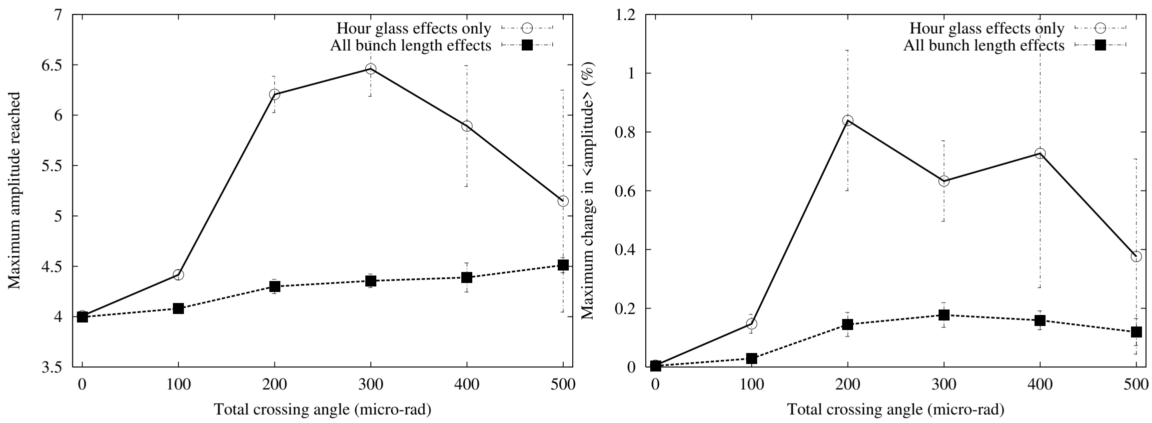

Figure 34: Simulations with crossing angles and only beam-beam interactions at B0 and D0 with two models for the interactions - one had only hour-glass effects, the other had all bunch length effects included. The initial distribution had 1000 particles between 0 and 4 σ. Three seeds were used for the initial distribution. Particles were tracked for 1 million turns. In each plot the average and the rms deviation over the seeds are shown as the data points with error bars. Left: Maximum amplitude reached among 1000 particles as a function of the total crossing angle. Right: Maximum % change in the averaged amplitude of the distribution as a function of the total crossing angle. It is clear that including all the bunch length effects reduces the amplitude growth significantly.

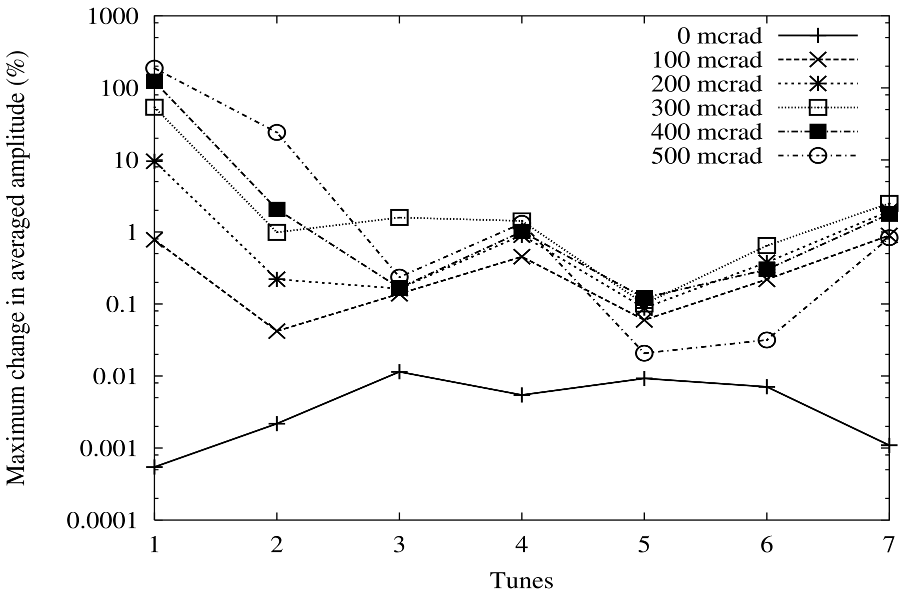

Tune #	ν_x	ν_y
1	0.575	0.569
2	0.577	0.571
3	0.579	0.573
4	0.581	0.575
5	0.583	0.577
6	0.585	0.579
7	0.587	0.581

Figure 35: Maximum change in the averaged amplitude as a function of the tune. The initial distribution had particles distributed between 0 and 5.25 σ. See the text for values of the tunes. The amplitude growth at tune 4 and its neighbourhood is low up to crossing angles of 500μrad. It is clear however that the crossing angle makes the dynamics more sensitive to the working point. At tune 1 (ν_x=0.575, ν_y=0.569) the amplitude growth increases to very large values as the crossing angle is increased. The table on the right shows the tunes used for the tune scan. Note that $\nu_x - \nu_y = 0.006$ for all tunes.

are modelled by slicing the strong beam and offsetting the slices - as shown in the previous section. This ensures that the transverse beam-beam kick is coupled to the longitudinal position of the particle. However the MAD model of the beam-beam lens is inherently 4 dimensional so energy kicks due to the beam-beam cannot be included in the tracking. Experience with other codes at other laboratories, e.g. Reference [28], shows that these energy kicks do not have a significant influence. Tracking with MAD in the rest of the lattice is however fully 6 dimensional. At a later stage we may repeat the tracking using a fully 6D beam-beam lens with a different code.

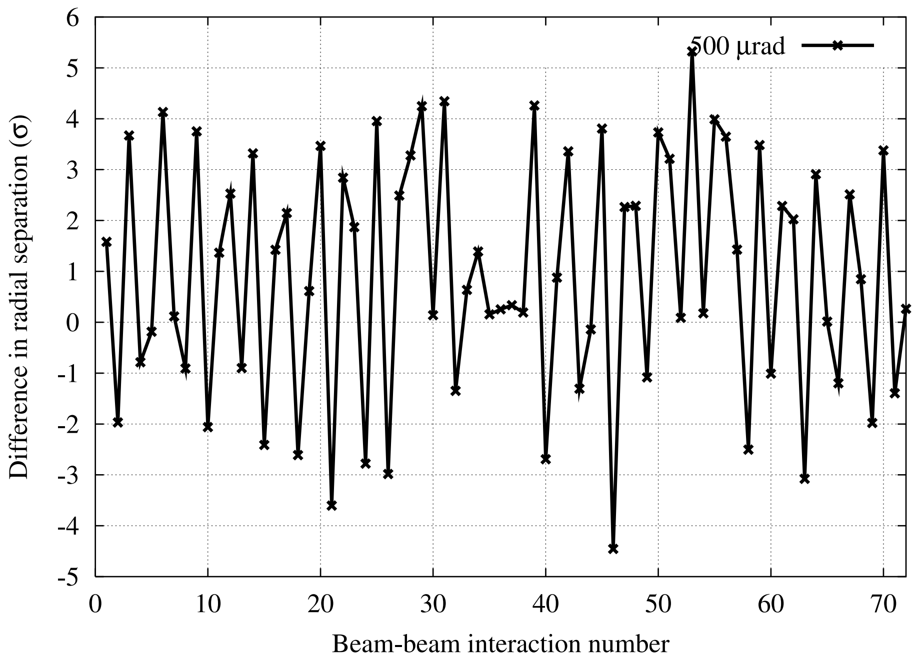

Figure 36: Difference in radial separation between the beams at the locations of the long-range interactions for bunch 6. The differences are taken between separations without a crossing angle and with a 500 μ radian crossing angle. A positive value implies that the separation with the crossing angle is greater. The separations at D0 (# 30) and B0 (# 54) are close to zero even with a crossing angle.

Crossing angles at B0 and D0 are generated using the separators in the ring. While almost all separators are changed to some extent, the primary separators used are B17H, B11H, D48H in the horizontal plane and B11V, C17V, A17V in the vertical plane. The maximum crossing angles that are possible are determined by the maximum separator strength which is about 4.5 MV/m. In this tracking we have studied three crossing angles: 300, 400 and 500 μrad. Increasing loss of luminosity as well as separator strengths preclude the possibility of much higher crossing angles. With a crossing angle, large changes in orbit are within the IR but the orbit in the arcs also changes. This changes the separations between the beams at the locations of the long-range interactions. Figure 36 shows the difference in radial separation at each beam-beam encounter when the crossing angle is increased to 500μradian. We ensure that the beam separations at B0 and D0 are maintained as close to zero as possible. At some locations the separations decrease by more than 4σ while at many others the separations increase by more than 4σ. While the change in separation fluctuates, on average the separation at this crossing angle increases by about 1 σ. It is clear that the locations of the closest parasitic encounters change with the crossing angle.

Figure 37 shows the 6D DA after 10^5 turns with total crossing angles from 300-500 μrad. For comparison, the DA without a crossing angle is also shown. While the stable boundary changes shape when crossing angles are introduced, there is no significant change in the average or minimum DA with increasing crossing angle, as seen in Table 12. Thus the synchro-betatron resonances generated by the interactions at B0 and D0 do not appear to have a significant impact - the dynamics is still dominated by the long-range interactions for the range of crossing angles studied. In future studies we will evaluate the influence of tunes and longer time scales on

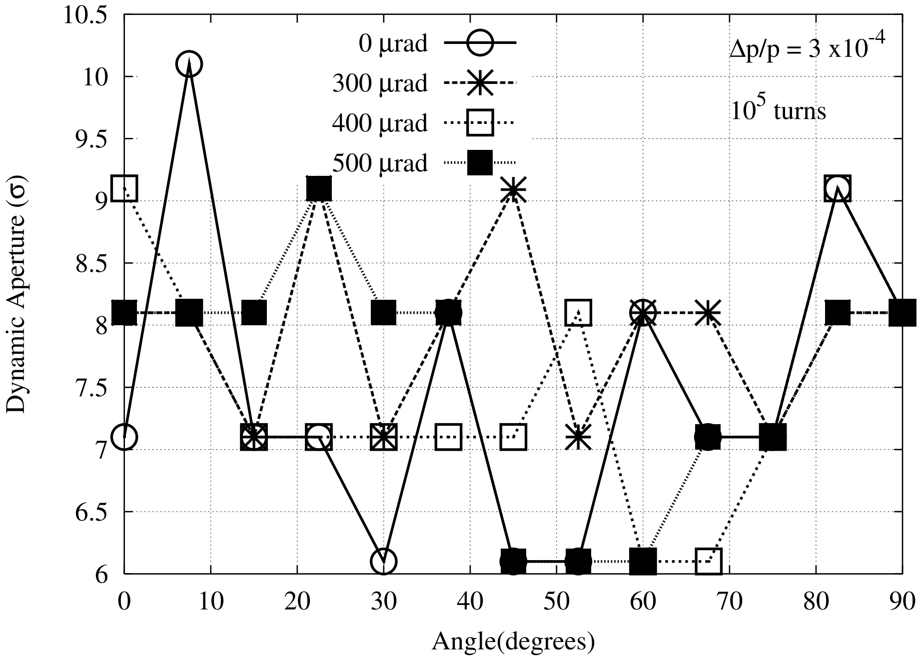

Figure 37: Dynamic aperture of bunch 6 at different total crossing angles. Particles were tracked in 6D for 100,000 turns with $\Delta p/p = 3 \times 10^{-4}$. Tunes were the nominal values: (0.585, 0.575).

the choice of crossing angle.

Crossing angle [μrad]	$(\langle DA \rangle, DA_{min})$
0	(7.5, 6.0)
300	(7.9, 7.0)
400	(7.5, 6.0)
500	(7.6, 6.0)

Table 12: Average and minimum 6D DA after 10^5 turns at three different crossing angles. These results show that in this configuration of 36× 36 bunches, crossing angles do not have a significant impact on the dynamics at these tunes (0.585, 0.575) and this time scale.

9 Conclusions

9.1 Bunch length effects

Analytical calculations and multi-particle tracking show that amplitude growth of particles is a decreasing oscillatory function of the bunch length. We also find that beam-beam resonance strengths with bunch lengths comparable to β^* are significantly weaker than those for infinitesimally short bunches.

9.2 Run IIa

We present our main conclusions in a question-answer format.

- *What is the dynamic aperture (DA) with all the beam-beam interactions ?*

  At design parameters and after 10^6 turns, the DA for bunch 6 is about 8σ (4D) and about 5σ (6D, $\Delta p/p = 3\times 10^{-4}$, $\nu_x' = \nu_y' = 5$). The 6D value is smaller than the aperture limitation set by the primary collimators. The dynamic aperture does not appear to reach an asymptotic value even after 10^6 turns but instead keeps decreasing with the number of turns followed. This contrasts with the dynamic aperture for single beams which does not change much after 10^5 turns.

- *Is the DA sensitive to the choice of tunes?*

  A tune scan around the nominal working point (the tune values can be seen in Figure 18) showed that the DA does not change significantly as long as the tunes are sufficiently far from the 5th and 7th order resonances. Reversing the tunes ($\nu_x = 0.575$, $\nu_y = 0.585$) results in a marginally larger value of the DA by 1σ.

- *How important are the head-on interactions compared to the long-range interactions?*

  The tune footprint is largely determined by the head-on interactions. However they have very little influence on the dynamic aperture. Thus the dynamic aperture with only the parasitic interactions is nearly the same as that with the parasitic and the head-on interactions. This is observed to be true at several other tunes in the vicinity of the working point. Hence it is not obvious that compressing the footprint would improve the dynamic aperture.

- *Is there a dominant group of long-range interactions ?*

  Yes, of the seventy long-range interactions the four interactions nearest to the two IPs are the dominant group. The 4D DA with only these long-range interactions is nearly the same as with all the interactions while the 6D DA is about 1σ larger. This also indicates that the synchro-betatron resonances driven by the other long-range interactions are important.

- *Is the DA sensitive to the separation at the nearest parasitics?*

  The average 4D DA increases by about 1.5σ when the separation at these locations is increased from 6σ to 10σ. The increase in the 6D DA is smaller, only about 0.5σ. This suggests that the effects of the synchro-betatron resonances driven by the long-range do not decay very rapidly with the beam separation. This in turn may be because the amplitude dependent chromaticity due to the long-range interactions is relatively insensitive to the beam separation at large amplitudes. Reducing the longitudinal emittance would be helpful in increasing the 6D DA of a bunch.

  This result in 6D is somewhat surprising. This begs the question then why the beam-beam interactions in Run I, where the separations were of the order of 10σ, did not usually pose a serious limitation? The answer may lie in the details; higher proton bunch intensities in this study, differences in Twiss functions at the parasitic interactions, particularly the dispersion, and phase advances between the interactions.

- *What are the mechanisms for amplitude growth ?*

  We have found with 4D tracking that there is no evidence of wide-spread diffusion close to the stable boundary. Instead, the motion near the boundary is characterized by thin chaotic layers. At this boundary the survival time depends very sensitively on the initial coordinates. Thus in a pair of particles separated by 0.5μm (0.014σ), one might survive for more than 10^5 turns while the other is lost within 10^4 turns.

A signature of eventual particle loss appears to be tune changes > 0.001 within 10^4 turns. These changes in tune start long before the particle is lost and are apparently due to the overlapping of twelfth and higher order resonances. Our simulations lend support to the picture of narrow streaming channels in phase space which, relatively slowly, transport particles out to larger amplitudes where other resonances cause fast loss.

- *Which resonances cause fast loss?*

  With a tune scan and 4D tracking we find that at amplitudes of 6σ and 7σ the seventh order sum resonances, particularly the $4\nu_x + 3\nu_y$ and $5\nu_x + 2\nu_y$ resonances, cause large amplitude growth within 10^3 turns.

  The synchro-betatron resonances at the nominal working point do not appear to be responsible for fast loss but the additional streaming channels created by the sideband resonances $m_x\nu_x + m_y\nu_y + m_s\nu_s = p$ of the twelfth order sum resonances, in particular (m_x, m_y) = (3, 9), (4, 8), (7, 5), (8, 4) and $|m_s| \leq 3$, destabilize particles that would be stable without synchrotron oscillations over longer time scales.

- *What is the bunch to bunch variation in DA?*

  We have studied bunch 6 (near the center of the bunch train) in some detail and bunch 1 at the head of the train to some extent. The differences in DA between these two bunches are not significant but bunch 1 may have a marginally smaller DA.

- *Do compensation schemes work?*

  We have not directly addressed this question in this report. However we do find that with beam-beam interactions there is no direct correlation between the size of a tune footprint and the dynamic aperture.

  This suggests that it may be more useful to use the proposed Tevatron electron lens [27] to compensate for an "averaged" long-range force from all the parasitic collisions rather than attempting to reduce the footprint in the second stage of this project. This speculation can be checked with a tracking model that includes the field of the electron lens. A more conventional idea would be to compensate the 7th order resonances which appear to be strongly driven.

- *What effects are not included in this study?*

  We list the important ones: error fields in the arc magnets, misalignments, time dependent effects such as power supply ripple which can modulate the tunes and beam separation, bunch to bunch differences in emittance and intensity.

- *How accurate are the models of the beam-beam interactions?*

  We believe that with the inclusion of bunch length effects, the transverse kicks due to the beam-beam interactions at B0 and D0 are modelled fairly accurately. The MAD model of the beam-beam interaction does not include the energy kicks so these are missing from our tracking. Simulations using other codes for different accelerators, see e.g. Reference [28], show that the energy kicks do not have a significant impact.

  The long-range kicks are modelled as point interactions and of course without energy kicks. The justification for ignoring bunch length effects in these interactions is that the beta functions at these locations are not very small so hour-glass effects and the phase advance over the length of the opposing strong bunch should be negligible. That said, it should be noted that point interactions over-emphasize the strength of the kick so the tracking model may over-estimate somewhat the effects due to the long-range interactions.

9.3 Crossing angles with 36$\times$ 36 bunches

We find that bunch length effects reduce the impact of synchro-betatron resonances when crossing angles are introduced. Once these bunch length effects are included in the interactions at B0 and D0, the synchro-betatron resonances generated by the crossing angles do not have a significant impact up to crossing angles of 500 μrads. The dynamics is dominated by the long-range interactions.

References

[1] Run II handbook, Fermilab report (unpublished)

[2] T. Sen, *The beam-beam interaction of finite length bunches in hadron colliders*, FNAL preprint FNAL-Pub-00/093-T (2000)

[3] T. Sen, *Beam-beam studies for the Tevatron*, FNAL-Conf-00/124-T, appeared in Proc. of a workshop on accelerator physics experiments for future hadron colliders, BNL-52601 (2000)

[4] T. Sen, N. Gelfand, M. Xiao, *Beam-beam interactions at the Tevatron in Run IIa*, PAC 2001

[5] T. Sen, N. Gelfand, M. Xiao, *Beam-beam interactions in Run II at the Tevatron*, contributed to the Beam-beam workshop at Fermilab, June 25-27, 2001 (http://www-ap.fnal.gov/˜meiqin/beambeam01/beambeam01.html)

[6] S. Peggs, *Part. Accel.*, **17**, 11 (1985); D. Neuffer, *Part. Accel.*, **20**, 97 (1986)

[7] S. Krishnagopal and R. Siemann, *Phys. Rev. D*, **41**, 2312 (1990)

[8] M. Furman, *The Hourglass reduction factor for asymmetric colliders*, SLAC-ABC-41-REV;ESG-NOTE-161 (1992)

[9] CERN LHC Yellow report, CERN/AC/95-05 (1995)

[10] Gradshteyn and Ryzhik, *Table of Integrals*

[11] A. Hofmann and S. Myers, *Evaluation of the absolute LEP luminosity from measurement of the coherent beam-beam tune split*, CERN-LEP-NOTE-604 (1988)

[12] A. Piwinski, IEEE Trans. Nuc. Science, **NS-32**, 2240 (1985)

[13] F. Schmidt, CERN report CERN SL/94-56(AP) [http://home.cern.ch/frs/sixtrack.html]

[14] W. Fischer, M. Giovannozi and F. Schmidt, *Dynamic aperture experiment at a synchrotron*, Phys. Rev. E, **55**, 3507 (1997)

[15] W. Fischer, *An experimental study on the long-term stability of particle motion in hadron storage rings*, DESY preprint DESY 95-235 (1995)

[16] B. Erdelyi and T. Sen,*Analytic studies of long-range beam-beam tune shifts and chromaticities*, Fermilab report, to be publshed

[17] T. Sen, N. Gelfand, W. Wan, *Effect of the beam-beam interactions on the dynamic aperture and amplitude growth in the LHC*, in Proc. of a workshop on beam-beam effects in large hadron colliders, CERN-SL-99-039 AP (1999)

[18] Y. Alexahin, T. Sen, M. Xiao, *Beam-Beam excited synchro-betatron resonances in the Tevatron Run II lattice*, contributed to the Beam-beam workshop at Fermilab, June 25-27, 2001

[19] J. Irwin, *Diffusive losses from SSC particle bunches due to long-range beam-beam interactions*, SSC Preprint SSC-233 (1989)

[20] Y. Papaphillipou and F. Zimmerman, CERN preprint CERN-SL-99-039 AP (1999)

[21] D.L. Rubin et al.,*Beam-beam interaction with a horizontal crossing angle*, Nucl. Instr.& Meth. A, **330**, p 12 (1993)

[22] A. Piwinski, *Limitation of the luminosity by satellite resonances*, DESY preprint DESY 77/18 (1977)

[23] K. Cornelis, W. Herr, M. Meddahi; *Proton anti-proton collisions at a finite crossing angle in the SPS*, CERN-SL-91-20-DI-23 (1991)

[24] M. Abramowitz and I.A. Stegun, *Handbook of Mathematical Functions*, Dover Publications (1965)

[25] G.N. Watson, *A Treatise on the Theory of Bessel Functions*, Cambridge University Press (1966)

[26] E.T. Copson, *Asymptotic Expansions*, Cambridge University Press (1965)

[27] V. Shiltsev et al., *Tevatron electron lens for beam-beam compensation: first experimental results*, PAC 2001

[28] D. Sagan, R. Siemann, S. Krishnagopal, *Resonances in the beam-beam interaction due to a finite crossing angle*, EPAC1990, pg 1649

A Appendix: Proof of a Bessel function identity

In Section 2 we made use of a Bessel function identity that we have not found in the standard texts such as Abramowitz and Stegun [24] and the treatise on Bessel functions by Watson [25]. Here for the sake of completeness we will prove this identity:

$$\sum_{j=-\infty}^{\infty} (-1)^j I_j^2(z) = 1 \tag{A.1}$$

for any arbitrary argument z.

First we note that the identity is true when $z = 0$ because

$$\begin{aligned} I_j(0) &= 1 \quad j = 0 \\ &= 0 \quad j \neq 0 \end{aligned} \tag{A.2}$$

The infinite sum can be written as

$$X = I_0^2(z) - 2I_1^2(z) + 2I_2^2(z) - \dots$$

We will show that this expression is independent of z, making use of the relation for the derivatives of the Bessel functions

$$2I_j'(z) = I_{j-1}(z) + I_{j+1}(z), \qquad I_0' = I_1 \tag{A.3}$$

Consider the derivative of the infinite sum.

$$\frac{dX}{dz} = 2I_0 I_0' - 2I_1 2I_1' + 2I_2 2I_2' - \dots \tag{A.4}$$

$$= 2I_0 I_1 - 2I_1(I_0 + I_2) + 2I_2(I_1 + I_3) - 2I_3(I_2 + I_4) + \dots \tag{A.5}$$

Note that all the terms cancel pairwise and hence the derivative vanishes. Since the expression X is independent of z, and $X = 1$ for $z = 0$, it follows that

$$\sum_{j=-\infty}^{\infty} (-1)^j I_j^2(z) = 1 \qquad \forall z \tag{A.6}$$

B Appendix: Field Errors in the IR quadrupoles

All errors are in units of 10^{-4}.

Field Errors in IR quadrupoles at D0

	Upstream (protons)			Downstream (protons)		
	Q2	Q3	Q4	Q4	Q3	Q2
(b_2, a_2)	-0.63, 4.11	-3.9, 4.62	0.54, 1.29	0.37, -3.6	-0.11, 3.03	-1.35, 3.06
(b_3, a_3)	-0.20, -0.40	1.21, -2.2	-0.33, -0.27	-0.25, -0.21	-0.13, 0.14	1.34, -0.15
(b_4, a_4)	0.13, -0.92	-0.020, 1.29	-0.060, 0.02	-0.20, -0.72	0.28, 0.43	-0.53, 0.33
(b_5, a_5)	-0.47, -0.78	-0.59, 0.02	-3.78, 0.75	-2.9, 0.40	-1.98, -0.3	-2.87, 0.37
(b_6, a_6)	-0.17, 0.57	-0.3, 0.47	0.12, 0.04	0.06, 0.33	0.14, 0.31	-0.21, 0.12
(b_7, a_7)	-0.42, 0.56	0.24, -0.26	0.17, 0.030	0.16, 0.15	-0.22, 0.15	-0.11, -0.11
(b_8, a_8)	0.21, 0.26	-0.17, 0.23	0.030, -0.12	0.16, -0.48	0.02, 0.05	0.05, 0.22
(b_9, a_9)	-0.71, -0.15	-0.81, 0.51	-0.86, 0.0	-1.4, 0.22	-0.65, 0.20	-0.73, 0.28

Field Errors in IR quadrupoles at B0

	Upstream (protons)			Downstream (protons)		
	Q2	Q3	Q4	Q4	Q3	Q2
(b_2, a_2)	-0.21, -2.330	1.68, -3.36	-0.49, -1.3	4.29, 0.57	-1.31, -0.94	1.79, -3.08
(b_3, a_3)	0.07, -1.95	0.63, -0.09	-0.12, 0.09	-2.33, -0.82	-0.19, -0.33	-0.12, -0.56
(b_4, a_4)	0.08, -0.51	0.44, -0.57	0.32, -0.05	-0.62, -0.79	0.61, -0.17	-0.62, -0.85
(b_5, a_5)	-2.59, 0.28	-2.96, 0.19	-3.21, 0.16	-0.32, -0.31	-2.77, 0.16	-2.71, 0.29
(b_6, a_6)	-0.09, 0.16	0.0, -0.33	-0.08, -0.08	1.06, 0.04	0.0, -0.34	-0.02, -0.28
(b_7, a_7)	0.03, -0.18	0.04, -0.01	0.02, -0.01	-0.24, -0.03	-0.09, -0.07	-0.08, -0.15
(b_8, a_8)	0.05, -0.05	0.18, -0.09	-0.36, -0.2	-0.36, 0.01	0.05, 0.05	-0.07, 0.09
(b_9, a_9)	-0.8, 0.15	-0.54, 0.08	-1.09, 0.48	-0.93, 0.42	-0.80, 0.0	-0.73, 0.21

C Appendix: Optics Changes with tune scans

Tune scans around the nominal working point (0.585, 0.575)

	Bare tunes	Tunes with beam-beam	(β_x^*, β_y^*) at B0	(β_x^*, β_y^*) at D0	$(\beta_x^{max}, \beta_y^{max})$
0	0.585, 0.575	0.611, 0.600	(0.331, 0.330)	(0.339, 0.330)	1155, 1156
1	0.575, 0.569	0.601, 0.595	(0.328, 0.327)	(0.335, 0.328)	
2	0.577, 0.571	0.603, 0.597	(0.329, 0.328)	(0.336, 0.329)	
3	0.579, 0.573	0.605, 0.599	(0.330, 0.329)	(0.337, 0.329)	
4	0.583, 0.577	0.610, 0.602	(0.331, 0.330)	(0.339, 0.330)	
5	0.585, 0.579	0.612, 0.604	(0.331, 0.331)	(0.340, 0.331)	
6	0.587, 0.581	0.614, 0.606	(0.332, 0.331)	(0.341, 0.331)	
7	0.575, 0.585	0.601, 0.610	(0.329, 0.331)	(0.337, 0.331)	(1160, 1153)
8	0.577, 0.587	0.603, 0.612	(0.330, 0.332)	(0.338, 0.331)	(1158, 1151)
9	0.579, 0.589	0.605, 0.614	(0.331, 0.333)	(0.338, 0.332)	(1157, 1150)
10	0.581, 0.591	0.608, 0.616	(0.331, 0.333)	(0.339, 0.332)	(1155, 1148)
11	0.583, 0.593	0.610, 0.618	(0.332, 0.334)	(0.340, 0.333)	(1153, 1147)
12	0.585, 0.595	0.611, 0.620	(0.332, 0.335)	(0.341, 0.333)	(1152, 1146)
13	0.551, 0.561	0.575, 0.585	(0.320, 0.322)	(0.323,0.324)	(1190, 1182)
14	0.553, 0.562	0.577, 0.587	(0.321, 0.323)	(0.324, 0.324)	(1187, 1180)
15	0.555, 0.564	0.580, 0.589	(0.322, 0.324)	(0.326, 0.325)	(1184, 1177)
16	0.556, 0.566	0.581, 0.591	(0.322, 0.324)	(0.326, 0.325)	(1182, 1174)
17	0.558, 0.568	0.583, 0.593	(0.323, 0.325)	(0.328, 0.326)	(1179, 1172)
18	0.560, 0.570	0.585, 0.595	(0.324, 0.326)	(0.329, 0.327)	(1176, 1168)

The lattice functions (β^*, β^{max}) shown are with all the beam-beam interactions included.